

We are committed to providing [accessible customer service](#).

If you need accessible formats or communications supports, please [contact us](#).

Nous tenons à améliorer [l'accessibilité des services à la clientèle](#).

Si vous avez besoin de formats accessibles ou d'aide à la communication, veuillez [nous contacter](#).

Reprocessing & Analysis of VTEM EM & Magnetic Surveys, Nipissing Cobalt, Ontario

**Larder Lake Mining Divisions,
Barr, Coleman, Firstbrook, Klock and Kittson Townships,
Ontario**

UTM NAD 83 (Zone 17) 582200 mE, 5254000 mN

NTS 031M05 & 041P08

FOR



Suite 902 – 18 King Street East

Toronto, Ontario

M5C 1C4

Zachary Matheson, BSc

March 25, 2019

TABLE OF CONTENTS

INTRODUCTION	1
PROPERTY LOCATION & ACCESS	1
CLAIMS & OWNERSHIP	3
REGIONAL AND PROPERTY GEOLOGY	19
HISTORIC EXPLORATION ACTIVITIES	21
CURRENT PROGRAM	24
REFERENCES	25
STATEMENT OF QUALIFICATIONS.....	26
APPENDIX A	27

LIST OF FIGURES

Figure 1: Regional Location Map, Nipissing Cobalt Property	2
Figure 2: Nipissing Cobalt Claim Map	18

LIST OF TABLES

Table 1: Nipissing Cobalt Claim List.....	4
---	---

LIST OF APPENDICES

Appendix A: "Report on Processing and Analysis of Five VTEM EM and Magnetic Surveys, Nipissing Cobalt and South Abitibi Properties, Ontario"

INTRODUCTION

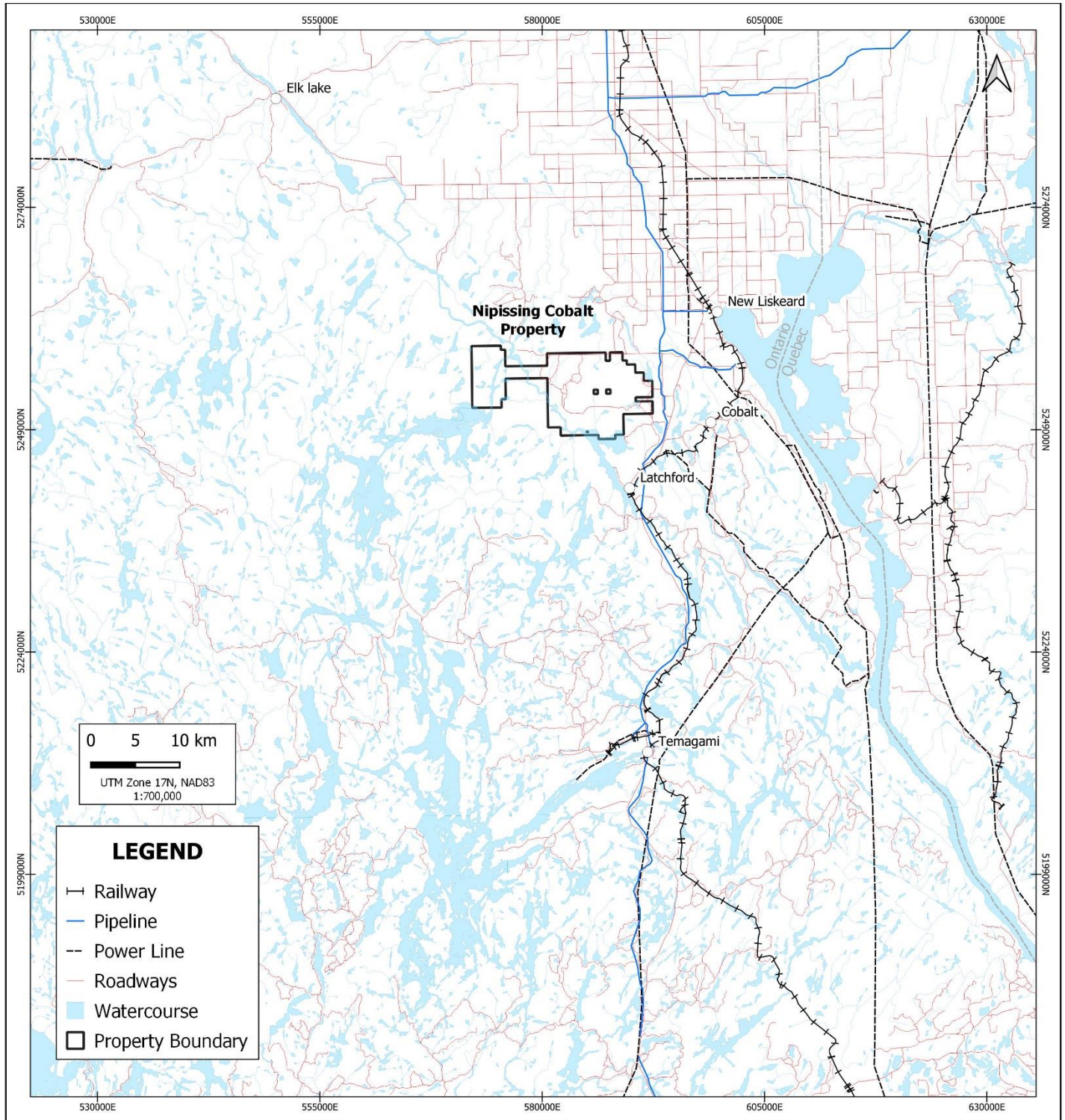
NewOrigin Gold Corp., formerly Tri Origin Exploration Ltd., have explored the Nipissing Cobalt property for gold and base metals, completing property wide geophysics, field mapping & sampling, and diamond drilling. During recent years, a resurgence of diamondiferous kimberlite exploration has taken place, and work completed by NewOrigin has indicated the potential for diamondiferous kimberlites in the area.

This report details the results and conclusions from the reprocessing & analysis of VTEM electromagnetic (EM) and magnetic airborne geophysical data completed by Condor Consulting Inc during the spring of 2021. This report is being submitted to the Ministry of Energy, Northern Development and Mines (MENDM) for assessment credits. The primary goal of the work completed was to reprocess magnetic and electromagnetic data to better delineate diamondiferous kimberlites across two of NewOrigin properties, the Nipissing Cobalt & South Abitibi properties, which the report completed by Condor Consulting pertains to.

PROPERTY LOCATION & ACCESS

The Nipissing Cobalt property is located approximately five kilometers north of Latchford, Ontario, and 10 km west of Cobalt, Ontario, centered at UTM coordinates 582200E/5254000N (UTM Zone 17, NAD83) on NTS map sheets 031M05 & 041P08. Year-round property access is available along the eastern-most portion of the claim block via Forest Access Rd which lies west of Trans-Canada Highway 11. The western portion of the property is accessible via Henwood 3 Rd, crossing the Montreal River from the north.

Figure 1: Regional Location Map, Nipissing Cobalt Property



CLAIMS & OWNERSHIP

The Nipissing Cobalt property has an area of approximately 12,387 hectares consisting of 570 Single Cell Mining Claims (Figure 2). All mineral claims lie within Barr, Coleman, Firstbrook, Klock and Kittson Townships of the Larder Mining Division. All claims are currently in good standing with NewOrigin Gold Corp. as the recorded owner (Table 1). Reprocessing of geophysical data for the purpose of this report was conducted on 566 cells within the Nipissing Cobalt claim block, as seen in Table 1.

Table 1: Nipissing Cobalt Claim List

Project	Township / Area	Tenure ID	Tenure Type	Tenure Status	Area (ha)	Anniversary Date	Included in Reporting
Nipissing Cobalt	FIRSTBROOK	100295	SCMC	Active	21.84433435	44797	Yes
Nipissing Cobalt	FIRSTBROOK	101597	SCMC	Active	21.83237773	44797	Yes
Nipissing Cobalt	KLOCK	102346	SCMC	Active	21.82725617	44797	Yes
Nipissing Cobalt	KLOCK	102347	SCMC	Active	21.83067765	44797	Yes
Nipissing Cobalt	BARR,COLEMAN,KITTSO	102997	SCMC	Active	21.85286897	44847	Yes
Nipissing Cobalt	FIRSTBROOK	103050	SCMC	Active	21.83579325	44797	Yes
Nipissing Cobalt	FIRSTBROOK	103051	SCMC	Active	21.8375087	44797	Yes
Nipissing Cobalt	FIRSTBROOK	103052	SCMC	Active	21.83750171	44797	Yes
Nipissing Cobalt	FIRSTBROOK	103519	SCMC	Active	21.83067415	44797	Yes
Nipissing Cobalt	KLOCK	103757	SCMC	Active	21.84091827	44797	Yes
Nipissing Cobalt	BARR	104538	SCMC	Active	21.8289722	44797	Yes
Nipissing Cobalt	BARR,COLEMAN	105694	SCMC	Active	21.85286897	44797	Yes
Nipissing Cobalt	BARR	105756	SCMC	Active	21.84263336	44797	Yes
Nipissing Cobalt	COLEMAN	105876	SCMC	Active	21.85971131	44797	Yes
Nipissing Cobalt	COLEMAN	105903	SCMC	Active	21.86140935	44797	Yes
Nipissing Cobalt	COLEMAN	106066	SCMC	Active	21.85627639	44797	Yes
Nipissing Cobalt	KLOCK	106120	SCMC	Active	21.83580024	44797	Yes
Nipissing Cobalt	BARR	109446	SCMC	Active	21.83237773	44797	Yes
Nipissing Cobalt	FIRSTBROOK	109986	SCMC	Active	21.83922053	44797	Yes
Nipissing Cobalt	BARR,KLOCK	111077	SCMC	Active	21.84434483	44797	Yes
Nipissing Cobalt	FIRSTBROOK	111116	SCMC	Active	21.84945233	44797	Yes
Nipissing Cobalt	BARR	111342	SCMC	Active	21.84604571	44797	Yes
Nipissing Cobalt	BARR	111389	SCMC	Active	21.8375087	44847	Yes
Nipissing Cobalt	KLOCK	112143	SCMC	Active	21.8460492	44797	Yes
Nipissing Cobalt	BARR	112628	SCMC	Active	21.83067066	44797	Yes
Nipissing Cobalt	KITTSO	112670	SCMC	Active	21.85627988	44847	Yes
Nipissing Cobalt	KITTSO	112671	SCMC	Active	21.8579974	44847	Yes
Nipissing Cobalt	BARR,FIRSTBROOK	116917	SCMC	Active	21.82896522	44797	Yes
Nipissing Cobalt	BARR	116918	SCMC	Active	21.83067415	44797	Yes
Nipissing Cobalt	FIRSTBROOK	117366	SCMC	Active	21.82896871	44797	Yes
Nipissing Cobalt	FIRSTBROOK	118192	SCMC	Active	21.84434483	44797	Yes
Nipissing Cobalt	BARR	118293	SCMC	Active	21.83579675	44797	Yes
Nipissing Cobalt	BARR	118294	SCMC	Active	21.84092176	44797	Yes
Nipissing Cobalt	COLEMAN,FIRSTBROOK	118360	SCMC	Active	21.85286897	44797	Yes
Nipissing Cobalt	FIRSTBROOK	118365	SCMC	Active	21.8375087	44797	Yes
Nipissing Cobalt	FIRSTBROOK	118366	SCMC	Active	21.83921704	44797	Yes
Nipissing Cobalt	BARR	118487	SCMC	Active	21.83067066	44797	Yes
Nipissing Cobalt	COLEMAN	118547	SCMC	Active	21.85459722	44797	Yes

Nipissing Cobalt	COLEMAN	118548	SCMC	Active	21.85459722	44797	Yes
Nipissing Cobalt	COLEMAN	118549	SCMC	Active	21.8579974	44797	Yes
Nipissing Cobalt	FIRSTBROOK	118604	SCMC	Active	21.83922053	44797	Yes
Nipissing Cobalt	FIRSTBROOK	118781	SCMC	Active	21.83409516	44797	Yes
Nipissing Cobalt	FIRSTBROOK	118840	SCMC	Active	21.83580024	44797	Yes
Nipissing Cobalt	FIRSTBROOK	119197	SCMC	Active	21.84945932	44797	Yes
Nipissing Cobalt	COLEMAN	120079	SCMC	Active	21.85628338	44797	Yes
Nipissing Cobalt	FIRSTBROOK	120505	SCMC	Active	21.84604571	44797	Yes
Nipissing Cobalt	FIRSTBROOK	120557	SCMC	Active	21.84945932	44797	Yes
Nipissing Cobalt	FIRSTBROOK	120558	SCMC	Active	21.84945583	44797	Yes
Nipissing Cobalt	FIRSTBROOK	121752	SCMC	Active	21.83067415	44797	Yes
Nipissing Cobalt	FIRSTBROOK	121753	SCMC	Active	21.83238122	44797	Yes
Nipissing Cobalt	FIRSTBROOK	121754	SCMC	Active	21.83409166	44797	Yes
Nipissing Cobalt	BARR	121993	SCMC	Active	21.84262986	44797	Yes
Nipissing Cobalt	BARR	121994	SCMC	Active	21.84604571	44797	Yes
Nipissing Cobalt	COLEMAN,FIRSTBROOK	122079	SCMC	Active	21.4334062	44797	Yes
Nipissing Cobalt	KLOCK	122677	SCMC	Active	21.83408817	44797	Yes
Nipissing Cobalt	KLOCK	122678	SCMC	Active	21.83580373	44797	Yes
Nipissing Cobalt	KITSON	123417	SCMC	Active	21.86140585	44847	Yes
Nipissing Cobalt	FIRSTBROOK	125729	SCMC	Active	21.84263336	44797	Yes
Nipissing Cobalt	FIRSTBROOK	125730	SCMC	Active	21.84434134	44797	Yes
Nipissing Cobalt	BARR	125858	SCMC	Active	21.8375087	44797	Yes
Nipissing Cobalt	FIRSTBROOK	127118	SCMC	Active	21.83067415	44797	Yes
Nipissing Cobalt	FIRSTBROOK	127612	SCMC	Active	21.84263336	44797	Yes
Nipissing Cobalt	FIRSTBROOK	127652	SCMC	Active	21.85117557	44797	Yes
Nipissing Cobalt	KLOCK	128377	SCMC	Active	21.82554699	44797	Yes
Nipissing Cobalt	KLOCK	128378	SCMC	Active	21.83067415	44797	Yes
Nipissing Cobalt	COLEMAN,FIRSTBROOK	129765	SCMC	Active	21.85287247	44797	Yes
Nipissing Cobalt	FIRSTBROOK	129833	SCMC	Active	21.83580024	44797	Yes
Nipissing Cobalt	COLEMAN	129982	SCMC	Active	21.8580009	44797	Yes
Nipissing Cobalt	BARR	130458	SCMC	Active	21.83921354	44797	Yes
Nipissing Cobalt	COLEMAN,KITSON	131162	SCMC	Active	21.8580009	44847	Yes
Nipissing Cobalt	FIRSTBROOK	132463	SCMC	Active	21.84945932	44797	Yes
Nipissing Cobalt	BARR,KLOCK	133220	SCMC	Active	21.84776044	44797	Yes
Nipissing Cobalt	BARR	133221	SCMC	Active	21.84945583	44797	Yes
Nipissing Cobalt	BARR	133222	SCMC	Active	21.84945583	44797	Yes
Nipissing Cobalt	BARR,KLOCK	133223	SCMC	Active	21.84946282	44797	Yes
Nipissing Cobalt	BARR	133788	SCMC	Active	21.83409516	44847	Yes
Nipissing Cobalt	BARR	133844	SCMC	Active	21.82896173	44797	Yes
Nipissing Cobalt	KITSON	133883	SCMC	Active	21.8579974	44847	Yes
Nipissing Cobalt	FIRSTBROOK	137029	SCMC	Active	21.84433784	44797	Yes
Nipissing Cobalt	BARR	137691	SCMC	Active	21.84775345	44797	Yes

Nipissing Cobalt	COLEMAN,FIRSTBROOK	137867	SCMC	Active	21.85286897	44797	Yes
Nipissing Cobalt	BARR	138352	SCMC	Active	21.83580024	44847	Yes
Nipissing Cobalt	COLEMAN,KITTSO	138455	SCMC	Active	21.85970781	44847	Yes
Nipissing Cobalt	BARR	138625	SCMC	Active	21.84091477	44797	Yes
Nipissing Cobalt	KITTSO	139818	SCMC	Active	21.86140935	44847	Yes
Nipissing Cobalt	BARR,KLOCK	140245	SCMC	Active	21.83751219	44797	Yes
Nipissing Cobalt	COLEMAN	141259	SCMC	Active	20.30599494	44797	Yes
Nipissing Cobalt	FIRSTBROOK	143069	SCMC	Active	21.84263336	44797	Yes
Nipissing Cobalt	FIRSTBROOK	143070	SCMC	Active	21.84263685	44797	Yes
Nipissing Cobalt	FIRSTBROOK	143071	SCMC	Active	21.84434134	44797	Yes
Nipissing Cobalt	FIRSTBROOK	143072	SCMC	Active	21.8460492	44797	Yes
Nipissing Cobalt	FIRSTBROOK	143328	SCMC	Active	21.84945932	44797	Yes
Nipissing Cobalt	FIRSTBROOK	143343	SCMC	Active	21.84775694	44797	Yes
Nipissing Cobalt	COLEMAN,FIRSTBROOK	143344	SCMC	Active	21.85286897	44797	Yes
Nipissing Cobalt	BARR	144348	SCMC	Active	21.83409516	44847	Yes
Nipissing Cobalt	BARR	144349	SCMC	Active	21.8375087	44847	Yes
Nipissing Cobalt	FIRSTBROOK	144796	SCMC	Active	21.84091827	44797	Yes
Nipissing Cobalt	FIRSTBROOK	144797	SCMC	Active	21.84434134	44797	Yes
Nipissing Cobalt	KLOCK	145745	SCMC	Active	21.84946282	44797	Yes
Nipissing Cobalt	BARR,KLOCK	146513	SCMC	Active	21.84263685	44797	Yes
Nipissing Cobalt	COLEMAN	148054	SCMC	Active	21.85971131	44797	Yes
Nipissing Cobalt	FIRSTBROOK	149067	SCMC	Active	21.85117207	44797	Yes
Nipissing Cobalt	BARR	150419	SCMC	Active	21.83067066	44797	Yes
Nipissing Cobalt	KITTSO	150458	SCMC	Active	21.85459372	44847	Yes
Nipissing Cobalt	BARR	153355	SCMC	Active	21.83580373	44847	Yes
Nipissing Cobalt	FIRSTBROOK	153707	SCMC	Active	21.84263336	44797	Yes
Nipissing Cobalt	KITTSO	153968	SCMC	Active	21.85460421	44847	Yes
Nipissing Cobalt	KITTSO	153969	SCMC	Active	21.85629038	44847	Yes
Nipissing Cobalt	BARR	154322	SCMC	Active	21.83408817	44847	Yes
Nipissing Cobalt	BARR	154323	SCMC	Active	21.83922403	44797	Yes
Nipissing Cobalt	FIRSTBROOK	154383	SCMC	Active	21.83409166	44797	Yes
Nipissing Cobalt	FIRSTBROOK	155046	SCMC	Active	21.83238122	44797	Yes
Nipissing Cobalt	BARR	155204	SCMC	Active	21.83921704	44797	Yes
Nipissing Cobalt	COLEMAN	155345	SCMC	Active	21.85628338	44797	Yes
Nipissing Cobalt	COLEMAN	155346	SCMC	Active	21.8580009	44797	Yes
Nipissing Cobalt	KLOCK	156327	SCMC	Active	21.83067066	44797	Yes
Nipissing Cobalt	KLOCK	156354	SCMC	Active	21.83237773	44797	Yes
Nipissing Cobalt	FIRSTBROOK	157197	SCMC	Active	21.84263336	44797	Yes
Nipissing Cobalt	COLEMAN	157709	SCMC	Active	21.85628338	44797	Yes
Nipissing Cobalt	BARR	158470	SCMC	Active	21.83409166	44847	Yes
Nipissing Cobalt	BARR	158471	SCMC	Active	21.8375087	44847	Yes
Nipissing Cobalt	FIRSTBROOK	158543	SCMC	Active	21.83580373	44797	Yes

Nipissing Cobalt	KLOCK	159862	SCMC	Active	21.84776044	44797	Yes
Nipissing Cobalt	BARR,KLOCK	160617	SCMC	Active	21.83922053	44797	Yes
Nipissing Cobalt	BARR	160618	SCMC	Active	21.84433784	44797	Yes
Nipissing Cobalt	BARR	160866	SCMC	Active	21.83409166	44797	Yes
Nipissing Cobalt	FIRSTBROOK	160884	SCMC	Active	21.83408817	44797	Yes
Nipissing Cobalt	KLOCK	161780	SCMC	Active	21.84263336	44797	Yes
Nipissing Cobalt	COLEMAN,KITTSO	161838	SCMC	Active	21.85628338	44847	Yes
Nipissing Cobalt	KLOCK	162410	SCMC	Active	21.82896871	44797	Yes
Nipissing Cobalt	BARR,KITTSO	162428	SCMC	Active	21.85287596	44847	Yes
Nipissing Cobalt	FIRSTBROOK	162909	SCMC	Active	21.84090778	44797	Yes
Nipissing Cobalt	FIRSTBROOK	165088	SCMC	Active	21.84262986	44797	Yes
Nipissing Cobalt	COLEMAN,FIRSTBROOK	165282	SCMC	Active	21.85287247	44797	Yes
Nipissing Cobalt	BARR	166862	SCMC	Active	21.82896522	44797	Yes
Nipissing Cobalt	FIRSTBROOK	166883	SCMC	Active	21.83409166	44797	Yes
Nipissing Cobalt	FIRSTBROOK	167092	SCMC	Active	21.83067765	44797	Yes
Nipissing Cobalt	FIRSTBROOK	167237	SCMC	Active	21.85117207	44797	Yes
Nipissing Cobalt	KLOCK	167815	SCMC	Active	21.8375087	44797	Yes
Nipissing Cobalt	KLOCK	167816	SCMC	Active	21.84263336	44797	Yes
Nipissing Cobalt	BARR	168014	SCMC	Active	21.83409166	44847	Yes
Nipissing Cobalt	BARR	168581	SCMC	Active	21.82725617	44797	Yes
Nipissing Cobalt	BARR	168582	SCMC	Active	21.8255435	44797	Yes
Nipissing Cobalt	KITTSO	168628	SCMC	Active	21.85627988	44847	Yes
Nipissing Cobalt	FIRSTBROOK	171014	SCMC	Active	21.8375087	44797	Yes
Nipissing Cobalt	FIRSTBROOK	171015	SCMC	Active	21.83921704	44797	Yes
Nipissing Cobalt	FIRSTBROOK	171677	SCMC	Active	21.82896522	44797	Yes
Nipissing Cobalt	FIRSTBROOK	172047	SCMC	Active	21.84775694	44797	Yes
Nipissing Cobalt	BARR	172913	SCMC	Active	21.83580024	44847	Yes
Nipissing Cobalt	FIRSTBROOK	173011	SCMC	Active	21.83579675	44797	Yes
Nipissing Cobalt	FIRSTBROOK	173012	SCMC	Active	21.83921704	44797	Yes
Nipissing Cobalt	FIRSTBROOK	173213	SCMC	Active	21.84945583	44797	Yes
Nipissing Cobalt	FIRSTBROOK	173223	SCMC	Active	21.83751219	44797	Yes
Nipissing Cobalt	FIRSTBROOK	173224	SCMC	Active	21.83921704	44797	Yes
Nipissing Cobalt	BARR	173343	SCMC	Active	21.8375087	44797	Yes
Nipissing Cobalt	FIRSTBROOK	174424	SCMC	Active	21.83067415	44797	Yes
Nipissing Cobalt	BARR	174796	SCMC	Active	21.83409166	44847	Yes
Nipissing Cobalt	BARR	174797	SCMC	Active	21.83579675	44797	Yes
Nipissing Cobalt	BARR	174798	SCMC	Active	21.8375052	44797	Yes
Nipissing Cobalt	KLOCK	175768	SCMC	Active	21.82896522	44797	Yes
Nipissing Cobalt	COLEMAN	176630	SCMC	Active	21.8580044	44797	Yes
Nipissing Cobalt	COLEMAN	176631	SCMC	Active	21.85970781	44797	Yes
Nipissing Cobalt	BARR	177130	SCMC	Active	21.83238471	44797	Yes
Nipissing Cobalt	COLEMAN,FIRSTBROOK	177197	SCMC	Active	21.85286547	44797	Yes

Nipissing Cobalt	FIRSTBROOK	177259	SCMC	Active	21.8375087	44797	Yes
Nipissing Cobalt	FIRSTBROOK	177260	SCMC	Active	21.83921354	44797	Yes
Nipissing Cobalt	COLEMAN	177291	SCMC	Active	21.85460071	44797	Yes
Nipissing Cobalt	BARR	178723	SCMC	Active	21.84434833	44797	Yes
Nipissing Cobalt	COLEMAN	179351	SCMC	Active	21.85628688	44797	Yes
Nipissing Cobalt	FIRSTBROOK	179723	SCMC	Active	21.83067066	44797	Yes
Nipissing Cobalt	FIRSTBROOK	179724	SCMC	Active	21.83237424	44797	Yes
Nipissing Cobalt	FIRSTBROOK	180499	SCMC	Active	21.82896522	44797	Yes
Nipissing Cobalt	FIRSTBROOK	180568	SCMC	Active	21.8375087	44797	Yes
Nipissing Cobalt	KLOCK	181271	SCMC	Active	21.83921704	44797	Yes
Nipissing Cobalt	KLOCK	181272	SCMC	Active	21.83921354	44797	Yes
Nipissing Cobalt	FIRSTBROOK	182222	SCMC	Active	21.84434483	44797	Yes
Nipissing Cobalt	BARR	185512	SCMC	Active	21.84605619	44797	Yes
Nipissing Cobalt	FIRSTBROOK	186564	SCMC	Active	21.83409166	44797	Yes
Nipissing Cobalt	BARR	187070	SCMC	Active	21.84775345	44797	Yes
Nipissing Cobalt	BARR	187134	SCMC	Active	21.83409166	44847	Yes
Nipissing Cobalt	BARR	187135	SCMC	Active	21.83409166	44847	Yes
Nipissing Cobalt	BARR	187136	SCMC	Active	21.83580024	44847	Yes
Nipissing Cobalt	BARR	187137	SCMC	Active	21.83580024	44847	Yes
Nipissing Cobalt	KLOCK	187305	SCMC	Active	21.84091128	44797	Yes
Nipissing Cobalt	KLOCK	187306	SCMC	Active	21.84434134	44797	Yes
Nipissing Cobalt	BARR	189220	SCMC	Active	21.84091477	44797	Yes
Nipissing Cobalt	FIRSTBROOK	189786	SCMC	Active	21.83409516	44797	Yes
Nipissing Cobalt	FIRSTBROOK	189787	SCMC	Active	21.83921005	44797	Yes
Nipissing Cobalt	BARR	190593	SCMC	Active	21.84775694	44797	Yes
Nipissing Cobalt	BARR,FIRSTBROOK	190660	SCMC	Active	21.84263336	44797	Yes
Nipissing Cobalt	FIRSTBROOK	190951	SCMC	Active	21.84433784	44797	Yes
Nipissing Cobalt	KLOCK	191784	SCMC	Active	21.82555049	44797	Yes
Nipissing Cobalt	KLOCK	191785	SCMC	Active	21.83237773	44797	Yes
Nipissing Cobalt	BARR	191812	SCMC	Active	21.84946632	44847	Yes
Nipissing Cobalt	BARR	192256	SCMC	Active	21.8375087	44847	Yes
Nipissing Cobalt	KLOCK	192411	SCMC	Active	21.84945932	44797	Yes
Nipissing Cobalt	FIRSTBROOK	193262	SCMC	Active	21.8375052	44797	Yes
Nipissing Cobalt	FIRSTBROOK	193263	SCMC	Active	21.83921354	44797	Yes
Nipissing Cobalt	BARR	193686	SCMC	Active	21.84262986	44797	Yes
Nipissing Cobalt	KLOCK	193874	SCMC	Active	21.84604571	44797	Yes
Nipissing Cobalt	BARR	194631	SCMC	Active	21.84262986	44797	Yes
Nipissing Cobalt	FIRSTBROOK	197209	SCMC	Active	21.8460492	44797	Yes
Nipissing Cobalt	FIRSTBROOK	197210	SCMC	Active	21.84775694	44797	Yes
Nipissing Cobalt	FIRSTBROOK	197211	SCMC	Active	21.84775694	44797	Yes
Nipissing Cobalt	BARR	198547	SCMC	Active	21.83067415	44797	Yes
Nipissing Cobalt	KLOCK	198870	SCMC	Active	21.83580024	44797	Yes

Nipissing Cobalt	COLEMAN	199980	SCMC	Active	21.85459722	44797	Yes
Nipissing Cobalt	BARR	202518	SCMC	Active	21.84776394	44797	Yes
Nipissing Cobalt	FIRSTBROOK	202528	SCMC	Active	21.8460527	44797	Yes
Nipissing Cobalt	FIRSTBROOK	202756	SCMC	Active	21.8460492	44797	Yes
Nipissing Cobalt	FIRSTBROOK	202757	SCMC	Active	21.84776044	44797	Yes
Nipissing Cobalt	FIRSTBROOK	203112	SCMC	Active	21.84091128	44797	Yes
Nipissing Cobalt	FIRSTBROOK	203131	SCMC	Active	21.84263336	44797	Yes
Nipissing Cobalt	BARR	204356	SCMC	Active	21.83579675	44797	Yes
Nipissing Cobalt	BARR	206013	SCMC	Active	21.82725267	44797	Yes
Nipissing Cobalt	FIRSTBROOK	206971	SCMC	Active	21.84945932	44797	Yes
Nipissing Cobalt	COLEMAN,FIRSTBROOK	206972	SCMC	Active	16.11954294	44797	Yes
Nipissing Cobalt	FIRSTBROOK	206980	SCMC	Active	21.83580373	44797	Yes
Nipissing Cobalt	COLEMAN	208004	SCMC	Active	21.8580009	44797	Yes
Nipissing Cobalt	FIRSTBROOK	208309	SCMC	Active	21.84091477	44797	Yes
Nipissing Cobalt	FIRSTBROOK	208976	SCMC	Active	21.83237773	44797	Yes
Nipissing Cobalt	FIRSTBROOK	210429	SCMC	Active	21.84434483	44797	Yes
Nipissing Cobalt	BARR	210460	SCMC	Active	21.83580024	44847	Yes
Nipissing Cobalt	BARR	210461	SCMC	Active	21.83750171	44847	Yes
Nipissing Cobalt	FIRSTBROOK	210780	SCMC	Active	21.84091477	44797	Yes
Nipissing Cobalt	FIRSTBROOK	210839	SCMC	Active	21.84945932	44797	Yes
Nipissing Cobalt	FIRSTBROOK	210840	SCMC	Active	21.84945932	44797	Yes
Nipissing Cobalt	FIRSTBROOK	210841	SCMC	Active	21.85117207	44797	Yes
Nipissing Cobalt	BARR	211007	SCMC	Active	21.83408817	44797	Yes
Nipissing Cobalt	BARR	211008	SCMC	Active	21.8375052	44797	Yes
Nipissing Cobalt	KLOCK	211880	SCMC	Active	21.8460527	44797	Yes
Nipissing Cobalt	BARR	213119	SCMC	Active	21.84434134	44797	Yes
Nipissing Cobalt	COLEMAN	213890	SCMC	Active	21.85628338	44797	Yes
Nipissing Cobalt	FIRSTBROOK	214797	SCMC	Active	21.82896522	44797	Yes
Nipissing Cobalt	FIRSTBROOK	214819	SCMC	Active	21.83067765	44797	Yes
Nipissing Cobalt	BARR,FIRSTBROOK	215050	SCMC	Active	21.83409166	44797	Yes
Nipissing Cobalt	FIRSTBROOK	215051	SCMC	Active	21.82896522	44797	Yes
Nipissing Cobalt	FIRSTBROOK	215881	SCMC	Active	21.83580024	44797	Yes
Nipissing Cobalt	KLOCK	216599	SCMC	Active	21.83750521	44797	Yes
Nipissing Cobalt	KLOCK	216600	SCMC	Active	21.83922053	44797	Yes
Nipissing Cobalt	BARR	219171	SCMC	Active	21.8375052	44797	Yes
Nipissing Cobalt	BARR	219172	SCMC	Active	21.83921354	44797	Yes
Nipissing Cobalt	BARR	219173	SCMC	Active	21.84091128	44797	Yes
Nipissing Cobalt	FIRSTBROOK	219732	SCMC	Active	21.85117207	44797	Yes
Nipissing Cobalt	FIRSTBROOK	219733	SCMC	Active	21.85117557	44797	Yes
Nipissing Cobalt	COLEMAN,FIRSTBROOK	219734	SCMC	Active	21.85286897	44797	Yes
Nipissing Cobalt	FIRSTBROOK	219737	SCMC	Active	21.83408468	44797	Yes
Nipissing Cobalt	BARR	219923	SCMC	Active	21.84945932	44797	Yes

Nipissing Cobalt	BARR	219924	SCMC	Active	21.85117207	44797	Yes
Nipissing Cobalt	BARR,FIRSTBROOK	219973	SCMC	Active	21.83580024	44797	Yes
Nipissing Cobalt	BARR	219974	SCMC	Active	21.83921704	44797	Yes
Nipissing Cobalt	BARR,FIRSTBROOK	219979	SCMC	Active	21.84434134	44797	Yes
Nipissing Cobalt	COLEMAN	220070	SCMC	Active	19.31213189	44797	Yes
Nipissing Cobalt	FIRSTBROOK	220398	SCMC	Active	21.82896522	44797	Yes
Nipissing Cobalt	KLOCK	221687	SCMC	Active	21.82725617	44797	Yes
Nipissing Cobalt	FIRSTBROOK	222333	SCMC	Active	21.84263336	44797	Yes
Nipissing Cobalt	FIRSTBROOK	222334	SCMC	Active	21.84604221	44797	Yes
Nipissing Cobalt	FIRSTBROOK	222892	SCMC	Active	21.8460527	44797	Yes
Nipissing Cobalt	COLEMAN,FIRSTBROOK	222893	SCMC	Active	21.85287247	44797	Yes
Nipissing Cobalt	COLEMAN,FIRSTBROOK	223081	SCMC	Active	21.85286897	44797	Yes
Nipissing Cobalt	COLEMAN	223082	SCMC	Active	21.85628338	44797	Yes
Nipissing Cobalt	COLEMAN	223083	SCMC	Active	21.8580009	44797	Yes
Nipissing Cobalt	FIRSTBROOK	223135	SCMC	Active	21.83409166	44797	Yes
Nipissing Cobalt	FIRSTBROOK	223136	SCMC	Active	21.83750521	44797	Yes
Nipissing Cobalt	COLEMAN	223859	SCMC	Active	21.85459722	44797	Yes
Nipissing Cobalt	FIRSTBROOK	224352	SCMC	Active	21.84434134	44797	Yes
Nipissing Cobalt	FIRSTBROOK	224353	SCMC	Active	21.8460492	44797	Yes
Nipissing Cobalt	FIRSTBROOK	224414	SCMC	Active	21.84775694	44797	Yes
Nipissing Cobalt	FIRSTBROOK	224415	SCMC	Active	21.84775694	44797	Yes
Nipissing Cobalt	BARR,FIRSTBROOK	224416	SCMC	Active	21.84775694	44797	Yes
Nipissing Cobalt	FIRSTBROOK	224417	SCMC	Active	21.85116858	44797	Yes
Nipissing Cobalt	FIRSTBROOK	226482	SCMC	Active	21.84091827	44797	Yes
Nipissing Cobalt	FIRSTBROOK	226483	SCMC	Active	21.84263336	44797	Yes
Nipissing Cobalt	FIRSTBROOK	226484	SCMC	Active	21.84263685	44797	Yes
Nipissing Cobalt	BARR	227112	SCMC	Active	21.83408817	44797	Yes
Nipissing Cobalt	BARR	227113	SCMC	Active	21.83579675	44847	Yes
Nipissing Cobalt	BARR	227114	SCMC	Active	21.83750521	44847	Yes
Nipissing Cobalt	FIRSTBROOK	227186	SCMC	Active	21.85116858	44797	Yes
Nipissing Cobalt	COLEMAN,FIRSTBROOK	227187	SCMC	Active	21.85286547	44797	Yes
Nipissing Cobalt	BARR	228050	SCMC	Active	21.83237424	44797	Yes
Nipissing Cobalt	FIRSTBROOK	228372	SCMC	Active	21.83237074	44797	Yes
Nipissing Cobalt	FIRSTBROOK	229291	SCMC	Active	21.83238122	44797	Yes
Nipissing Cobalt	FIRSTBROOK	229648	SCMC	Active	21.84776044	44797	Yes
Nipissing Cobalt	FIRSTBROOK	229649	SCMC	Active	21.84775694	44797	Yes
Nipissing Cobalt	FIRSTBROOK	229650	SCMC	Active	21.84946282	44797	Yes
Nipissing Cobalt	FIRSTBROOK	229651	SCMC	Active	21.85117557	44797	Yes
Nipissing Cobalt	COLEMAN,FIRSTBROOK	229652	SCMC	Active	21.85287247	44797	Yes
Nipissing Cobalt	BARR	229694	SCMC	Active	21.84604571	44847	Yes
Nipissing Cobalt	COLEMAN	231230	SCMC	Active	21.85799391	44797	Yes
Nipissing Cobalt	COLEMAN	231245	SCMC	Active	21.86140935	44797	Yes

Nipissing Cobalt	COLEMAN	231898	SCMC	Active	21.85970781	44797	Yes
Nipissing Cobalt	FIRSTBROOK	232387	SCMC	Active	21.8460492	44797	Yes
Nipissing Cobalt	BARR,FIRSTBROOK	232388	SCMC	Active	21.8460492	44797	Yes
Nipissing Cobalt	FIRSTBROOK	232389	SCMC	Active	21.84946282	44797	Yes
Nipissing Cobalt	BARR,FIRSTBROOK	233561	SCMC	Active	21.83237773	44797	Yes
Nipissing Cobalt	BARR	233562	SCMC	Active	21.83237773	44797	Yes
Nipissing Cobalt	FIRSTBROOK	233583	SCMC	Active	21.83237773	44797	Yes
Nipissing Cobalt	FIRSTBROOK	234382	SCMC	Active	21.82895823	44797	Yes
Nipissing Cobalt	KLOCK	235147	SCMC	Active	21.83751219	44797	Yes
Nipissing Cobalt	KLOCK	235148	SCMC	Active	21.84434134	44797	Yes
Nipissing Cobalt	KLOCK	236684	SCMC	Active	21.8375087	44797	Yes
Nipissing Cobalt	KLOCK	236685	SCMC	Active	21.84262986	44797	Yes
Nipissing Cobalt	KLOCK	236686	SCMC	Active	21.84433784	44797	Yes
Nipissing Cobalt	FIRSTBROOK	238302	SCMC	Active	21.84091477	44797	Yes
Nipissing Cobalt	FIRSTBROOK	238303	SCMC	Active	21.8460492	44797	Yes
Nipissing Cobalt	BARR	238962	SCMC	Active	21.84945583	44797	Yes
Nipissing Cobalt	FIRSTBROOK	239864	SCMC	Active	21.84776044	44797	Yes
Nipissing Cobalt	BARR	240011	SCMC	Active	21.8460492	44797	Yes
Nipissing Cobalt	BARR	240012	SCMC	Active	21.8460492	44797	Yes
Nipissing Cobalt	BARR,FIRSTBROOK	240070	SCMC	Active	21.8375087	44797	Yes
Nipissing Cobalt	BARR	240075	SCMC	Active	21.84263336	44797	Yes
Nipissing Cobalt	BARR	240076	SCMC	Active	21.84434134	44797	Yes
Nipissing Cobalt	BARR,KLOCK	240906	SCMC	Active	21.83409516	44797	Yes
Nipissing Cobalt	BARR	241797	SCMC	Active	21.84091128	44797	Yes
Nipissing Cobalt	KLOCK	241835	SCMC	Active	21.82554699	44797	Yes
Nipissing Cobalt	BARR	241856	SCMC	Active	21.85116858	44847	Yes
Nipissing Cobalt	BARR	243189	SCMC	Active	21.82896173	44797	Yes
Nipissing Cobalt	COLEMAN	243254	SCMC	Active	21.8580009	44797	Yes
Nipissing Cobalt	FIRSTBROOK	243312	SCMC	Active	21.83409516	44797	Yes
Nipissing Cobalt	FIRSTBROOK	243313	SCMC	Active	21.84091128	44797	Yes
Nipissing Cobalt	COLEMAN	243372	SCMC	Active	21.86140236	44797	Yes
Nipissing Cobalt	FIRSTBROOK	244386	SCMC	Active	21.84774995	44797	Yes
Nipissing Cobalt	FIRSTBROOK	244540	SCMC	Active	21.84263685	44797	Yes
Nipissing Cobalt	BARR,FIRSTBROOK	244598	SCMC	Active	21.85117207	44797	Yes
Nipissing Cobalt	BARR	245679	SCMC	Active	21.83751219	44847	Yes
Nipissing Cobalt	FIRSTBROOK	246557	SCMC	Active	21.83238122	44797	Yes
Nipissing Cobalt	COLEMAN,KITTSO	246848	SCMC	Active	21.86140935	44847	Yes
Nipissing Cobalt	BARR	247170	SCMC	Active	21.83408468	44847	Yes
Nipissing Cobalt	BARR	247171	SCMC	Active	21.83751219	44847	Yes
Nipissing Cobalt	BARR,FIRSTBROOK	247369	SCMC	Active	21.84091477	44797	Yes
Nipissing Cobalt	FIRSTBROOK	247757	SCMC	Active	21.8375087	44797	Yes
Nipissing Cobalt	BARR	248916	SCMC	Active	21.83580024	44847	Yes

Nipissing Cobalt	BARR,KLOCK	248917	SCMC	Active	21.83580373	44797	Yes
Nipissing Cobalt	KLOCK	249092	SCMC	Active	21.84775345	44797	Yes
Nipissing Cobalt	KLOCK	249093	SCMC	Active	21.84945583	44797	Yes
Nipissing Cobalt	COLEMAN,FIRSTBROOK	250872	SCMC	Active	21.85286897	44797	Yes
Nipissing Cobalt	FIRSTBROOK	252712	SCMC	Active	21.82896871	44797	Yes
Nipissing Cobalt	BARR	252813	SCMC	Active	21.84262986	44797	Yes
Nipissing Cobalt	COLEMAN,FIRSTBROOK	252892	SCMC	Active	17.27479032	44797	Yes
Nipissing Cobalt	COLEMAN	252893	SCMC	Active	21.85460071	44797	Yes
Nipissing Cobalt	BARR,KLOCK	253148	SCMC	Active	21.8460527	44797	Yes
Nipissing Cobalt	BARR,KLOCK	253250	SCMC	Active	21.82555049	44797	Yes
Nipissing Cobalt	BARR	253251	SCMC	Active	21.82725267	44797	Yes
Nipissing Cobalt	FIRSTBROOK	253281	SCMC	Active	21.83921704	44797	Yes
Nipissing Cobalt	FIRSTBROOK	253282	SCMC	Active	21.83922053	44797	Yes
Nipissing Cobalt	FIRSTBROOK	253283	SCMC	Active	21.83921704	44797	Yes
Nipissing Cobalt	KLOCK	253485	SCMC	Active	21.83409166	44797	Yes
Nipissing Cobalt	KLOCK	253486	SCMC	Active	21.83409166	44797	Yes
Nipissing Cobalt	KLOCK	253954	SCMC	Active	21.83921704	44797	Yes
Nipissing Cobalt	KLOCK	253955	SCMC	Active	21.84263685	44797	Yes
Nipissing Cobalt	COLEMAN,KITTSON	254190	SCMC	Active	21.85970431	44847	Yes
Nipissing Cobalt	COLEMAN,KITTSON	254191	SCMC	Active	21.86141285	44847	Yes
Nipissing Cobalt	BARR	256734	SCMC	Active	21.84945932	44797	Yes
Nipissing Cobalt	FIRSTBROOK	256987	SCMC	Active	21.84604571	44797	Yes
Nipissing Cobalt	FIRSTBROOK	257171	SCMC	Active	21.85117557	44797	Yes
Nipissing Cobalt	FIRSTBROOK	257875	SCMC	Active	21.84091477	44797	Yes
Nipissing Cobalt	FIRSTBROOK	257876	SCMC	Active	21.84434134	44797	Yes
Nipissing Cobalt	KLOCK	258369	SCMC	Active	21.8255435	44797	Yes
Nipissing Cobalt	KLOCK	258370	SCMC	Active	21.82896522	44797	Yes
Nipissing Cobalt	BARR,KITTSON	258390	SCMC	Active	21.85286547	44847	Yes
Nipissing Cobalt	FIRSTBROOK	259162	SCMC	Active	21.84262986	44797	Yes
Nipissing Cobalt	BARR	259187	SCMC	Active	21.83409166	44847	Yes
Nipissing Cobalt	BARR	259188	SCMC	Active	21.83580373	44847	Yes
Nipissing Cobalt	BARR	259189	SCMC	Active	21.83579325	44847	Yes
Nipissing Cobalt	FIRSTBROOK	259281	SCMC	Active	21.83580024	44797	Yes
Nipissing Cobalt	COLEMAN	259738	SCMC	Active	21.8580009	44797	Yes
Nipissing Cobalt	FIRSTBROOK	259781	SCMC	Active	21.83579675	44797	Yes
Nipissing Cobalt	FIRSTBROOK	259782	SCMC	Active	15.47409302	44797	Yes
Nipissing Cobalt	FIRSTBROOK	259783	SCMC	Active	21.84091128	44797	Yes
Nipissing Cobalt	BARR	261816	SCMC	Active	21.83921704	44797	Yes
Nipissing Cobalt	BARR	261831	SCMC	Active	21.83921354	44797	Yes
Nipissing Cobalt	BARR	261832	SCMC	Active	21.84433784	44797	Yes
Nipissing Cobalt	BARR,FIRSTBROOK	262264	SCMC	Active	21.83067415	44797	Yes
Nipissing Cobalt	BARR	262265	SCMC	Active	21.83409166	44797	Yes

Nipissing Cobalt	BARR	265242	SCMC	Active	21.83751219	44847	Yes
Nipissing Cobalt	KITTSO	265844	SCMC	Active	21.85459372	44847	Yes
Nipissing Cobalt	BARR	266854	SCMC	Active	21.83409865	44797	Yes
Nipissing Cobalt	FIRSTBROOK	266912	SCMC	Active	21.83409166	44797	Yes
Nipissing Cobalt	FIRSTBROOK	266913	SCMC	Active	21.83580024	44797	Yes
Nipissing Cobalt	FIRSTBROOK	266914	SCMC	Active	21.83922053	44797	Yes
Nipissing Cobalt	COLEMAN	267239	SCMC	Active	21.85459722	44797	Yes
Nipissing Cobalt	FIRSTBROOK	267617	SCMC	Active	21.83237773	44797	Yes
Nipissing Cobalt	BARR	268621	SCMC	Active	21.84091128	44797	Yes
Nipissing Cobalt	BARR,KLOCK	268622	SCMC	Active	21.84091827	44797	Yes
Nipissing Cobalt	FIRSTBROOK	269087	SCMC	Active	21.8460527	44797	Yes
Nipissing Cobalt	FIRSTBROOK	269088	SCMC	Active	21.84776044	44797	Yes
Nipissing Cobalt	FIRSTBROOK	269089	SCMC	Active	21.84775345	44797	Yes
Nipissing Cobalt	FIRSTBROOK	269090	SCMC	Active	21.85117207	44797	Yes
Nipissing Cobalt	FIRSTBROOK	269091	SCMC	Active	21.85117207	44797	Yes
Nipissing Cobalt	FIRSTBROOK	269092	SCMC	Active	21.85117557	44797	Yes
Nipissing Cobalt	COLEMAN	269840	SCMC	Active	21.8580009	44797	Yes
Nipissing Cobalt	BARR	270227	SCMC	Active	21.83237773	44797	Yes
Nipissing Cobalt	FIRSTBROOK	270228	SCMC	Active	21.82896173	44797	Yes
Nipissing Cobalt	FIRSTBROOK	271764	SCMC	Active	21.83066717	44797	Yes
Nipissing Cobalt	FIRSTBROOK	271765	SCMC	Active	21.83237773	44797	Yes
Nipissing Cobalt	FIRSTBROOK	271832	SCMC	Active	21.83751219	44797	Yes
Nipissing Cobalt	FIRSTBROOK	273719	SCMC	Active	21.84091477	44797	Yes
Nipissing Cobalt	BARR	274328	SCMC	Active	21.83921354	44797	Yes
Nipissing Cobalt	FIRSTBROOK	274903	SCMC	Active	21.83580024	44797	Yes
Nipissing Cobalt	FIRSTBROOK	275592	SCMC	Active	21.83237773	44797	Yes
Nipissing Cobalt	FIRSTBROOK	275818	SCMC	Active	21.84434134	44797	Yes
Nipissing Cobalt	BARR	275841	SCMC	Active	21.83409166	44847	Yes
Nipissing Cobalt	FIRSTBROOK	276030	SCMC	Active	21.85117207	44797	Yes
Nipissing Cobalt	FIRSTBROOK	276432	SCMC	Active	21.83921354	44797	Yes
Nipissing Cobalt	COLEMAN,KITTSO	276595	SCMC	Active	21.86140935	44847	Yes
Nipissing Cobalt	FIRSTBROOK	276788	SCMC	Active	21.84091477	44797	Yes
Nipissing Cobalt	FIRSTBROOK	276789	SCMC	Active	21.8460492	44797	Yes
Nipissing Cobalt	KLOCK	276893	SCMC	Active	21.82725267	44797	Yes
Nipissing Cobalt	BARR	276906	SCMC	Active	21.85116858	44847	Yes
Nipissing Cobalt	KITTSO	277944	SCMC	Active	21.85970781	44847	Yes
Nipissing Cobalt	BARR	278221	SCMC	Active	21.83068114	44797	Yes
Nipissing Cobalt	COLEMAN	278289	SCMC	Active	21.85460071	44797	Yes
Nipissing Cobalt	COLEMAN	278290	SCMC	Active	21.85628688	44797	Yes
Nipissing Cobalt	FIRSTBROOK	278359	SCMC	Active	21.83751219	44797	Yes
Nipissing Cobalt	FIRSTBROOK	278360	SCMC	Active	21.83921704	44797	Yes
Nipissing Cobalt	FIRSTBROOK	278361	SCMC	Active	21.84091477	44797	Yes

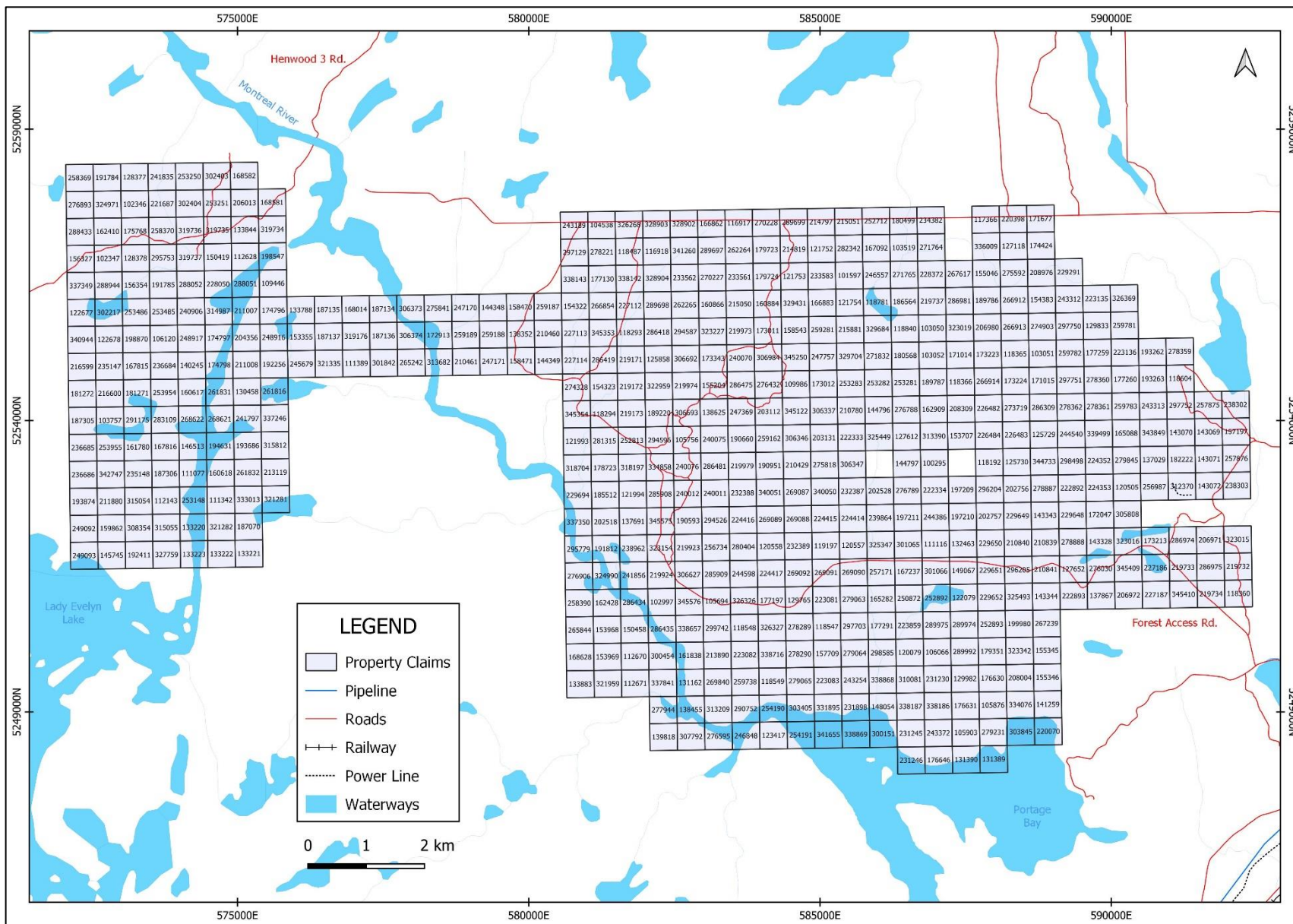
Nipissing Cobalt	FIRSTBROOK	278362	SCMC	Active	21.84091827	44797	Yes
Nipissing Cobalt	FIRSTBROOK	278887	SCMC	Active	21.8460492	44797	Yes
Nipissing Cobalt	FIRSTBROOK	278888	SCMC	Active	21.84946282	44797	Yes
Nipissing Cobalt	COLEMAN,FIRSTBROOK	279063	SCMC	Active	21.85286897	44797	Yes
Nipissing Cobalt	COLEMAN	279064	SCMC	Active	21.85628338	44797	Yes
Nipissing Cobalt	COLEMAN	279065	SCMC	Active	21.8580044	44797	Yes
Nipissing Cobalt	COLEMAN	279231	SCMC	Active	21.86141285	44797	Yes
Nipissing Cobalt	FIRSTBROOK	279845	SCMC	Active	21.84433784	44797	Yes
Nipissing Cobalt	BARR,FIRSTBROOK	280404	SCMC	Active	21.84945932	44797	Yes
Nipissing Cobalt	BARR	281315	SCMC	Active	21.84264035	44797	Yes
Nipissing Cobalt	FIRSTBROOK	282342	SCMC	Active	21.83067415	44797	Yes
Nipissing Cobalt	KLOCK	283109	SCMC	Active	21.84091477	44797	Yes
Nipissing Cobalt	BARR	285908	SCMC	Active	21.8460492	44797	Yes
Nipissing Cobalt	BARR	285909	SCMC	Active	21.85117207	44797	Yes
Nipissing Cobalt	FIRSTBROOK	286309	SCMC	Active	21.84091477	44797	Yes
Nipissing Cobalt	BARR	286418	SCMC	Active	21.83580024	44797	Yes
Nipissing Cobalt	BARR	286419	SCMC	Active	21.83751569	44797	Yes
Nipissing Cobalt	BARR,COLEMAN,KITTSO	286434	SCMC	Active	21.85286547	44847	Yes
Nipissing Cobalt	COLEMAN,KITTSO	286435	SCMC	Active	21.85459722	44847	Yes
Nipissing Cobalt	BARR,FIRSTBROOK	286475	SCMC	Active	21.83921704	44797	Yes
Nipissing Cobalt	BARR	286481	SCMC	Active	21.84434134	44797	Yes
Nipissing Cobalt	FIRSTBROOK	286974	SCMC	Active	21.84946282	44797	Yes
Nipissing Cobalt	FIRSTBROOK	286975	SCMC	Active	21.85117207	44797	Yes
Nipissing Cobalt	FIRSTBROOK	286981	SCMC	Active	21.83409166	44797	Yes
Nipissing Cobalt	BARR	288051	SCMC	Active	21.83237424	44797	Yes
Nipissing Cobalt	BARR,KLOCK	288052	SCMC	Active	21.83238122	44797	Yes
Nipissing Cobalt	KLOCK	288433	SCMC	Active	21.82896173	44797	Yes
Nipissing Cobalt	KLOCK	288944	SCMC	Active	21.83238122	44797	Yes
Nipissing Cobalt	BARR	289697	SCMC	Active	21.83067415	44797	Yes
Nipissing Cobalt	BARR	289698	SCMC	Active	21.83409166	44797	Yes
Nipissing Cobalt	FIRSTBROOK	289699	SCMC	Active	21.82896871	44797	Yes
Nipissing Cobalt	COLEMAN	289974	SCMC	Active	20.32993067	44797	Yes
Nipissing Cobalt	COLEMAN	289975	SCMC	Active	11.38958977	44797	Yes
Nipissing Cobalt	COLEMAN	289992	SCMC	Active	21.85628338	44797	Yes
Nipissing Cobalt	COLEMAN,KITTSO	290752	SCMC	Active	21.85970781	44847	Yes
Nipissing Cobalt	KLOCK	291175	SCMC	Active	21.84091477	44797	Yes
Nipissing Cobalt	BARR	294526	SCMC	Active	21.84775694	44797	Yes
Nipissing Cobalt	BARR	294587	SCMC	Active	21.83580024	44797	Yes
Nipissing Cobalt	BARR	294596	SCMC	Active	21.84263336	44797	Yes
Nipissing Cobalt	KLOCK	295753	SCMC	Active	21.83067415	44797	Yes
Nipissing Cobalt	BARR	295779	SCMC	Active	21.84945583	44847	Yes
Nipissing Cobalt	FIRSTBROOK	296204	SCMC	Active	21.8460527	44797	Yes

Nipissing Cobalt	FIRSTBROOK	296205	SCMC	Active	21.85117207	44797	Yes
Nipissing Cobalt	BARR	297129	SCMC	Active	21.83067066	44797	Yes
Nipissing Cobalt	COLEMAN	297703	SCMC	Active	21.85459722	44797	Yes
Nipissing Cobalt	FIRSTBROOK	297750	SCMC	Active	21.83580373	44797	Yes
Nipissing Cobalt	FIRSTBROOK	297751	SCMC	Active	13.1256539	44797	Yes
Nipissing Cobalt	FIRSTBROOK	297752	SCMC	Active	21.84091827	44797	Yes
Nipissing Cobalt	FIRSTBROOK	298498	SCMC	Active	21.84434483	44797	Yes
Nipissing Cobalt	COLEMAN	298585	SCMC	Active	21.85628688	44797	Yes
Nipissing Cobalt	COLEMAN	299742	SCMC	Active	21.85459722	44797	Yes
Nipissing Cobalt	COLEMAN	300151	SCMC	Active	21.86141285	44797	Yes
Nipissing Cobalt	KITTSOON	300454	SCMC	Active	21.85628338	44847	Yes
Nipissing Cobalt	FIRSTBROOK	301065	SCMC	Active	21.84945932	44797	Yes
Nipissing Cobalt	FIRSTBROOK	301066	SCMC	Active	21.85116508	44797	Yes
Nipissing Cobalt	BARR	301842	SCMC	Active	21.8375087	44847	Yes
Nipissing Cobalt	KLOCK	302217	SCMC	Active	21.83409516	44797	Yes
Nipissing Cobalt	BARR	302403	SCMC	Active	21.8255435	44797	Yes
Nipissing Cobalt	BARR,KLOCK	302404	SCMC	Active	21.82725966	44797	Yes
Nipissing Cobalt	COLEMAN,KITTSOON	303405	SCMC	Active	21.85971131	44847	Yes
Nipissing Cobalt	COLEMAN	303845	SCMC	Active	21.86140935	44797	Yes
Nipissing Cobalt	FIRSTBROOK	305808	SCMC	Active	21.84775345	44797	Yes
Nipissing Cobalt	FIRSTBROOK	306337	SCMC	Active	21.84091477	44797	Yes
Nipissing Cobalt	FIRSTBROOK	306346	SCMC	Active	21.84263685	44797	Yes
Nipissing Cobalt	FIRSTBROOK	306347	SCMC	Active	21.84434134	44797	Yes
Nipissing Cobalt	BARR	306373	SCMC	Active	21.83409516	44847	Yes
Nipissing Cobalt	BARR	306374	SCMC	Active	21.83580373	44847	Yes
Nipissing Cobalt	BARR	306627	SCMC	Active	21.85117207	44797	Yes
Nipissing Cobalt	BARR	306692	SCMC	Active	21.8375087	44797	Yes
Nipissing Cobalt	BARR	306693	SCMC	Active	21.84091477	44797	Yes
Nipissing Cobalt	FIRSTBROOK	306984	SCMC	Active	21.83750521	44797	Yes
Nipissing Cobalt	KITTSOON	307792	SCMC	Active	21.86140935	44847	Yes
Nipissing Cobalt	KLOCK	308354	SCMC	Active	21.84775694	44797	Yes
Nipissing Cobalt	COLEMAN	310081	SCMC	Active	21.8580009	44797	Yes
Nipissing Cobalt	FIRSTBROOK	312370	SCMC	Active	21.8460527	44797	Yes
Nipissing Cobalt	COLEMAN,KITTSOON	313209	SCMC	Active	21.85970781	44847	Yes
Nipissing Cobalt	FIRSTBROOK	313390	SCMC	Active	21.84262637	44797	Yes
Nipissing Cobalt	BARR	313682	SCMC	Active	21.8375087	44847	Yes
Nipissing Cobalt	BARR	314987	SCMC	Active	21.83408817	44797	Yes
Nipissing Cobalt	KLOCK	315054	SCMC	Active	21.8460492	44797	Yes
Nipissing Cobalt	KLOCK	315055	SCMC	Active	21.84775694	44797	Yes
Nipissing Cobalt	BARR	315812	SCMC	Active	21.84263336	44797	Yes
Nipissing Cobalt	BARR	318197	SCMC	Active	21.84433784	44797	Yes
Nipissing Cobalt	BARR	318704	SCMC	Active	21.84433784	44797	Yes

Nipissing Cobalt	BARR	319176	SCMC	Active	21.83580024	44847	Yes
Nipissing Cobalt	BARR	319734	SCMC	Active	21.82896522	44797	Yes
Nipissing Cobalt	BARR	319735	SCMC	Active	21.82896173	44797	Yes
Nipissing Cobalt	BARR,KLOCK	319736	SCMC	Active	21.82896871	44797	Yes
Nipissing Cobalt	BARR,KLOCK	319737	SCMC	Active	21.83067765	44797	Yes
Nipissing Cobalt	BARR	321281	SCMC	Active	21.8460492	44797	Yes
Nipissing Cobalt	BARR	321282	SCMC	Active	21.84775345	44797	Yes
Nipissing Cobalt	BARR	321335	SCMC	Active	21.8375087	44847	Yes
Nipissing Cobalt	KITSON	321959	SCMC	Active	21.85800789	44847	Yes
Nipissing Cobalt	BARR	322959	SCMC	Active	21.83921704	44797	Yes
Nipissing Cobalt	FIRSTBROOK	323015	SCMC	Active	21.84945932	44797	Yes
Nipissing Cobalt	FIRSTBROOK	323016	SCMC	Active	21.84945583	44797	Yes
Nipissing Cobalt	FIRSTBROOK	323019	SCMC	Active	21.83580024	44797	Yes
Nipissing Cobalt	BARR	323154	SCMC	Active	21.84945932	44797	Yes
Nipissing Cobalt	BARR	323227	SCMC	Active	21.83580024	44797	Yes
Nipissing Cobalt	COLEMAN	323342	SCMC	Active	21.85628338	44797	Yes
Nipissing Cobalt	KLOCK	324971	SCMC	Active	21.82725966	44797	Yes
Nipissing Cobalt	BARR	324990	SCMC	Active	21.85117907	44847	Yes
Nipissing Cobalt	FIRSTBROOK	325347	SCMC	Active	21.84946282	44797	Yes
Nipissing Cobalt	FIRSTBROOK	325449	SCMC	Active	21.84263685	44797	Yes
Nipissing Cobalt	COLEMAN,FIRSTBROOK	325493	SCMC	Active	21.85286897	44797	Yes
Nipissing Cobalt	BARR	326268	SCMC	Active	21.82896173	44797	Yes
Nipissing Cobalt	BARR,COLEMAN,FIRSTBROOK	326326	SCMC	Active	21.85286897	44797	Yes
Nipissing Cobalt	COLEMAN	326327	SCMC	Active	21.85459372	44797	Yes
Nipissing Cobalt	FIRSTBROOK	326369	SCMC	Active	21.83408817	44797	Yes
Nipissing Cobalt	KLOCK	327759	SCMC	Active	21.84945932	44797	Yes
Nipissing Cobalt	BARR	328902	SCMC	Active	21.82896522	44797	Yes
Nipissing Cobalt	BARR	328903	SCMC	Active	21.82896522	44797	Yes
Nipissing Cobalt	BARR	328904	SCMC	Active	21.83237773	44797	Yes
Nipissing Cobalt	FIRSTBROOK	329431	SCMC	Active	21.83409516	44797	Yes
Nipissing Cobalt	FIRSTBROOK	329684	SCMC	Active	21.83580373	44797	Yes
Nipissing Cobalt	FIRSTBROOK	329704	SCMC	Active	21.8375087	44797	Yes
Nipissing Cobalt	COLEMAN	331895	SCMC	Active	21.85970781	44797	Yes
Nipissing Cobalt	BARR	333013	SCMC	Active	21.84604571	44797	Yes
Nipissing Cobalt	COLEMAN	334076	SCMC	Active	21.85970781	44797	Yes
Nipissing Cobalt	BARR	334858	SCMC	Active	21.84434134	44797	Yes
Nipissing Cobalt	FIRSTBROOK	336009	SCMC	Active	21.83067765	44797	Yes
Nipissing Cobalt	BARR	337246	SCMC	Active	21.84091477	44797	Yes
Nipissing Cobalt	KLOCK	337349	SCMC	Active	21.83237424	44797	Yes
Nipissing Cobalt	BARR	337350	SCMC	Active	21.84775345	44847	Yes
Nipissing Cobalt	KITSON	337841	SCMC	Active	21.8580009	44847	Yes
Nipissing Cobalt	BARR	338142	SCMC	Active	21.83237424	44797	Yes

Nipissing Cobalt	BARR	338143	SCMC	Active	21.83237424	44797	Yes
Nipissing Cobalt	COLEMAN	338186	SCMC	Active	21.85970081	44797	Yes
Nipissing Cobalt	COLEMAN	338187	SCMC	Active	21.85970781	44797	Yes
Nipissing Cobalt	COLEMAN,KITSON	338657	SCMC	Active	21.85459722	44847	Yes
Nipissing Cobalt	COLEMAN	338716	SCMC	Active	21.85627988	44797	Yes
Nipissing Cobalt	COLEMAN	338868	SCMC	Active	21.8580044	44797	Yes
Nipissing Cobalt	COLEMAN	338869	SCMC	Active	21.86140935	44847	Yes
Nipissing Cobalt	FIRSTBROOK	339499	SCMC	Active	21.84263336	44797	Yes
Nipissing Cobalt	FIRSTBROOK	340050	SCMC	Active	21.8460492	44797	Yes
Nipissing Cobalt	FIRSTBROOK	340051	SCMC	Active	21.84604571	44797	Yes
Nipissing Cobalt	KLOCK	340944	SCMC	Active	21.83579675	44797	Yes
Nipissing Cobalt	BARR	341260	SCMC	Active	21.83067415	44797	Yes
Nipissing Cobalt	COLEMAN,KITSON	341655	SCMC	Active	21.86140935	44847	Yes
Nipissing Cobalt	KLOCK	342747	SCMC	Active	21.84434483	44797	Yes
Nipissing Cobalt	FIRSTBROOK	343849	SCMC	Active	21.84262986	44797	Yes
Nipissing Cobalt	FIRSTBROOK	344733	SCMC	Active	21.84434134	44797	Yes
Nipissing Cobalt	FIRSTBROOK	345122	SCMC	Active	21.84091827	44797	Yes
Nipissing Cobalt	FIRSTBROOK	345250	SCMC	Active	21.83751219	44797	Yes
Nipissing Cobalt	BARR	345353	SCMC	Active	21.83580723	44797	Yes
Nipissing Cobalt	BARR	345354	SCMC	Active	21.84091128	44797	Yes
Nipissing Cobalt	FIRSTBROOK	345409	SCMC	Active	21.85116858	44797	Yes
Nipissing Cobalt	COLEMAN,FIRSTBROOK	345410	SCMC	Active	21.85287247	44797	Yes
Nipissing Cobalt	BARR	345575	SCMC	Active	21.84775694	44797	Yes
Nipissing Cobalt	BARR,COLEMAN	345576	SCMC	Active	21.85286897	44797	Yes
Nipissing Cobalt	COLEMAN	131389	SCMC	Active	21.86313001	44797	No
Nipissing Cobalt	COLEMAN	131390	SCMC	Active	21.86312652	44797	No
Nipissing Cobalt	COLEMAN	176646	SCMC	Active	21.86311952	44797	No
Nipissing Cobalt	COLEMAN	231246	SCMC	Active	21.86312652	44797	No

Figure 2: Nipissing Cobalt Claim Map



REGIONAL AND PROPERTY GEOLOGY

The geology of the Nipissing Cobalt property is largely understood from mapping by Ontario Geological Survey geologists Johns and Van Steenburgh (1984) and from a comprehensive compilation Map P.3851 (Ayer et al., 2006). The property is underlain by flat-lying sedimentary rocks (mudstones, siltstones, sandstones, and diamictites) of the Huronian Supergroup which rest unconformably on Archean volcanic and sedimentary rocks that are correlative with the Abitibi Subprovince. The Huronian rocks and Archean rocks have been intruded by 2219 Ma Nipissing diabase and gabbro sills.

Archean Rock Types and Exposures

The Archean volcanic and sedimentary rocks are exposed in one small inlier (known as the Firstbrook Inlier) in the east-central portion of the property between McLaren Lake and Maggie Lake in Firstbrook Township (approximate UTM NAD83 coordinates 587,900 mE, 5,251,550 mN) where the Huronian cover rocks have been eroded. The volcanic rocks are completely enclosed within siltstone and shale of the Gowganda Formation (Firstbrook Member). The dominant lithologies exposed in the Firstbrook Inlier are massive felsic volcanics (rhyolite), feldspar porphyry, tuff, lapilli tuff, and tuff breccia. Volcanic bombs are rare and localized within the felsic volcanics but are up to 5 cm wide and composed of either rhyolite or hornblende-rich porphyry. A pervasive induration or weak silicification of the rhyolite has taken place, making the rhyolite appear bleached (especially the bombs), very hard in places, and locally having a vuggy texture in veins and along vein margins. Weak, selective sericitization of the feldspars has occurred within the porphyry units.

Proterozoic Rock Types and Exposures

The Proterozoic rocks of the Cobalt Embayment in the vicinity of the reconnaissance work area are comprised of a relatively flat-lying succession of diamictite, shale, siltstone, and sandstone belonging to the Cobalt Group which are intruded by Nipissing gabbro dykes & sills and Sudbury dykes. Metamorphic grade is low (sub-greenschist), except where intruded by the Nipissing gabbro and contact metamorphism locally increases the metamorphic grade to amphibolitic. Structurally, the Proterozoic strata are nearly flat-lying, but large-scale, broad, open folds have been mapped and north-west trending normal faults (i.e. the Montreal River and Latchford faults) may locally distort or offset bedding vertically, though very little lateral displacement has been observed on these faults. Total thickness of all Proterozoic units may be as little as a couple of meters to over 1,300 m in the area of interest, but is generally no more than a few hundred meters thick in total throughout most of the region.

Gowganda Formation

The Gowganda Formation in the area of interest is divided into the Coleman and Firstbrook members. The Coleman Member unconformably drapes the Archean basement and is comprised of wide-spread poorly-sorted basal diamictites (both clast-supported and matrix-supported), massive and stratified diamictites, and pebbly and non-pebbly shaley mudstones with interlaminated siltstone and sandstone beds, which mark the top of the member. The Coleman Member was observed by geologists at a number of outcrops across the area of interest. North of the NE Temagami inlier, the Coleman Member can have a thickness of zero to 430 m (Born & Hitch 1988) but is generally no thicker than 100 m in the vicinity of Highway 11

(Thomson 1968). The Firstbrook Member conformably overlies the Coleman Member. This rock unit consists of a coarsening-upward sequence of mudstone, siltstone, and minor very fine sandstone. Interlaminated shaley mudstone and siltstone is the most common facies of the member, and colour ranges from greyish-green at the base of the member to purplish-red at the top of the member. The unit was most commonly seen by Tri Origin geologists as interlaminated grey-green and/or purple-red shaley mudstone and siltstone. Outcroppings of the Firstbrook Member to the west of the Archean inlier are nearly flat-lying, generally dipping 8° to 12° and locally up to 20°, with varying strikes. The Firstbrook Member in this area is composed of finely laminated mudstones and siltstones with laminations generally less than 5mm thick. The mudstones often have a grey-green colour whereas the siltstones are often a reddish-purple colour (indicating iron oxide or hematite).

Lorrain Formation

The Lorrain Formation conformably overlies the Firstbrook Member and consists of a lower well-sorted, horizontally laminated, fine-grained, thickly bedded arkose grading up into laminated shaley mudstones, siltstones, and sandstones, which grade up into moderately- to poorly-sorted, medium grained coarsening-upward arkose and arenite. The Lorrain Formation is not very widespread and is only locally preserved, but is up to 610 m thick in the area north of the NE Temagami inlier (Born & Hitch 1988). The Lorrain Formation was observed as flat-lying thick beds of grey to pinkish-grey arkose, with both planar and large scale (up to 30 cm) cross-bedding sets.

Intrusions and Dykes

The Nipissing intrusions (2219 Ma) form dozens of dykes and sills across the entire Cobalt Embayment area. Within the Best area, the sills may reach a maximum thickness of 500 m. The intrusions are predominantly comprised of coarse-grained quartz diabase and hypersthene gabbro. Quartz gabbro, varied-textured gabbro, and granophyre are less common.

The Sudbury dykes (1235 Ma) are mentioned here as they are highly magnetic and are readily visible on airborne magnetic surveys. The dykes are reported to be between 3 and 30 m wide. Where observed by Tri Origin geologists, the dykes are no more than several meters wide and are vertically dipping.

Both the Huronian Supergroup sediments and Archean rocks have been intruded by Proterozoic-aged Nipissing diabase and gabbro sills. These are largely exposed on the southeastern corner of the property at McLaren Mountain, south of McLaren Lake.

Kimberlites

Since the resurgence of diamond exploration during the 1970's-1980's, multiple diamondiferous kimberlites have been positively identified with the aid of modernized geophysical exploration techniques. Accelerated exploration for diamondiferous kimberlite pipes in the Cobalt area continued in 2017, with focus by RJK Exploration where more than 20 kimberlite targets have been identified. In 2019, De Beers Canada optioned ground on the Nipissing Cobalt property and conducted a short single-hole drill program with minor till sampling. This short program positively identified a kimberlite pipe in the northeastern portion of the property, which further warranted the need to reanalyze and interpret previously completed geophysical data for kimberlite targets on the Nipissing Cobalt and South Abitibi properties.

HISTORIC EXPLORATION ACTIVITIES

The Ontario Geological Survey conducted a geological mapping program in 1979 across Firstbrook, Barr, Kittson, and Coleman townships to the north shore of Bay Lake (Map 2474, Johns and Van Steenburgh, 1984). The OGS also conducted a UTEM survey across the whole area of interest in 1987 (Hanneson and Huxter, 1986, 1987, 1988, 1989, 1991; Hanneson, Huxter, and Rowe, 1989; Hanneson and Rowe, 1989). The UTEM survey was also accompanied by a small (1:20,000 scale) Bouguer gravity survey around the McLaren Lake area (P 3147, Hanneson and Rowe, 1989). In the following text, the Firstbrook area refers to the eastern portion of the Nipissing Cobalt property claim block.

The first recorded exploration programs on the Nipissing Cobalt property area were in 1948 and 1957, and both programs consisted of geologic mapping and prospecting. Two programs conducted by Copperfields Mining were completed during the 1970s, and they consisted of geologic mapping, ground magnetics survey, and a VLF survey. Both programs were conducted on and around the Archean volcanics inlier at McLaren Lake and the company was targeting copper mineralization. In 1980, St Joseph Exploration conducted a geologic mapping program near McLaren Lake, and was likely the company to have blasted out the exploration pits and shafts near McLaren Lake, discovered in June 2016. In 1981, Agnico-Eagle Mines began exploring between Eisen Lake (southwest of McLaren Lake) and Portage Bay. Agnico flew an airborne VLF-EM survey in 1982, conducted a UTEM survey over the west side of Bay Lake in 1989 (this survey was planned as a southern extension of the UTEM survey conducted by the OGS), and drilled 4 diamond drill holes in 1981, 2 holes in 1982, and 4 holes in 1989. The only holes to intersect the Archean volcanics were the 1989 drill holes near Pork Rapids (Montreal River) at the southwest corner of the Firstbrook area (between 60 and 103 m depth). R. I. Benner conducted a ground VLF survey in 1982 in the McLaren Lake area. The Benner property was optioned by Hudson Bay Mines in 1983 and eight diamond drill holes were drilled. All but 2 of these holes intersected Archean volcanics between 36 m and 344 m. Legacy Exploration continued the Benner project in 1986 with a ground magnetometer survey and 24 drill holes (of which 9 holes intersected the Archean between 25 and 400 m depth). In 1988, Bethlehem Resources continued work around McLaren Lake and produced a geologic map. Quote Resources performed a small ground magnetometer and VLF-EM survey near Forest Access Road west of L52+00E in 1989.

In 1990 and 1991, G. Chitaroni completed geologic mapping programs around McLaren Creek and Highway 558 (north of the TA-1 area). R. Benner drilled 1 diamond drill hole in 1990 which hit Archean rocks at 155 m depth. In 1993, Falconbridge flew a GeoTEM survey which was followed up with 5 diamond drill holes targeting Archean basement conductors (2 holes had downhole EM surveys performed, but data is only available for one of the holes, COL-05). The northwestern portion of Falconbridge's GeoTEM survey covers the entire Firstbrook area of interest, but some of the EM anomalies from the Falconbridge survey do not correlate with the EM anomalies from the Tri Origin-Sumitomo Alliance VTEM Survey conducted during 2015/16. The Falconbridge holes intersected Archean rocks in 3 holes. In 1995, Consolidated Pine Channel Gold Corp. flew an airborne magnetics survey (targeting kimberlites). Between 1995 and 1998, Silver Century explored north of the Firstbrook area near Highway 558 using ground gravity, magnetics, and two diamond drill holes (one of which was wedged and extended to

1602 m). In 1997, Silver Century drilled 3 holes east of McLaren Creek; these holes intersected Archean rocks between 417 and 469 m depth. During the summer months of 2002, Universal Power Corporation drilled 464.2 meters in 6 diamond drill holes along the western margin of Lady Evelyn River. A total of 72 core samples were taken during the program with high-grade zinc intercepts reported in two drill holes including a wide intercept of 21.2 meters of 0.415% Zn. Sudbury Contact Mines performed work just northwest of the property in 2002 and 2003 (airborne magnetics and 4 drill holes). Part of Tres-Or's 2003 ground magnetics and till sampling survey fell on the Firstbrook area (at Pork Rapids and McLaren Lake), but Tres-Or was targeting kimberlite pipes. Tres-Or continued diamond exploration in the area between 2004 and 2005, conducting geological mapping and geochemistry surveys. Temex flew an airborne magnetics survey over part of the Nipissing Cobalt property in 2006, and conducted till sampling in the same year. In 2006, two diamond drill holes targeting kimberlite pipes were drilled west of McLaren Creek (one drill hole hit Archean volcanics at 110 m depth).

A total of 58 diamond drill holes (plus one hole that was extended/wedged from an earlier hole) were drilled on the Firstbrook area of interest. Of these holes, 27 holes intersected Archean volcanic rocks, interflow sediments, or both. Most of these holes occur between McLaren and Maggie Lake near the Archean inlier on the Forest Access Road (at vertical depths of 18m to 306m), but drill holes have also intersected Archean rocks on the southwest side of McLaren Mountain (at vertical depths of 301m to 375m), west side of McLaren Creek (78 m depth), and east of Pork Rapids (at vertical depths of 52m to 75m). The most common lithologies encountered in the drill logs describe the Archean volcanics as felsic to intermediate (or rhyolitic to andesitic) massive flows, pillowed flows, tuffs, fragmental volcanic breccia, and generic "lavas" and "flows", with occasional pyrite, quartz-calcite veins, and minor epidote. The same drill logs describe the Archean sedimentary and interflow sedimentary rocks as argillite or greywacke, sometimes carbonaceous or graphitic and occasionally cherty or siliceous. Of the diamond drill holes that successfully intersected Archean rocks, only about 10 of them were drilled to target EM conductors (holes drilled by Agnico-Eagle in 1989, Silver Century in 1997, Falconbridge in 1993, and Conwest). Trace pyrite or trace to minor graphite was encountered in only half of these holes, while the other 5 holes did not intersect any unit that would have explained the EM conductor they were targeting. Falconbridge hole COL-05 was the only hole to intersect sulphide (minor semi-massive pyrite).

Most of the aforementioned programs targeted Nipissing-related silver-nickel-cobalt quartz-carbonate veins in the early 1980s, although toward the end of the 1980s and 1990s explorers were targeting the basement Archean rocks for mineralization (i.e. Agnico-Eagle, Falconbridge, and Silver Century). In the 1990s and 2000s, exploration targets shifted with a focus toward exploring for kimberlites and diamonds, rather than gold and base metals (i.e. Consolidated Pine, Tres-Or, and Temex).

Work Completed by Tri Origin Exploration Ltd.

Since acquiring the property in 2015, Tri Origin has completed preliminary mapping and sampling programs, a diamond drill program in conjunction with Sumitomo Metals, flown a VTEM airborne geophysical survey, and conducted a ground geophysical IP survey, mainly in search for gold and base metal mineralization. The property was optioned to Metals Tech in 2018 (Bay Lake North Cobalt Project) in search for cobalt mineralization, completing field

sampling and a short drill program. Reporting for the work program was not completed by Metals Tech. Portion of the Nipissing Cobalt property was optioned to De Beers Canada during 2019, who completed a single hole diamond drill program in search for diamondiferous kimberlite pipes on the Nipissing Cobalt property.

CURRENT PROGRAM

2021 Data Processing and Analysis

During the Spring of 2021, between April and June, NewOrigin Gold Corp contracted Condor Consulting Inc to reprocess and analyze airborne geophysical data completed during 2015/2016 by GeoTech, to better define possible kimberlite targets across the Nipissing Cobalt and South Abitibi Properties. Supervision of the work completed was done by Dr. Robert Valliant, while Project Geologist, Zachary Matheson will complete interpretations and analysis of the results produced by Condor Consulting.

Condor Consulting Inc. completed a report for the reprocessing of the airborne VTEM geophysical survey titled "Report on Processing and Analysis of Five VTEM EM and Magnetic Surveys, Nipissing Cobalt and South Abitibi Properties, Ontario" which is appended in Appendix A. The report completed by Condor outlines all parameters involved with the reprocessing and analysis of the airborne geophysical data in order to outline possible kimberlite pipes by means of the Keating Analysis, and additional geophysical survey products.

Conclusions & Recommendations

Based on the results presented by Condor Consulting, the work completed on EM and Magnetic data has positively identified numerous kimberlite targets which show typical geometries and correlate well with expected EM responses. Many of these targets have not been tested by drilling and follow up work is required.

It is recommended that once prioritized targets are identified, an extensive till sampling program be completed in a down ice glaciation pattern within the Nipissing Cobalt and South Abitibi properties in search for positive KIMs (kimberlite indicator minerals). Depending on the results, this should then be followed up with diamond drilling to test the potential for diamondiferous kimberlites on these prioritized targets.

REFERENCES

- Ayer JA, Chartrand JE, Grabowski GPB, Josey SD, Rainsford DRB, Trowell NF. 2006. Geological Compilation of the Cobalt-Temagami Area, Abitibi Greenstone Belt. Ontario (ON): Ministry of Energy, Northern Development and Mines. Ontario Geological Survey Publication: P3581. Preliminary Map Series. Scale 1: 100 000.
- Born P, Hitch MW. 1990. Precambrian Geology, Bay Lake Area. Ontario (ON): Ministry of Energy, Northern Development and Mines. Ontario Geological Survey Publication: R276. 5-12p.
- Hanneson, J. E., and Huxter, R. S. 1986. The Detection and Mapping of Basement Conductors Under Areas Covered by Thick Huronian Sedimentary Rocks, District of Timiskaming; p.225-233, in Summary of Field Work and Other Activities, 1986, by the Ontario Geological Survey, edited by P.C. Thurston, Owen L. White, R.B. Barlow, M.E. Cherry, and A.C. Colvine, Ontario Geological Survey, Miscellaneous Paper 132, 435p.
- Hanneson, J. E., and Huxter, R. S. 1987. The Detection and Mapping of Basement Conductors Under Areas Covered by Thick Huronian Sedimentary Rocks, District of Timiskaming; p.406-410, in Summary of Field Work and Other Activities 1987, by the Ontario Geological Survey, edited by R.B. Barlow, M.E. Cherry, A.C. Colvine, Burkhard Dressler, and Owen L. White, Ontario Geological Survey, Miscellaneous Paper 137, 429 p.
- Hanneson, J. E., and Huxter, R. S. 1988. The Detection and Mapping of Basement Conductors Under Areas Covered by Thick Huronian Sedimentary Rocks, District of Timiskaming; p 464-469, in Summary of Field Work and Other Activities 1988, by the Ontario Geological Survey, edited by A.C. Colvine, M.E. Cherry, Burkhard O. Dressler, P.C. Thurston, C.L. Baker, R.B. Barlow, and Chris Riddle, Ontario Geological Survey, Miscellaneous Paper 141, 498p.
- Hanneson, J. E., and Huxter, R. S. 1989. UTEM Profile Data (1987), Cobalt Geophysical Research Project, Cobalt Area, District of Timiskaming, Ontario; Ontario Geological Survey, Map P.3133, Geophysical Series - Preliminary Map, scale 1:20 000.
- Hanneson, J.E., Huxter, R.S. and Rowe, D.S. 1989. UTEM profile data (1988) Cobalt Geophysical Research Project, Cobalt area, District of Timiskaming, Ontario; Ontario Geological Survey, Preliminary Map P.3141, Geophysical Series, scale 1:20 000.
- Hanneson, J.E., and Huxter, R.S. 1991. Ground geophysical survey and computer modelling, Cobalt geophysical research project, Cobalt area, Ontario Geological Survey, Map 80802.
- McGuiunty, B., Gignac, J., and Rhul, M. 2021. Report on a Diamond Drilling and Sampling Program 2019 Nipissing Cobalt and South Abitibi Properties, Cobalt and Latchford, Ontario Larder Lake and Sudbury Mining Divisions; Assessment File 20000019478

STATEMENT OF QUALIFICATIONS

I, **Zachary Matheson**, of 104 Ordnance St, Toronto, ON, do hereby certify that:

1. I am employed as project geologist by NewOrigin Gold Corp.
2. I graduated with a Bachelor of Science in Geology (BSc. Geology) from Saint Mary's University in 2016.
3. I have worked as a geologist for more than 3 years.
4. I am responsible for the technical report titled "Reprocessing & Analysis of VTEM EM & Magnetic Surveys, Nipissing Cobalt, Ontario".
5. My knowledge of the property as described herein was obtained by literature review.
6. I have no direct interest, nor do I expect to receive any interest in the mining claims that comprise the Nipissing Cobalt Property.
7. I am not aware of any material fact or material change with respect to the subject matter of the Technical Report that is not reflected in the Technical Report, the omission to disclose which makes the Technical Report misleading.
8. I consent to the filing of this Technical Report with any pertinent organization if deemed necessary such as any stock exchange and other regulatory authority and inclusive of any publication by same for regulatory purposes, including electronic publication in the public company files on their websites accessible by the public, of this Technical Report.
9. Dated this 25th day of March, 2022.

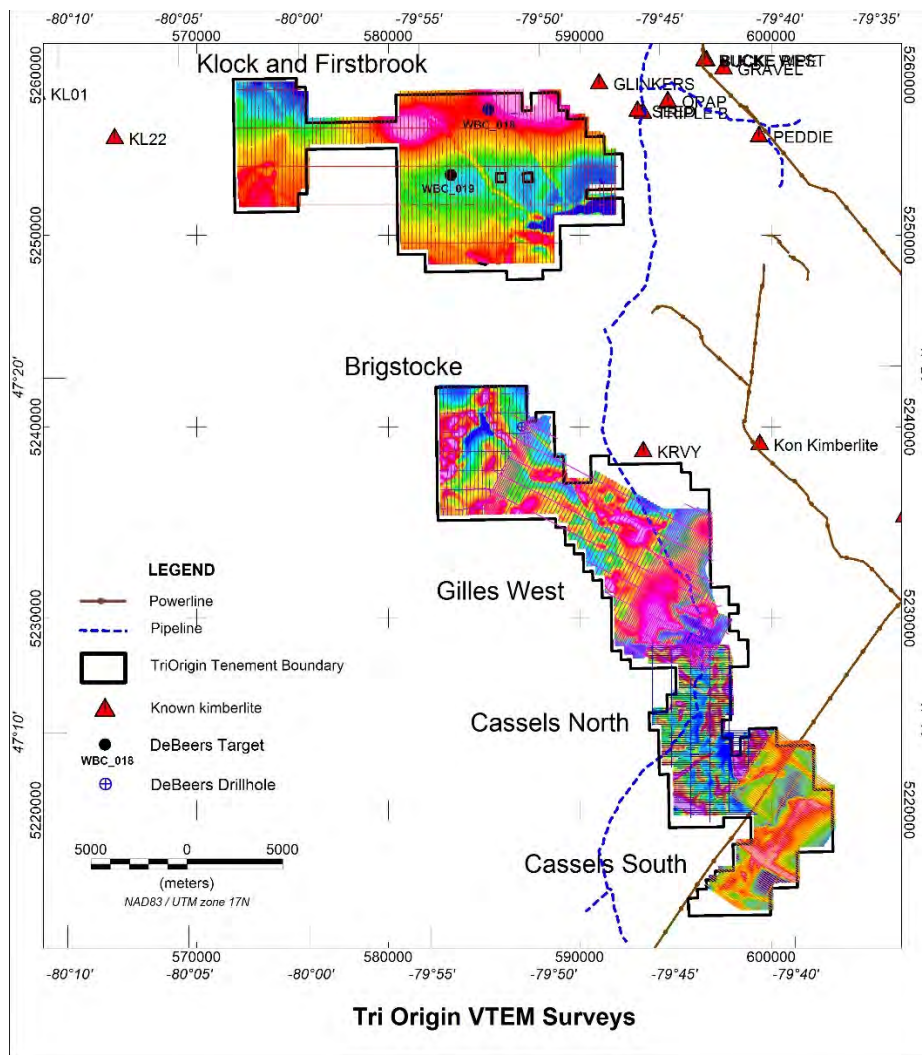
Zachary D. Matheson, BSc

APPENDIX A

**“Report on Processing and Analysis of Five VTEM EM and Magnetic Surveys, Nipissing
Cobalt and South Abitibi Properties, Ontario”**



**REPORT ON PROCESSING AND ANALYSIS
OF FIVE VTEM EM AND MAGNETIC SURVEYS
NIPISSING COBALT AND SOUTH ABITIBI PROPERTIES
ONTARIO
FOR
TRI ORIGIN EXPLORATION LTD.
APRIL 2021**





**REPORT ON PROCESSING AND ANALYSIS
OF FIVE VTEM EM AND MAGNETIC SURVEYS**

**NIPISSING COBALT AND SOUTH ABITIBI PROPERTIES
ONTARIO**

FOR

TRI ORIGIN EXPLORATION LTD.

APRIL 2021

CONTENTS

- 1. SUMMARY 2
- 2. INTRODUCTION 3
- 3. SCOPE OF WORK 5
 - 3.1 Processing 5
 - 3.2 Target Model 5
- 4. VTEM PROCESSING AND ANALYSIS TECHNIQUES 8
 - 4.1 Magnetics Processing 8
 - 4.1.1 Keating Analysis 8
 - 4.1.2 MAG3D Voxel Inversion 8
 - 4.2 Electromagnetic Processing 8
 - 4.2.1 Time-Domain Layered-Earth Conductivity Model 8
 - 4.2.2 Time Constant 9
 - 4.2.3 MultiPlots™ 10
 - 4.2.4 Keating Analysis of the EM Data 11
- 5. KEATING MAGNETIC PROCESSING 13
- 6. KEATING EM PROCESSING 27
- 7. MAG AND EM SOLUTIONS COMBINED 40
- 8. DISCUSSION 45
- 9. PRODUCTS 46
- 10. CONCLUSIONS AND RECOMMENDATIONS 47
- 11. REFERENCES 48
- APPENDIX A: KEATING 1995 PAPER 49
- APPENDIX B: CONDOR TECHNICAL NOTE 2004-1 50
- APPENDIX C: MAG3D INVERSION NOTES/EM REFERENCE PAPERS 51
- APPENDIX D: QUALIFICATIONS 54
 - Statement of Qualifications – Ken E. Witherly 54

1. SUMMARY

This report covers the processing and analysis completed by Condor Consulting, Inc. (Condor) of five VTEM surveys performed during 2015-2016 by Geotech Ltd. for Tri Origin Exploration Limited (Tri Origin).

Condor was commissioned to carry out basic processing and analysis of the EM and magnetic data from the VTEM surveys.

The principal focus of the present work was to run Keating Analysis (Keating, 1995) on both magnetic and EM data, to delineate possible diamondiferous kimberlite pipes.

Layered Earth Inversion (LEI) was performed on the EM data to produce a 1D conductivity depth section for every line.

MAG3D inversion of the magnetic data was carried out to produce a 3D voxel apparent susceptibility model,

MultiPlots™ to show the results of the above analysis, together with the basic acquired magnetic and EM data, were generated for every line.

No formal interpretation or target generation was carried out on the VTEM data.

The client also expressed interest in reviewing and comparing magnetic and EM data acquired by RJK Explorations Ltd. (RJK) during their diamond exploration around the Kon area and in their Nipissing Diamond Project south of Cobalt, Ontario. This has been done and included as an appendix to this report.

2. INTRODUCTION

During the period October 2015-January 2016, Geotech Ltd. (Geotech) carried out four contiguous VTEM airborne electromagnetic and magnetic survey for Tri Origin over the Brigstocke, Gilles West, Cassels North, and Cassels South blocks (Figure 1). Shortly afterwards, in January-February 2016, Geotech flew the Klock and Firstbrook block, also shown in Figure 1. The logistics reports for these surveys are Venter et al., 2016, and Fiset et al., 2016, respectively.

The flight line direction and flight line spacing varied from block to block, as listed in Table 1.

Table 1: VTEM blocks specifications

Survey Block	Line Spacing (m)	Flight Direction	Line Km
Brigstocke	100 and 200	N 0° E / N 180° E	156
Gilles West	100 and 200	N 27° E / N 207° E	594
Cassels North	100	N 90° E / N 270° E	391
Cassels South	100	N 124° E / N 304° E	376
Klock and Firstbrook	200	N 0° E / N 180° E	658

The current processing and analysis included all lines from the five blocks.

The locations of known kimberlites contained in the Ontario Ministry of Energy, Northern Development and Mines Mineral Deposit Inventory database are shown in Figure 1. https://www.geologyontario.mndm.gov.on.ca/MDI_Description.html Kimberlite KL22 lies west of the Klock and Firstbrook area.

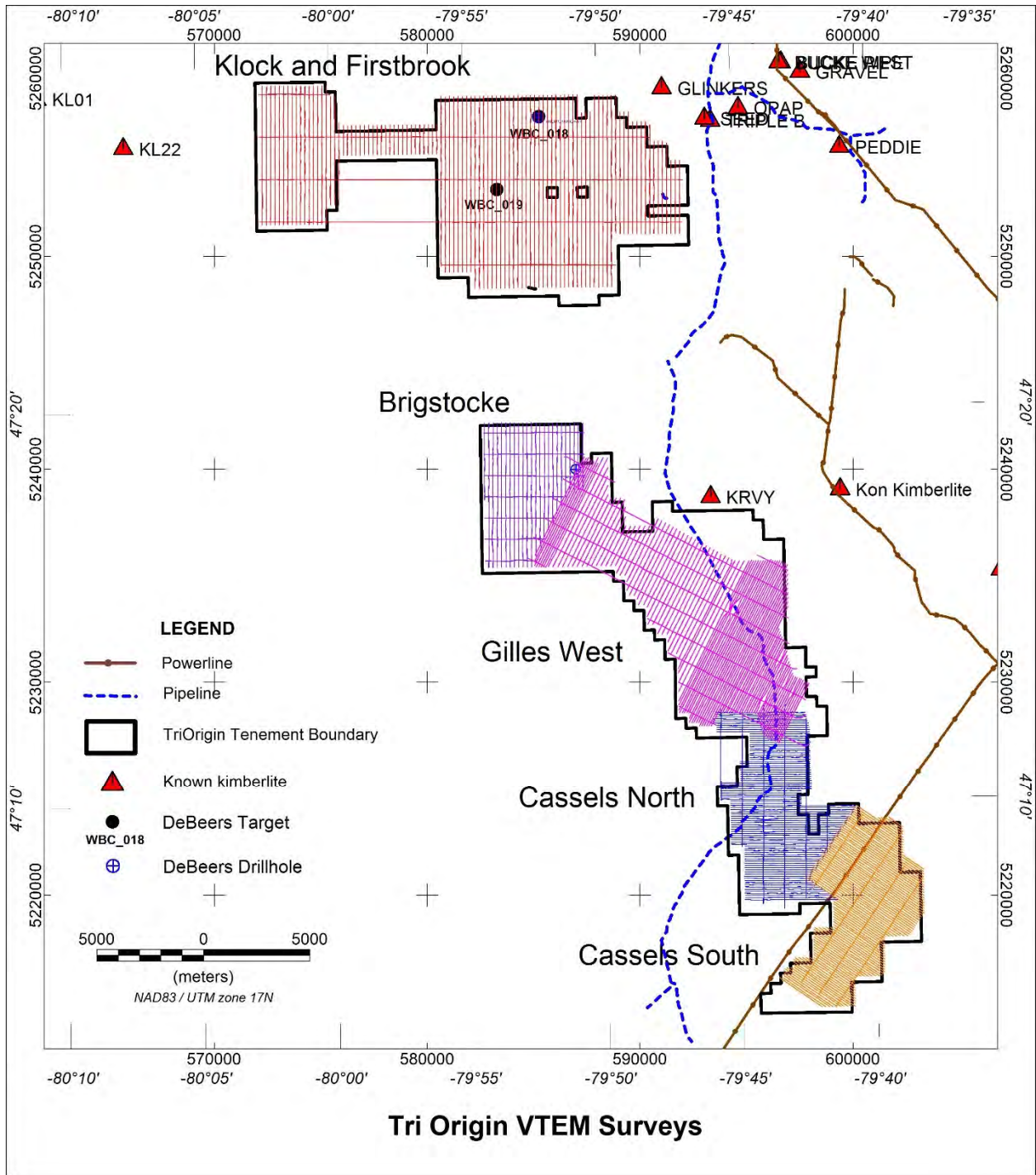


Figure 1: Location map of Tri Origin VTEM surveys

3. SCOPE OF WORK

3.1 Processing

The client requested Condor carry out the following work:

1. Run Keating kimberlite pipe analysis on the magnetic data for all five areas.
2. Explore the feasibility of running a Keating technique on the EM data
3. Run LEI 1D inversion (layered earth conductivity modelling) on the VTEM EM data to produce a conductivity depth section for all lines in all five blocks.
4. Run MAG3D inversions on the magnetic data for all five blocks and produce a voxel apparent susceptibility 3D volume for each survey.
5. Generate MultiPlots™ for all lines, incorporating the data produced in steps (1) to (4) above.

NOTE: No formal interpretation or target definition has been carried out.

The client also expressed interest in reviewing and comparing magnetic and EM data acquired by RJK during their diamond exploration around the Kon area and in their Nipissing Diamond Project south of Cobalt, Ontario. This has been done and included as an appendix to this report.

3.2 Target Model

Traditionally, magnetic methods have been the primary means to detect kimberlites. However, when the host rocks are competent (crystalline), then gravity and EM/DC resistivity techniques can be applied as well due to the strong physical property contrasts. Figure 2 shows the range of physical properties that can be observed. In Figure 3, a suite of four examples of the magnetic responses associated with kimberlites. In Figure 4, the results of and AeroTEM II time-domain EM survey over the Lapointe kimberlite are shown (Rudd 2005). The kimberlite has a clear positive magnetic response and moderate EM response.

In terms of applying the Keating filter to magnetic and EM data, Figure 5 shows the results from the central part of the Diavik kimberlite field. While there are a number of false positives, the majority of the known kimberlites are detected with both the Keating magnetic and EM filters.

The kimberlites are not expected to be strong conductors, so it is recommended that strong conductors defined by the time constant (described in Section 4) should be downgraded.

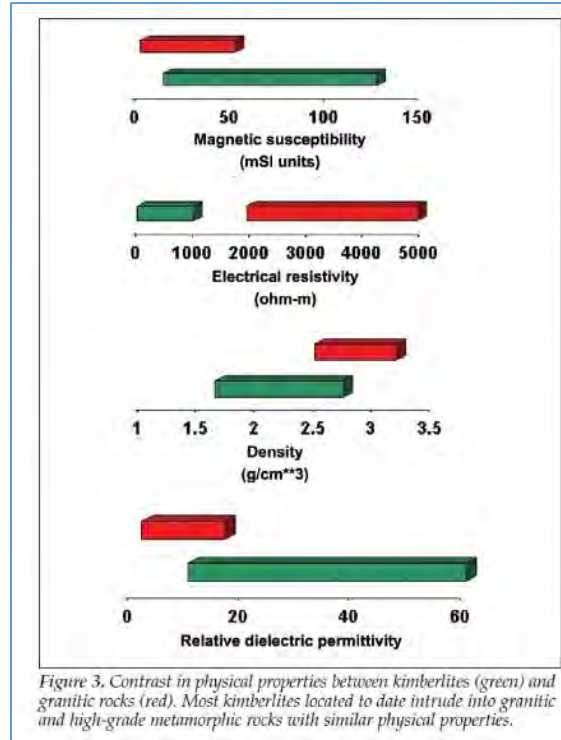


Figure 2: Typical physical property values for kimberlites (green) and crystalline host (red). (Power et al., 2004).

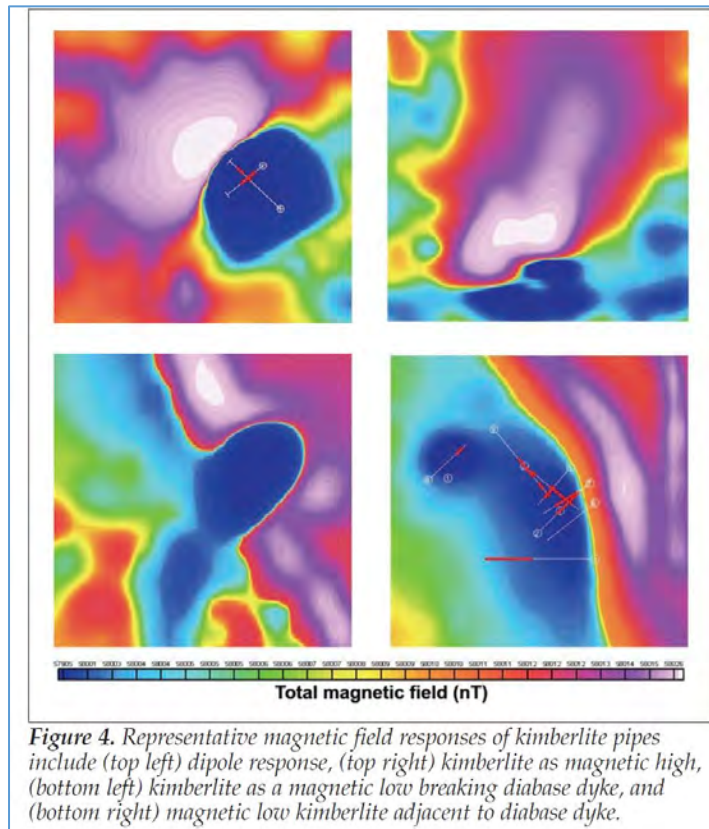


Figure 3: Examples of magnetic response of kimberlites (Power et al., 2004).

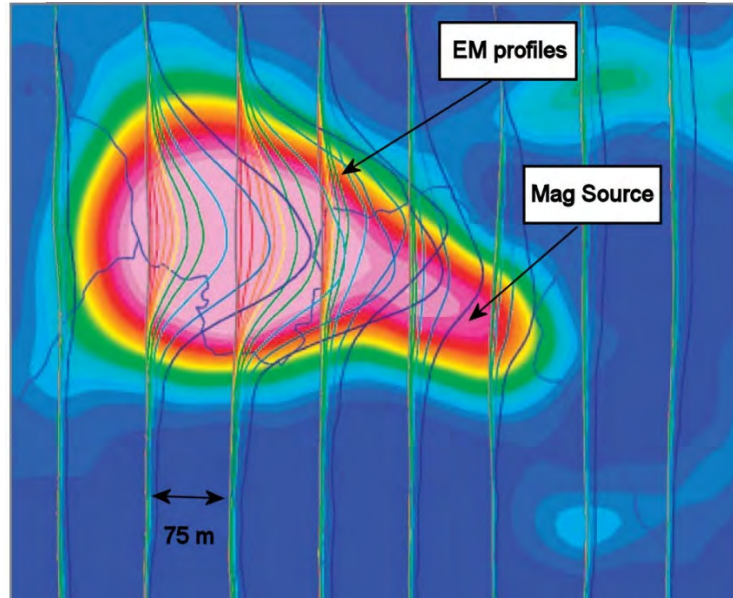


Figure 4: Geophysical response of Lapointe kimberlite; colored body-mag; profiles EM. (Rudd 2005).

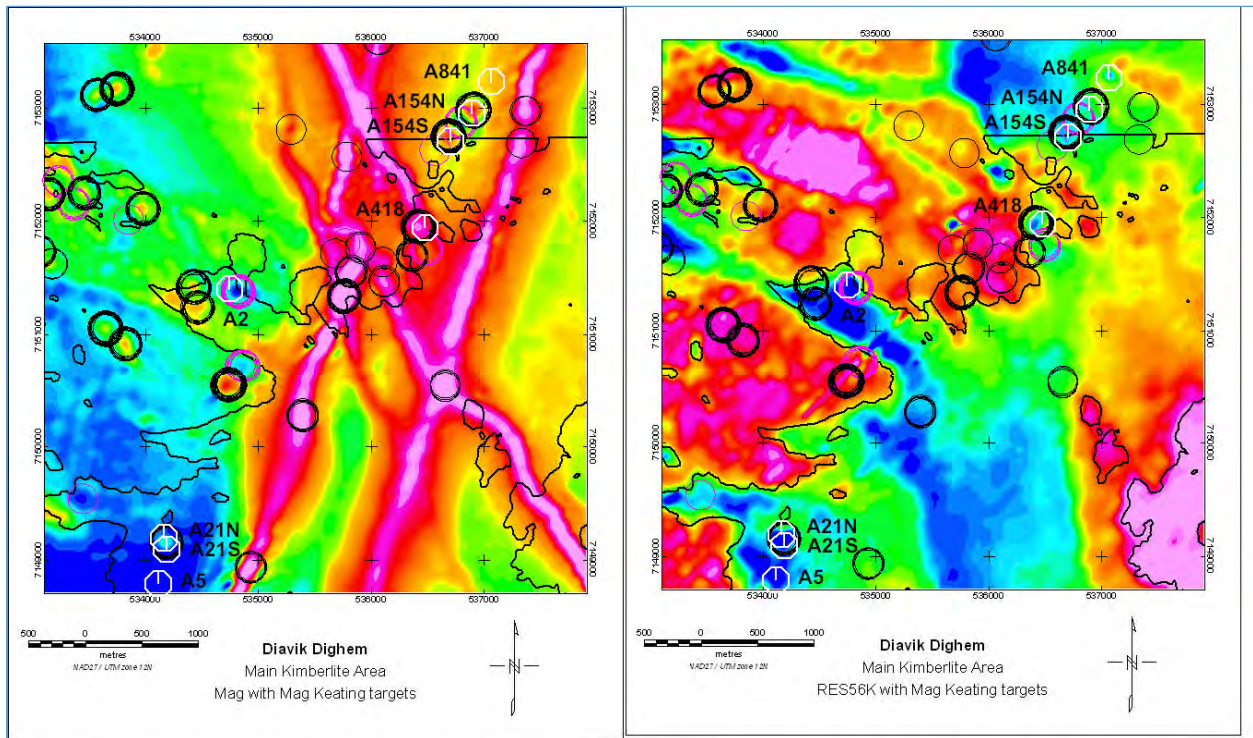


Figure 5: Diavik area (left) Keating applied to magnetic data; (right) Keating applied to EM data.

4. VTEM PROCESSING AND ANALYSIS TECHNIQUES

4.1 Magnetism Processing

The reduction to pole (RTP) transformation was performed on the gridded total magnetic intensity data, using the Discover PA¹ software package. This product represents a calculation of what the magnetic observations would be if the inducing field were vertical (i.e. observations made at the magnetic pole), minimizing the side lobes of anomalies due to the dipole nature of the magnetic charges.

In addition, the first vertical derivative of the RTP was calculated and used in display of the Keating magnetic solutions.

4.1.1 Keating Analysis

Keating analysis is a pattern recognition technique to match theoretical anomalies of circular pipe-like models to the acquired magnetic data. The same pattern recognition technique can also be utilized for the EM channels and/or conductivity data. Details of the Keating analyses used in this project are documented in later sections of this report.

4.1.2 MAG3D Voxel Inversion

Details of the MAG3D voxel inversion are contained in Appendix C.

4.2 Electromagnetic Processing

To enhance the data and to assist interpretation, the following processing steps were carried out on the VTEM Z-component of the measured dB/dt EM data:

- Layered earth conductivity modeling
- Time constant

4.2.1 Time-Domain Layered-Earth Conductivity Model

The depth of conductors is determined from the Layered-Earth Inversion Models (LEI). This style of modeling works well where the conductivity structure of the earth is primarily sub-

¹ Discover PA is a product of Datamine

horizontal ($\leq 30^\circ$). However, if the conductors are steeply dipping sheets or pods, the depth derived from the LEI can be used only as a rough indicator of the actual depth; in general, the depth of steeply dipping conductors is over-estimated by the LEI program. Parametric modeling using a program such as Maxwell² is required to properly characterize steeply dipping bodies.

The LEI produces a conductivity-depth profile for each individual sounding. The units of conductivity are Siemens per meter, often converted for convenience to milliSiemens per meter (mS/m). The reference model used in the modeling process is what the LEI program produces for deep layers that are beyond the sensitivity of the data. It is also used in the objective function, which evaluates the complexity of the model. Often the reciprocal of the conductivity is computed to form resistivity, which has the units of ohm-m.

The LEI algorithm models the EM data (Farquharson and Oldenburg 1993, Ellis 1998-Appendix C), with a 28-layered earth model that increases layer thickness from the surface to depth in an approximately logarithmic fashion. The first layer is 5 m thick while the deepest is 232 m thick (a complete list of layers is provided in Appendix C). A starting model of 1 000 ohm-m (0.001 S/m) was used, with a reference model of 10 000 ohm-m (0.0001 S/m). The modeling program defaults to the reference model at depth where there is not enough information to refine the earth model. The results of the modeling are presented in the form of a conductivity depth section (CDS).

4.2.2 Time Constant

For time-domain systems such as VTEM, the *AdTau* algorithm calculates the time constant (often denoted by the Greek letter tau) from time-domain decay data. The program is termed *AdTau* because rather than using a fixed suite of time channels as commonly done, the user sets a noise level and depending on the local characteristics of the data, the program will select the set of five channels earlier in time to avoid the channels containing data below the noise level. In resistive areas, earlier channels will tend to be used due to rapid decay of the transient signal, whereas in conductive terrains the latest channels available

² Maxwell is a product of EMIT, Perth, Australia

can generally be used. A typical decay fit; in this case the last five channels, are shown to the right in Figure 6.

For additional general information on the time constant see:

http://en.wikipedia.org/wiki/Time_constant.

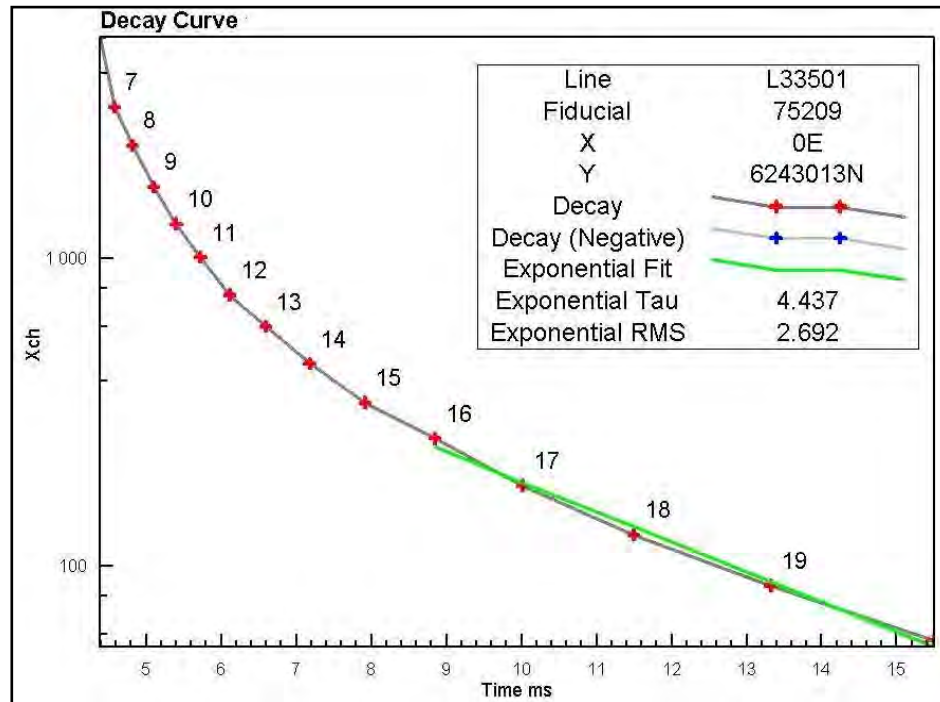


Figure 6: Typical decay curve for time-domain EM systems.

4.2.3 MultiPlots™

Figure 7 shows an example of a MultiPlot™ used to display the results of the LEI, AdTau time constants, MAG3D magnetic susceptibility voxel inversion and the Keating magnetic and EM analyses, in addition to the acquired EM data profiles. A description of the components follows:

MiniMaps:

- Image of TMI RTP, showing flight line.
- Image of TMI RTP 1VD (First vertical derivative), showing flight line.
- Image of EM channel $dB/dt[6]$, showing flight line
- Bing satellite image, showing Keating magnetic solutions, plus flight line.

Tracks:

- EM Z dB/dt (43 channels)
- EM X dB/dt (27 channels)
- AdTau time constant Z dB/dt (red), AdTau time constant Z B-Field (blue), Power Line Monitor (green)
- LEI Conductivity Depth Section (dB/dt) showing EM System Height
- Total Magnetic Intensity TMI (Blue) and TMI 1VD (1st vertical derivative) (red)
- Magnetic Susceptibility Depth Section along flight line from MAG3D inversion
- TrackMap of RTP 1VD magnetic image, with flight path and Keating magnetic solutions overlain (black-positive, white-negative)
- TrackMap of dB/dt EM channel SFz[6] image with flight path and Keating EM solutions (black)

4.2.4 Keating Analysis of the EM Data

Details of this processing are contained in a later section of this report.

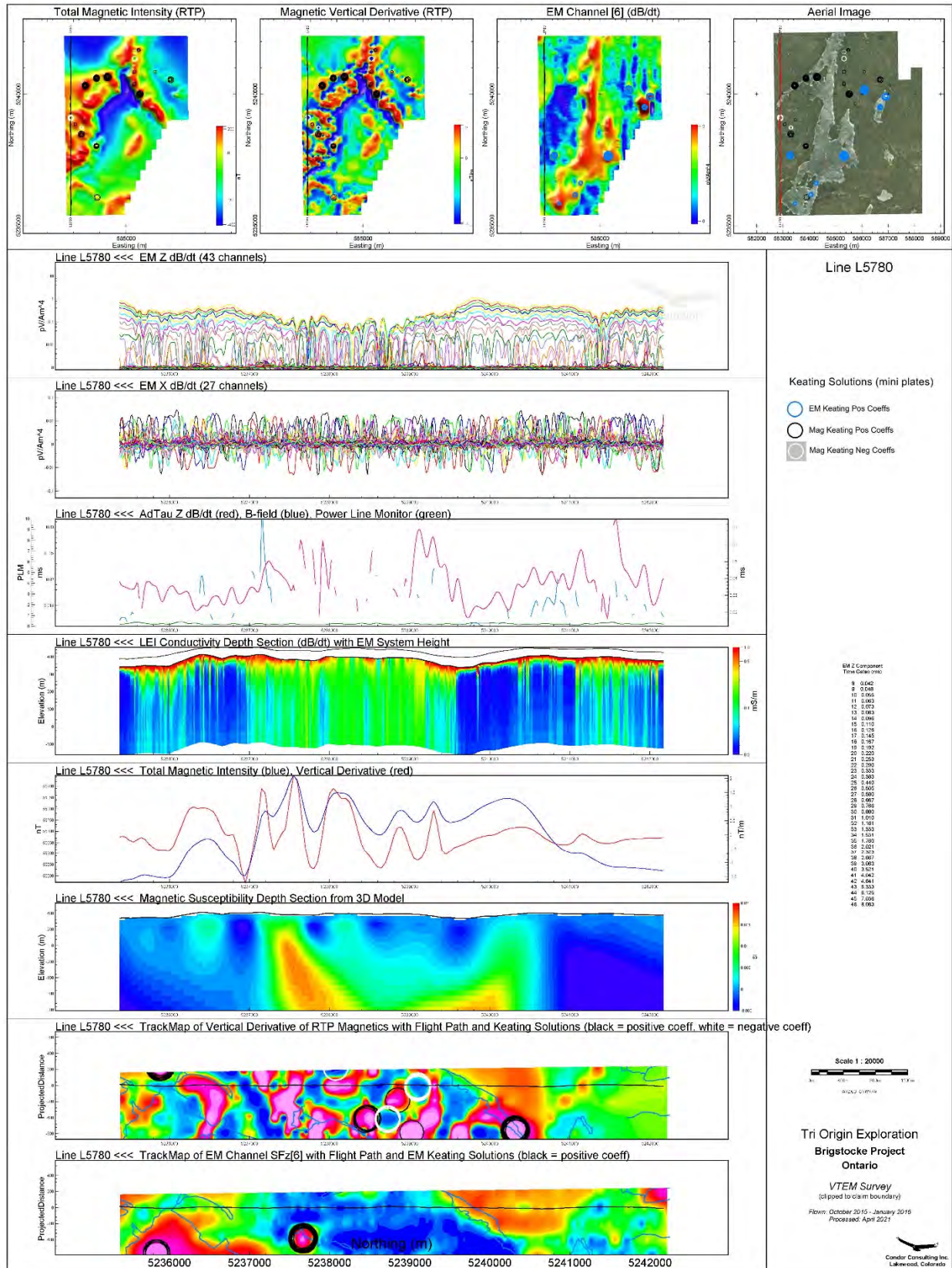


Figure 7: Typical MultiPlot.

5. KEATING MAGNETIC PROCESSING

This technique was developed as a simple means to identify circular features in magnetic data (Keating 1995). The method utilizes a simple pattern recognition technique to locate magnetic anomalies that resemble the response of a modeled pipe. The magnetic response of a vertically dipping cylinder is computed in grid form. The modeled parameters that may be adjusted include the depth, radius and length of the cylinder, the local magnetic inclination and declination, and the areal extent of the anomaly. The model grid is then passed over a grid of total magnetic intensity as a “moving window”. The correlation between the modeled and observed data is computed at each grid node using a first order regression and archived. The correlation coefficients that exceed a specific threshold (e.g. 85%) are retained for further analysis. Negative correlation coefficients are retained but are categorized as being caused by reversely magnetized bodies.

Keating’s 1995 paper is included in Appendix A.

For the current study, four target radii were used for the magnetic analysis: 25, 50, 75 and 100 m. Three depths to top of the pipe were modeled, 0, 30 and 60 m below ground level (or 60, 90 and 120 m below the nominal VTEM magnetic sensor clearance of 60 m).

The Keating matched filtering is applied within the Oasis Montaj environment.

For the current study, the VTEM magnetic RTP grid and the modeled response of a vertical cylinder in a vertical inducing field were used for the Keating analysis. In both cases the grid mesh size was 25 m for all five blocks.

As listed in Table 1, the flight line spacing in the five blocks varies from 100-200 m. Figure 8 shows magnetic profiles across kimberlite pipe models calculated using ModelVision³. Four models are shown (corresponding to the Keating models). The upper two show pipes with the top at zero depth and radii of 25 and 100 m respectively. The lower two show pipes with the top at depth 60 m below surface and radii of 25 and 100 m respectively. It can be seen that the narrowest anomaly (25 m radius, zero depth) in the top left would be defined reasonably well at a line spacing of 100 m, but would not be reliably defined at a line spacing of 200 m (unless a flight line was located close to the center of the pipe). Even the widest anomaly (created from the pipe with the 100 m radius and depth

³ ModelVision is a product of Tensor Research, Australia

60 m), would be barely defined by 200 m line spacing (if the flight lines happen to straddle the pipe). Consequently, the Keating analysis in areas of 200 m line spacing (including the whole of the Klock and Firstbrook block) should be treated with caution; kimberlite pipes between flight lines may not generate recognizable anomalies.

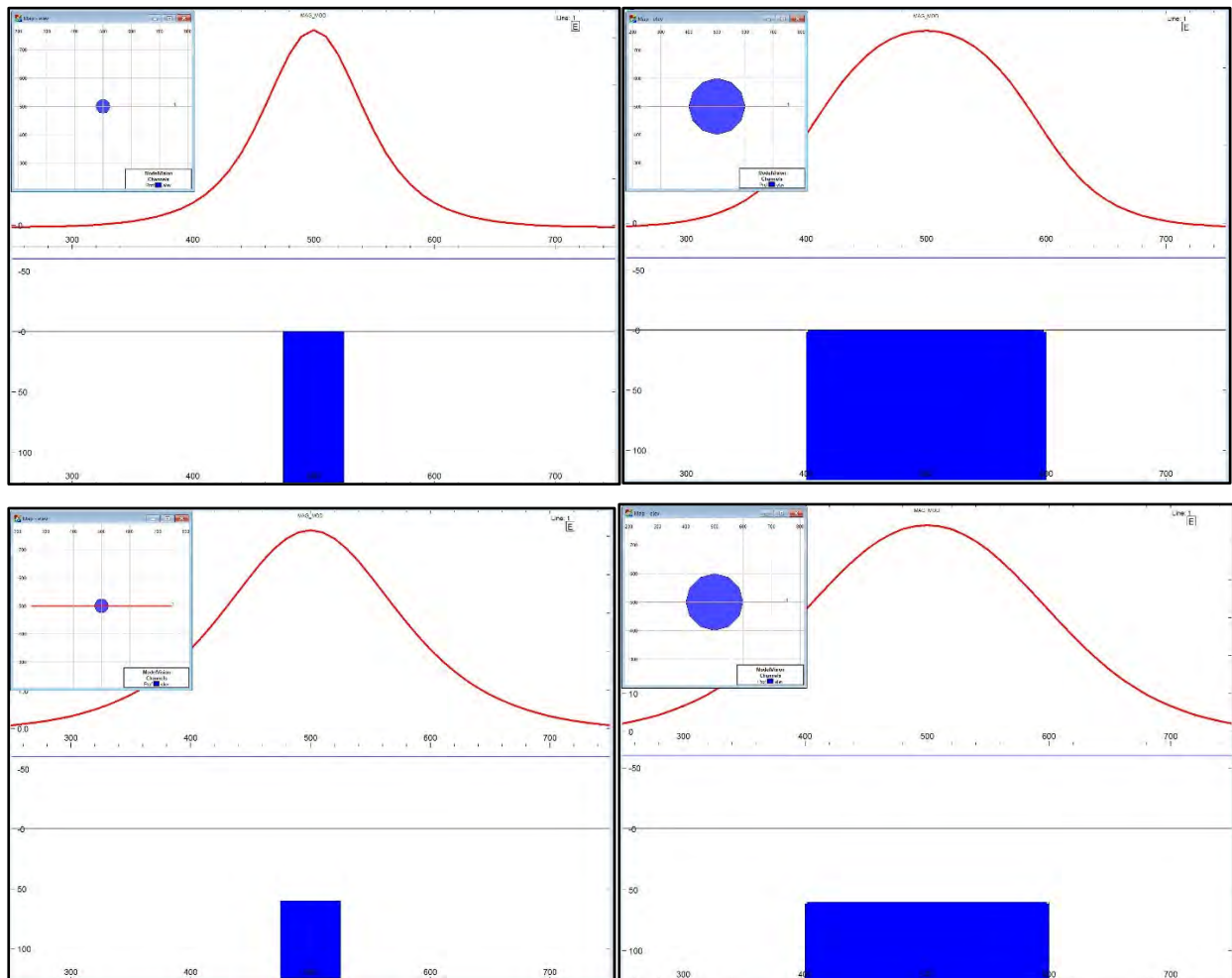


Figure 8: Calculated magnetic anomalies from kimberlite pipe models.
 Top left: Radius 25 m, Depth 0m. Top right: Radius 100 m, Depth 0m.
 Bottom left: Radius 25 m. Depth 60 m below surface. Bottom right: Radius 100 m, Depth 60 m.

The Keating matched filtering generates an output file with X, Y locations of matching anomalies, together with information on the correlation coefficients. These data are inspected and a suitable threshold value for the correlation coefficient is selected, so as to sift out anomalies that do not fit well to the theoretical model and thus reduce the data set to a manageable number of targets.

For this study, a threshold correlation coefficient of 85% was used, together with a threshold amplitude of 50.

The thresholded anomaly locations are then overlain on a suitable base map – in this case the RTP magnetics and RTP 1VD. The latter highlights smaller, local anomalies typical of kimberlite pipes.

The Keating magnetic solutions for the five blocks are shown in Figures 9-20.

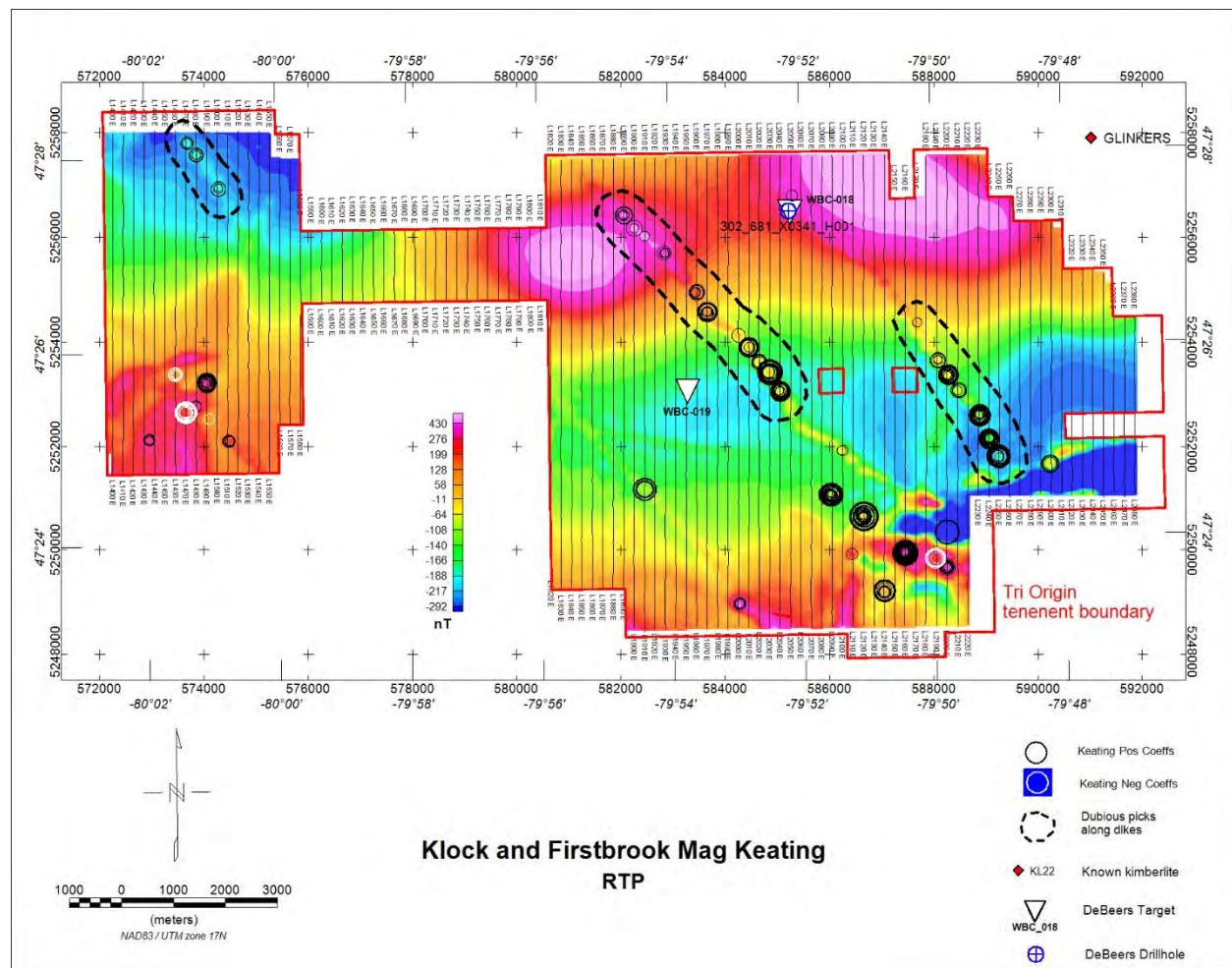


Figure 9: Klock and Firstbrook: Keating Magnetic solutions superimposed on RTP image. The size of the symbols is proportional to the correlation coefficient. Only solutions with a Correlation Coefficient above 85% are shown.

The positive correlations are shown as black circles and the negative correlations (possibly caused by reversely magnetized pipes) as white circles. The size of the symbols is proportional

to the correlation coefficient. In many cases, several solutions occur close to one another (even after thresholding), so that the circles overlap and appear to be “thicker” than single solutions.

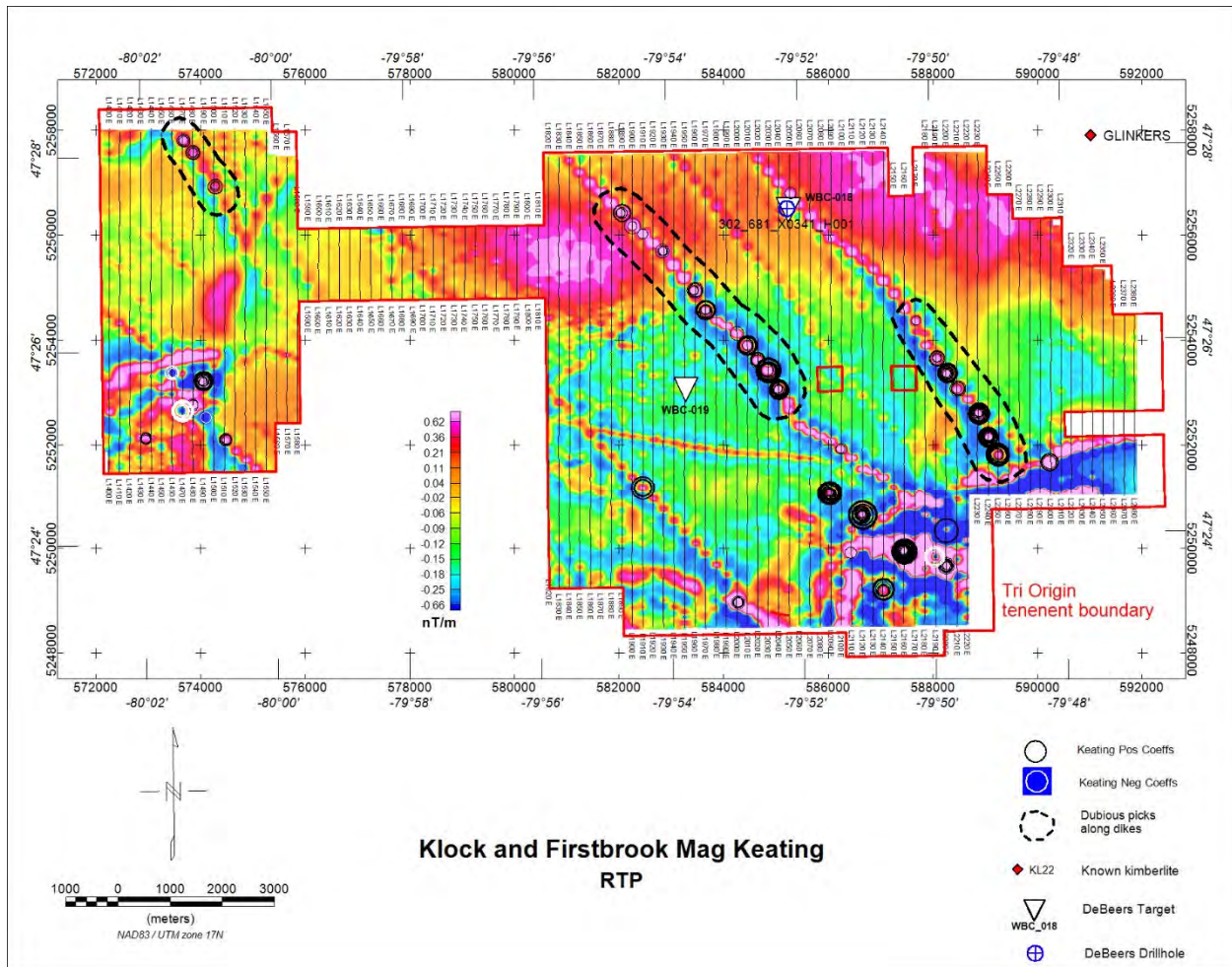


Figure 10: Klock and Firstbrook: Keating Magnetic solutions superimposed on RTP 1VD image. The size of the symbols is proportional to the correlation coefficient. Only solutions with a Correlation Coefficient above 85% are shown.

In the Klock and Firstbrook area (Figures 9 and 10), a number of solutions have been defined by a polygon and labeled as “Dubious picks along dikes”. The standard Minimum Curvature gridding method utilized to grid the data results in a “string of pearls” effect along dike-like features which strike at less than approximately 60 degrees to the flight lines. Many of the interpreted dikes in this area strike at 45 degrees or less to the flight lines and this has resulted in many magnetic “pearls”. These have shapes and dimensions similar to the anomalies produced by kimberlites and so often generate Keating solutions. It is possible that a few of these Keating solutions could

be generated by kimberlites intruded along the dikes, but not feasible to differentiate these from the many other solutions.

In past exploration, De Beers defined two “targets” within the Klock and Firstbrook area and drilled one of them. The locations are shown on the left of Figure 11. The targets are shown as inverted white triangles and the drill hole into the northern target is shown as a blue circle with a cross inside. On the right, these symbols have been omitted so that the underlying RTP 1VD magnetic image can be seen. The targets correlate with very small, weak magnetic anomalies which did not generate any Keating solutions. There is a solution along the dike adjacent to the northern target, but this appears to be quite separate from the weak anomaly correlating with the target itself.

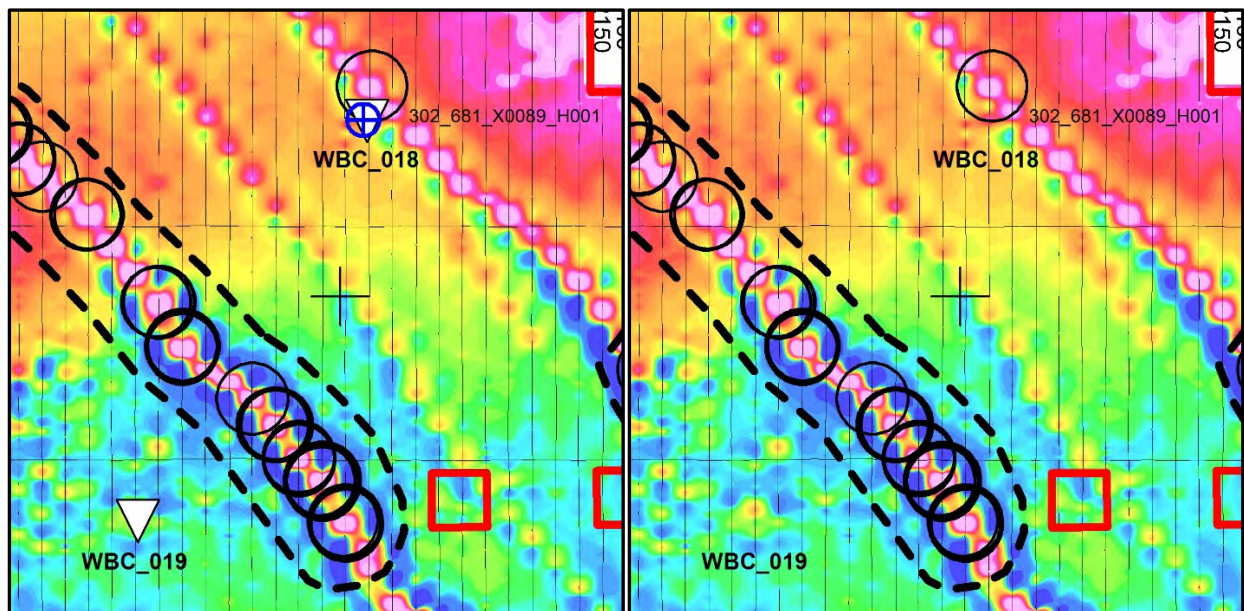


Figure 11: Area of De Beers targets and drill hole (RTP 1VD image)
Left: Targets shown as inverted white triangles. Drill hole shown as blue circle with cross.
Right: Symbols removed to allow underlying magnetic image to be seen.

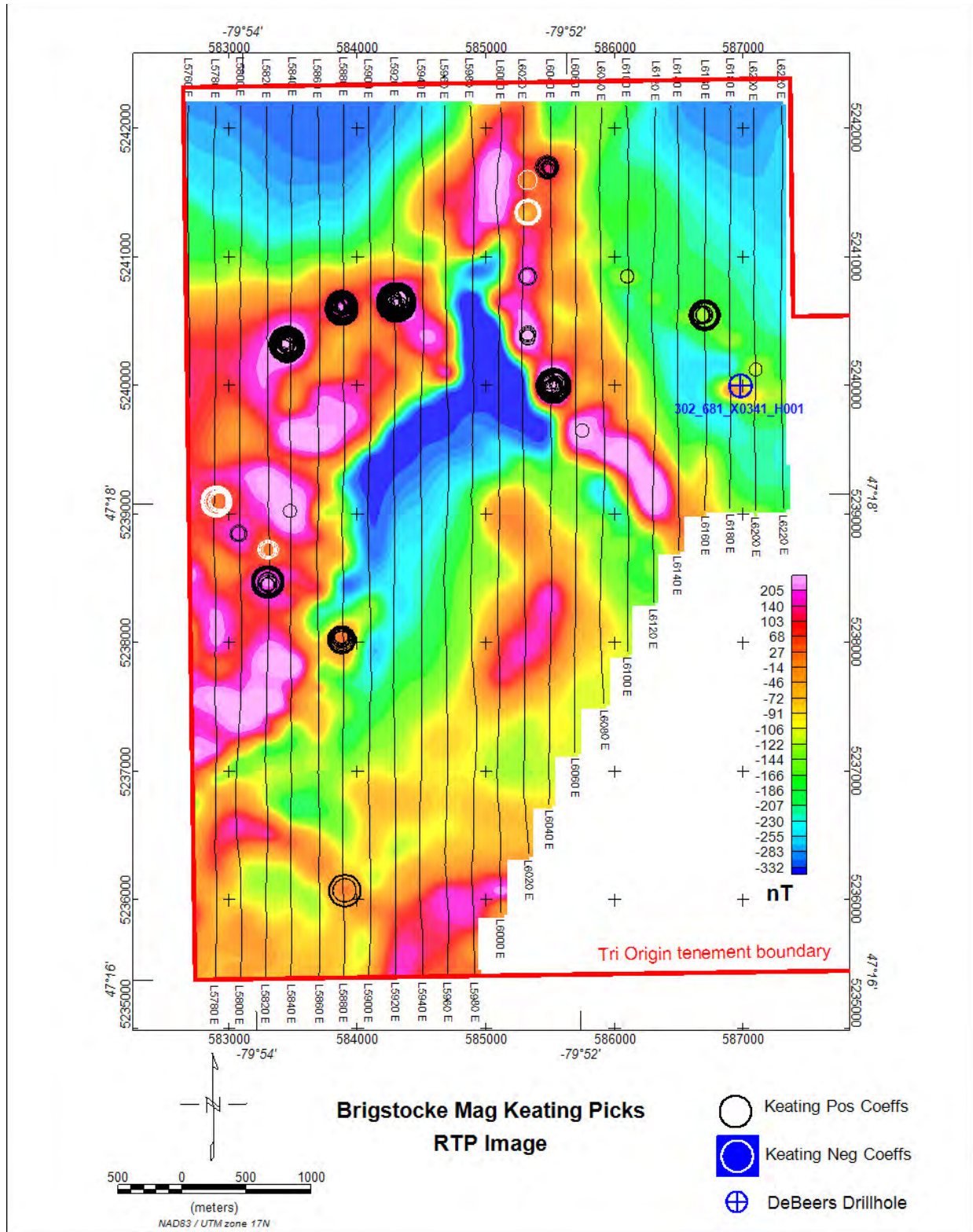


Figure 12: Brigstocke: Keating Magnetic solutions superimposed on RTP.

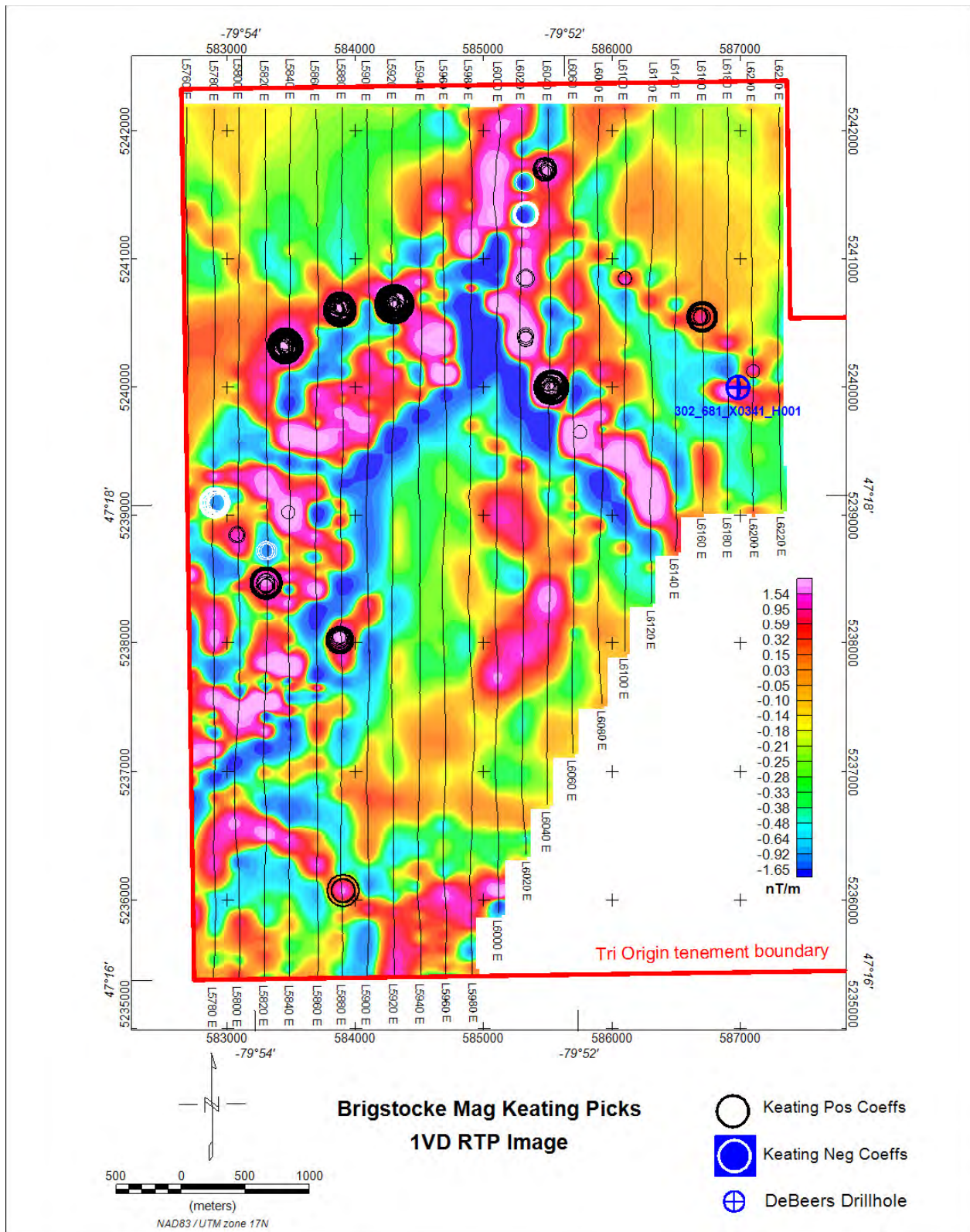


Figure 13: Brigstocke: Keating Magnetic solutions superimposed on RTP 1VD.

De Beers second drill hole is located in the far northeast of the Brigstocke area. Figure 14 shows the enlarged RTP 1VD image in the vicinity of the drill hole. It correlates with a smallish magnetic anomaly, elongated in an east-west direction. This did not generate a Keating magnetic solution, probably because the elongate anomaly does not fit the theoretical sub-circular shape.

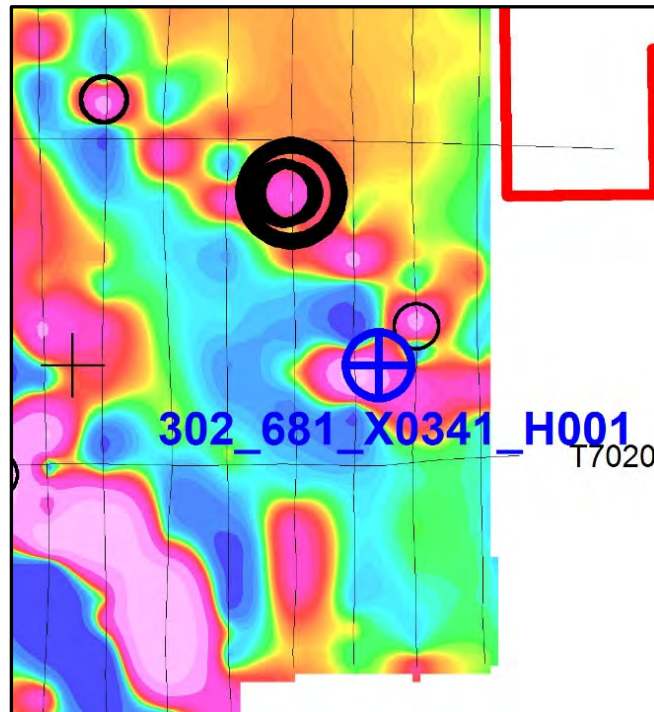


Figure 14: Brigstocke- Area of De Beers drill hole. (RTP 1VD image).

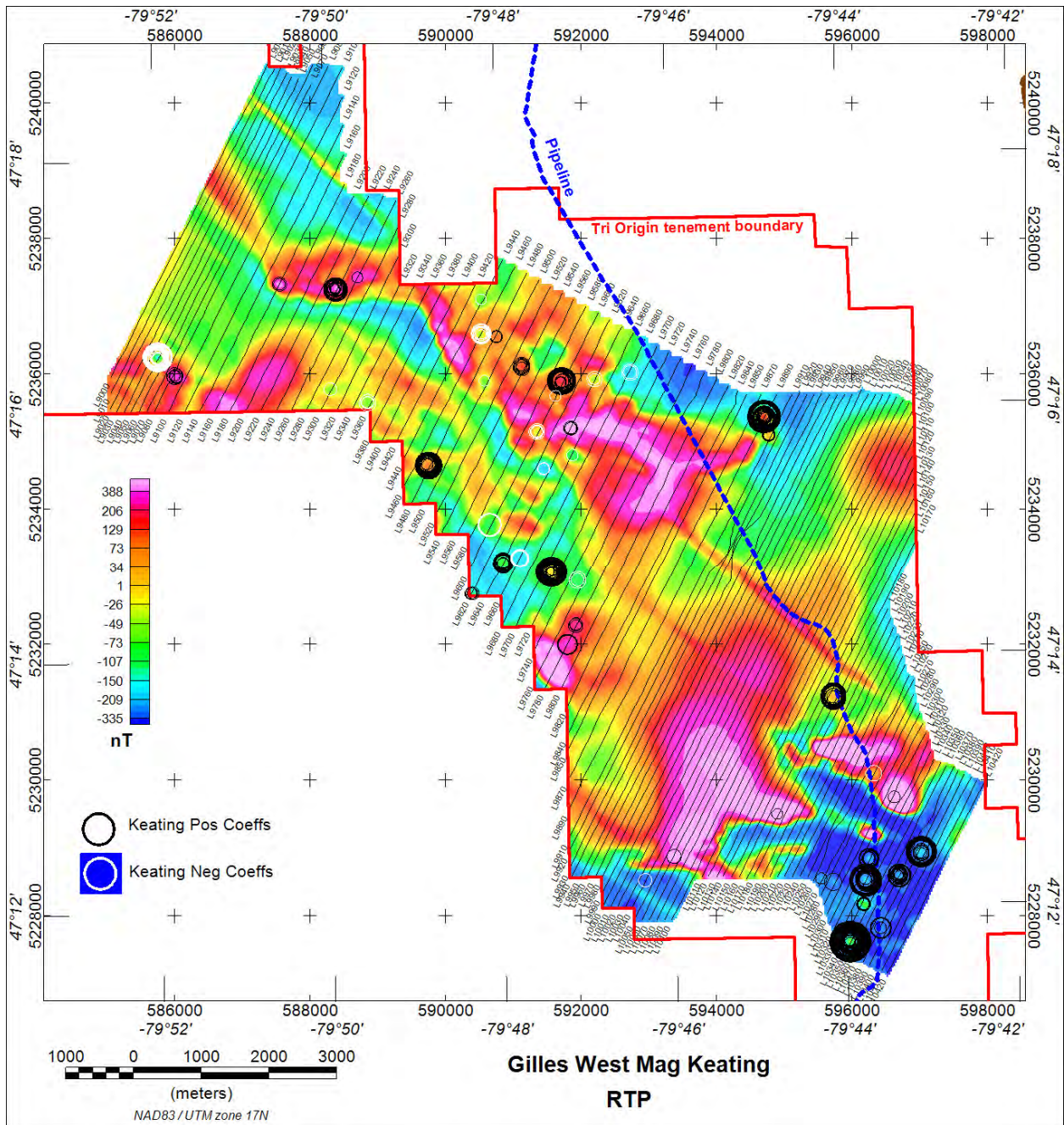


Figure 15: Gilles West: Keating Magnetic solutions superimposed on RTP.

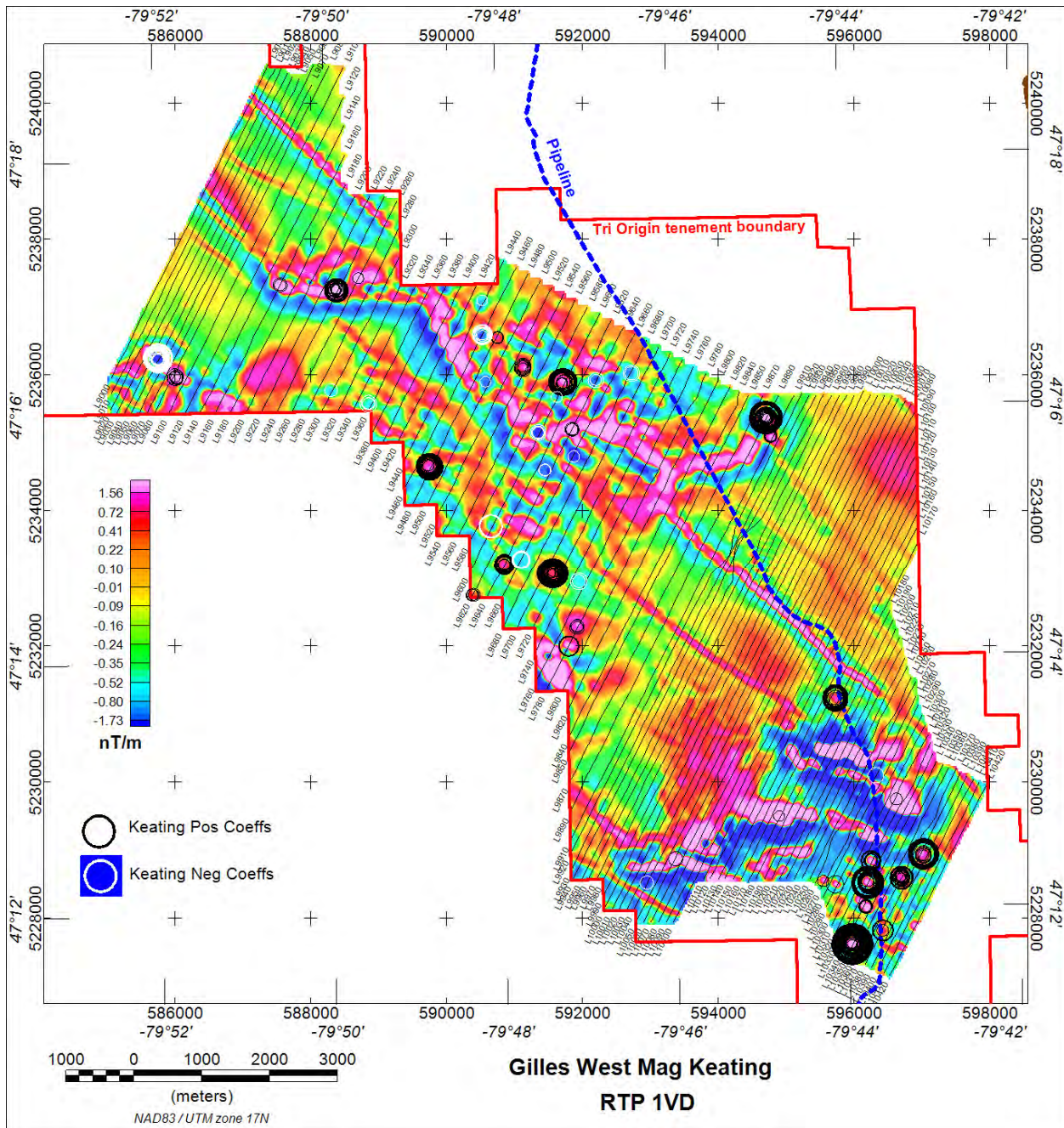


Figure 16: Gilles West: Keating Magnetic solutions superimposed on RTP 1VD.

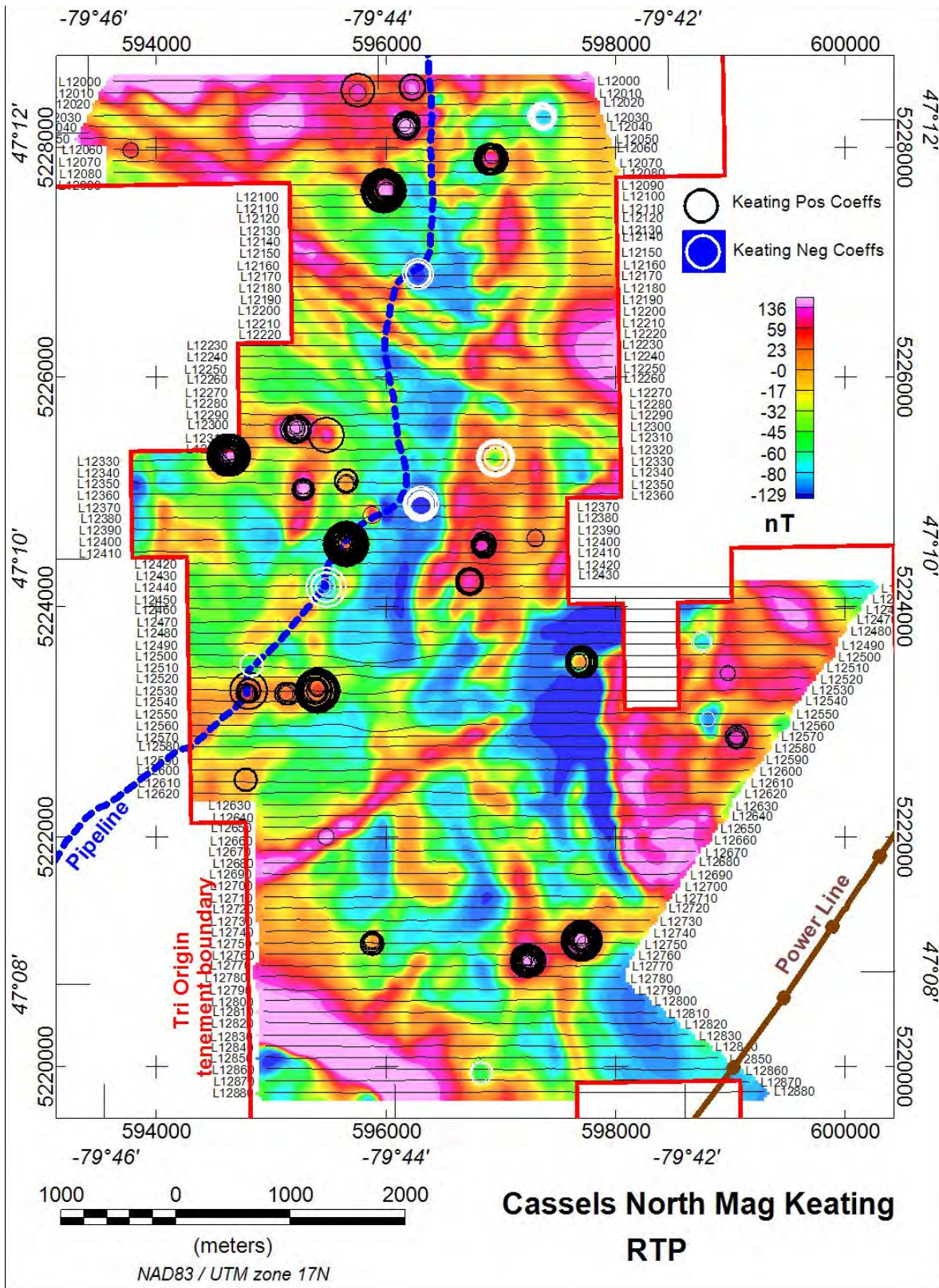


Figure 17: Cassels North: Keating Magnetic solutions superimposed on RTP.

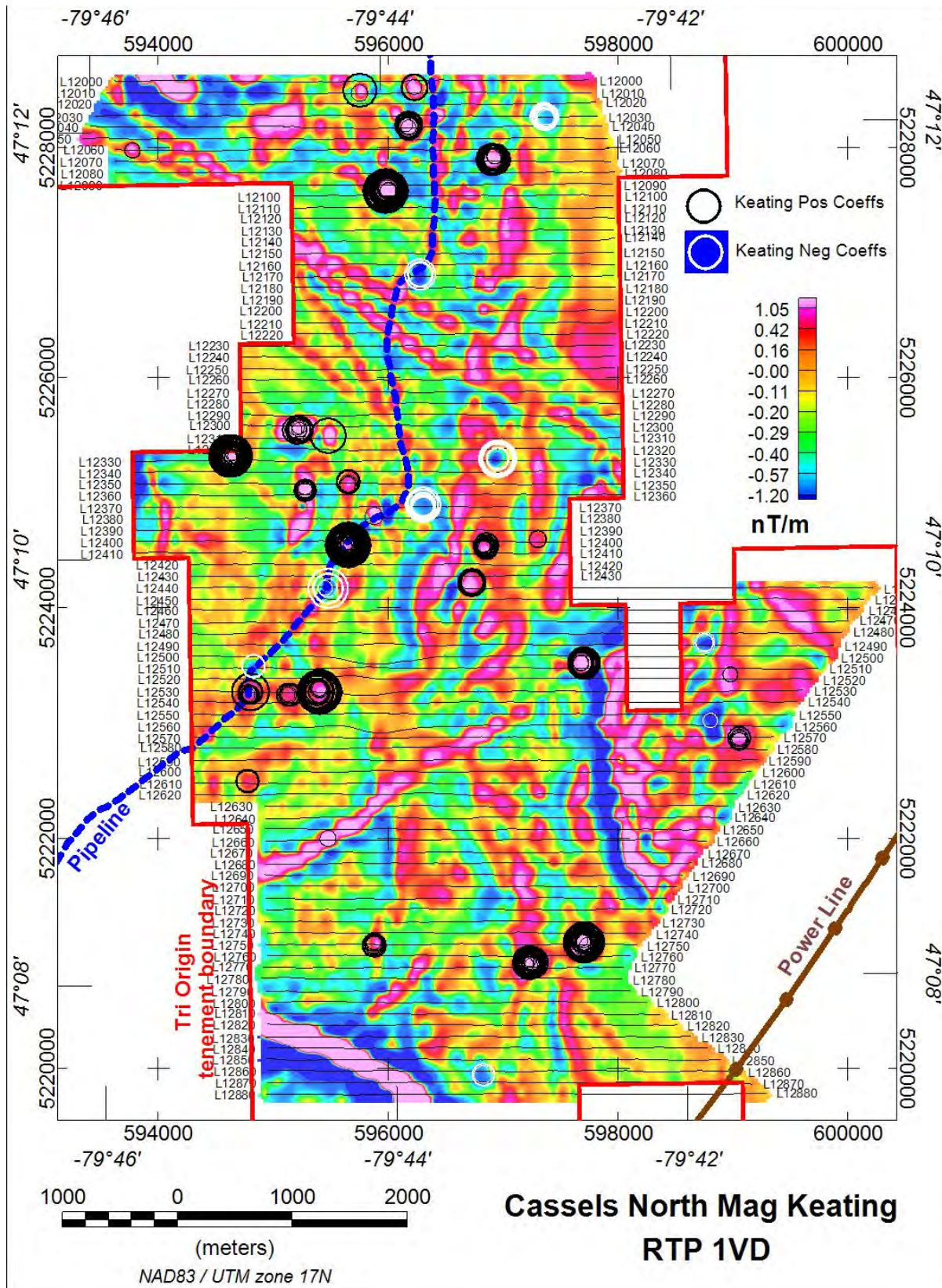


Figure 18: Cassels North: Keating Magnetic solutions superimposed on RTP 1VD.

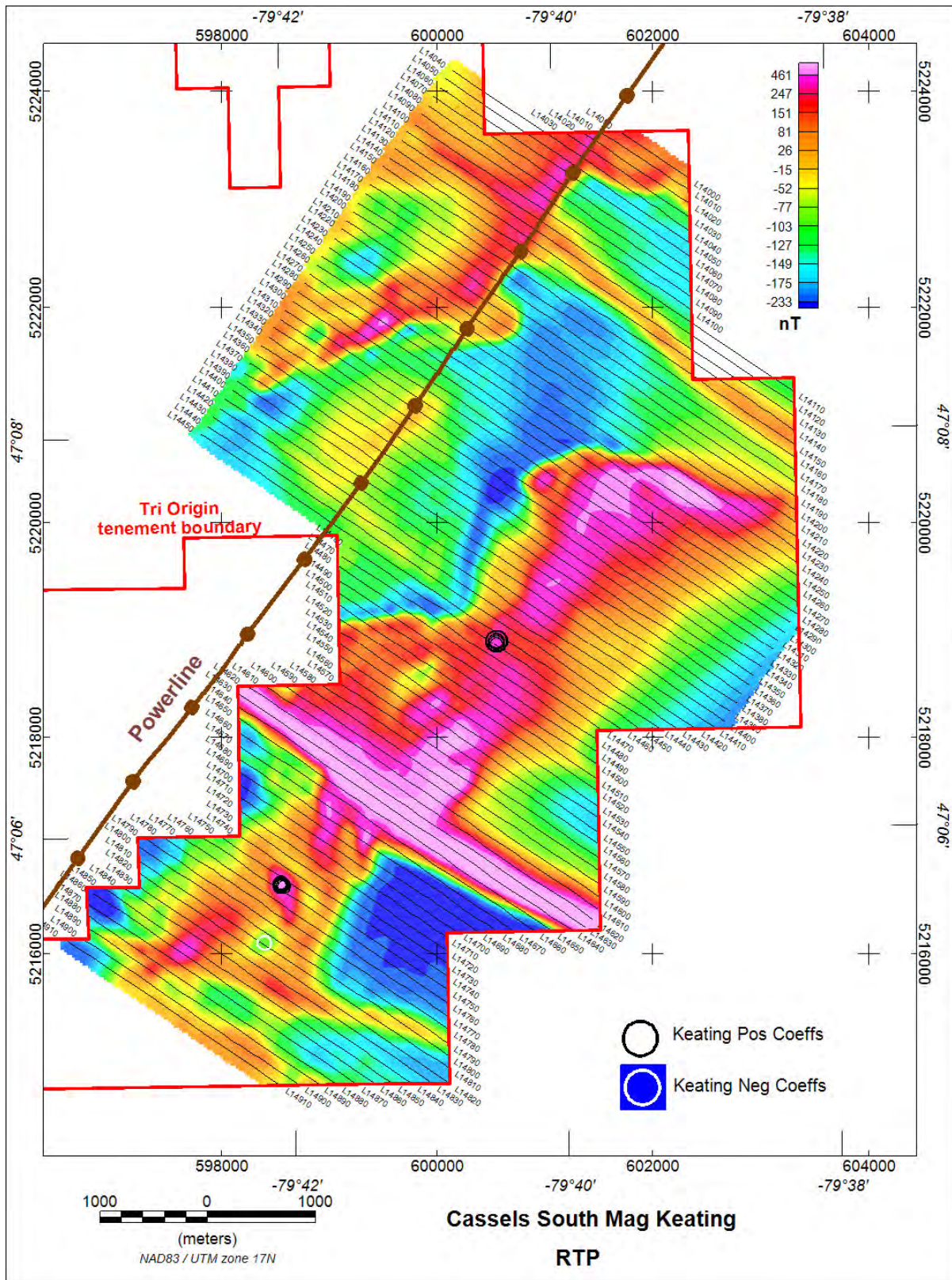


Figure 19: Cassels South: Keating Magnetic solutions superimposed on RTP.

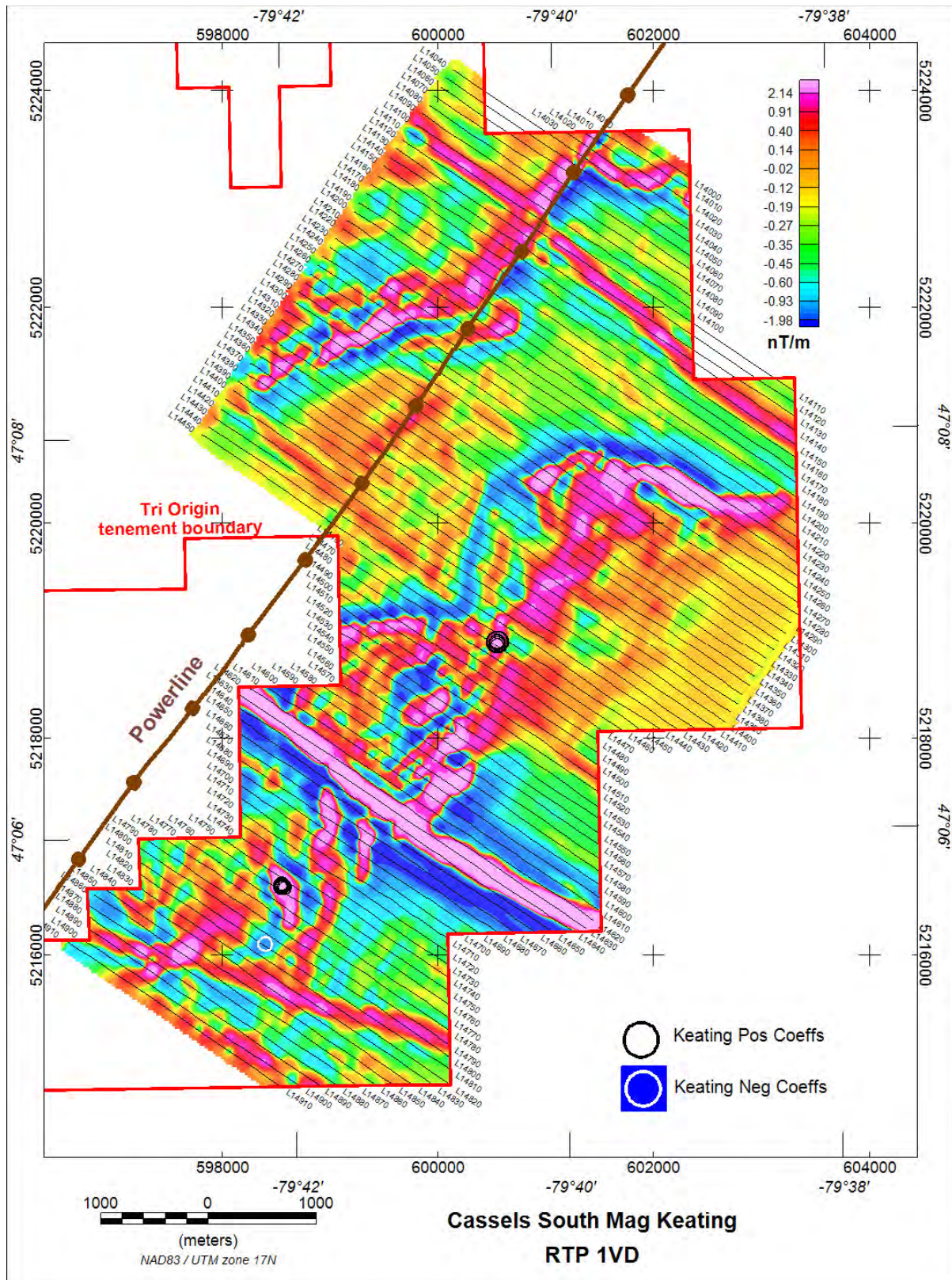


Figure 20: Cassels South: Keating Magnetic solutions superimposed on RTP 1VD

6. KEATING EM PROCESSING.

Condor has previously run Keating analysis on helicopter frequency domain EM data (see Technical Note 2004-1 in Appendix B). We considered that a similar approach would generate useful results for VTEM time domain data.

The EM response of typical kimberlites is considered to be generated by either (or both):

- The relatively low conductivity of the crater phase (or weathering/oxidation) at the top of the kimberlite (likened to a “hockey puck”).
- The unweathered kimberlite having a relatively low resistivity, sufficient to generate a significant EM anomaly. However, the rapid drop-off with depth of responses of airborne EM systems means that the near-surface portion of any kimberlite will dominate the EM response; thus also looking like a “hockey puck”.

An attempt was made to model this conductive “hockey puck” using Maxwell⁴ software, but unfortunately Maxwell models only rectangular plates and no reliable modeling could be generated for the “hockey puck”.

However, the general form of the EM anomalies appeared quite similar to those generated for the magnetic pipe. It was concluded that running the same set of Keating models used for the magnetic processing would provide useful results for the EM data. This was reinforced by the range of model responses produced by the variable radii (25 to 100 m) and depths (0 to 30 m below surface) of the magnetic modeling, which in combination produce a significant range of anomaly shapes applicable to the conductive responses of kimberlites.

The VTEM EM data was examined and it was concluded that SFz[6], a relatively early channel (0.031 msec) of the dB/dt Z component, was best mapping near-surface conductivity and this was used for the Keating EM analysis.

The Keating matched filtering generates an output file with X, Y locations of matching anomalies, together with information on the correlation coefficients. These data are inspected and a suitable

⁴ Maxwell is a product of EMIT, Perth Australia

threshold value for the correlation coefficient is selected to produce a manageable number of targets. For this study, a threshold correlation coefficient of 85% was used, together with a threshold Amplitude of 0.5.

The final locations are then overlain on a suitable base map - in this case the SFz[6] EM response. Only EM Keating solutions with positive coefficients are shown because negative coefficients imply resistive areas.

Because conductive lake sediments often generate significant early-time EM responses, the outlines of lakes have been superimposed on the SFz[6] image in a second set of figures.

The positive correlations are shown as black circles. The size of the symbols is proportional to the correlation coefficient. In many cases, several solutions occur close to one another (even after thresholding), so that the circles overlap and appear to be “thicker” than single solutions.

The Keating EM solutions for the five areas are shown in Figures 21-31.

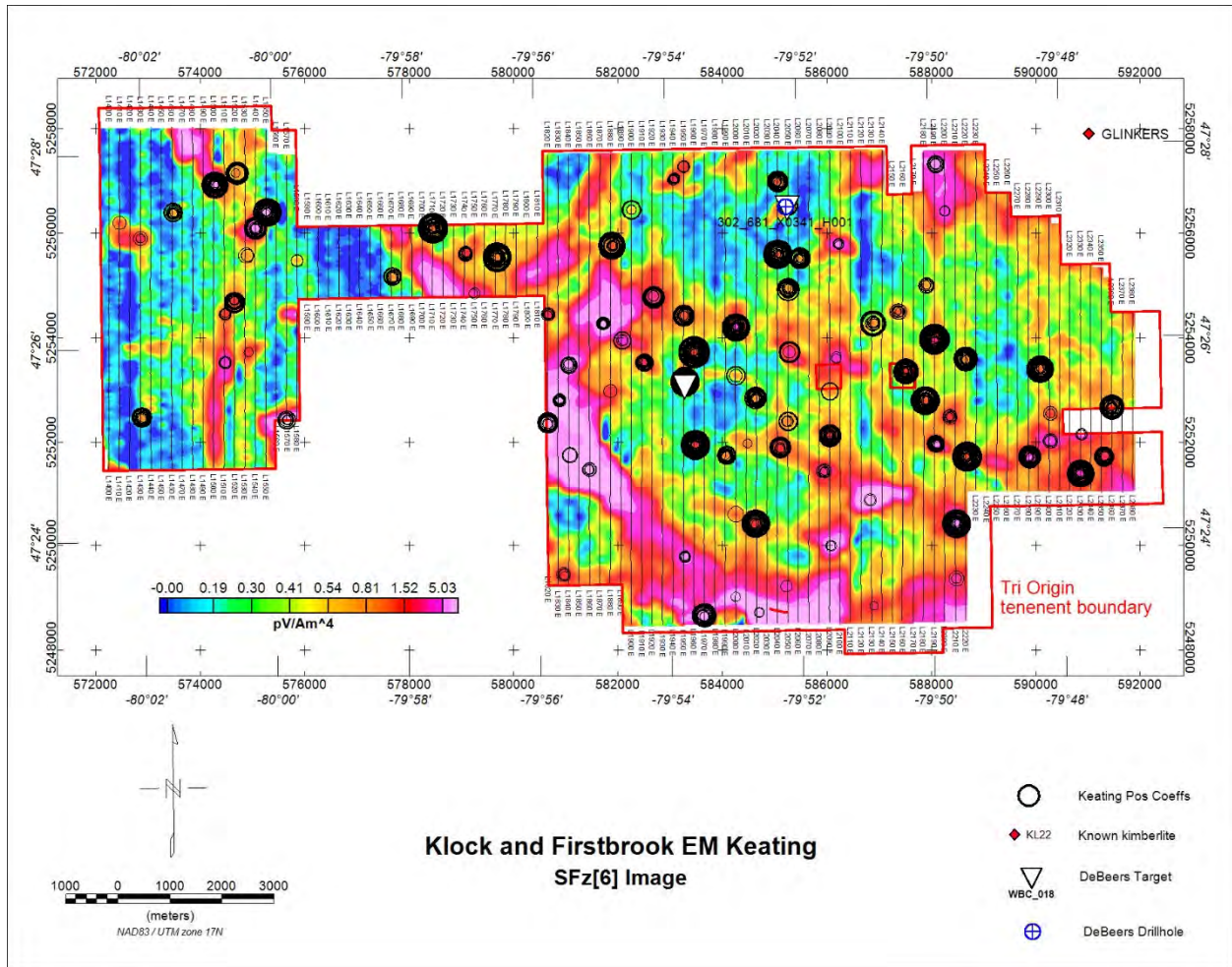


Figure 21: Klock and Firstbrook Keating EM solutions superimposed on SFz[6] image. The size of the symbols is proportional to the correlation coefficient. Only solutions with a Correlation Coefficient above 85% are shown.

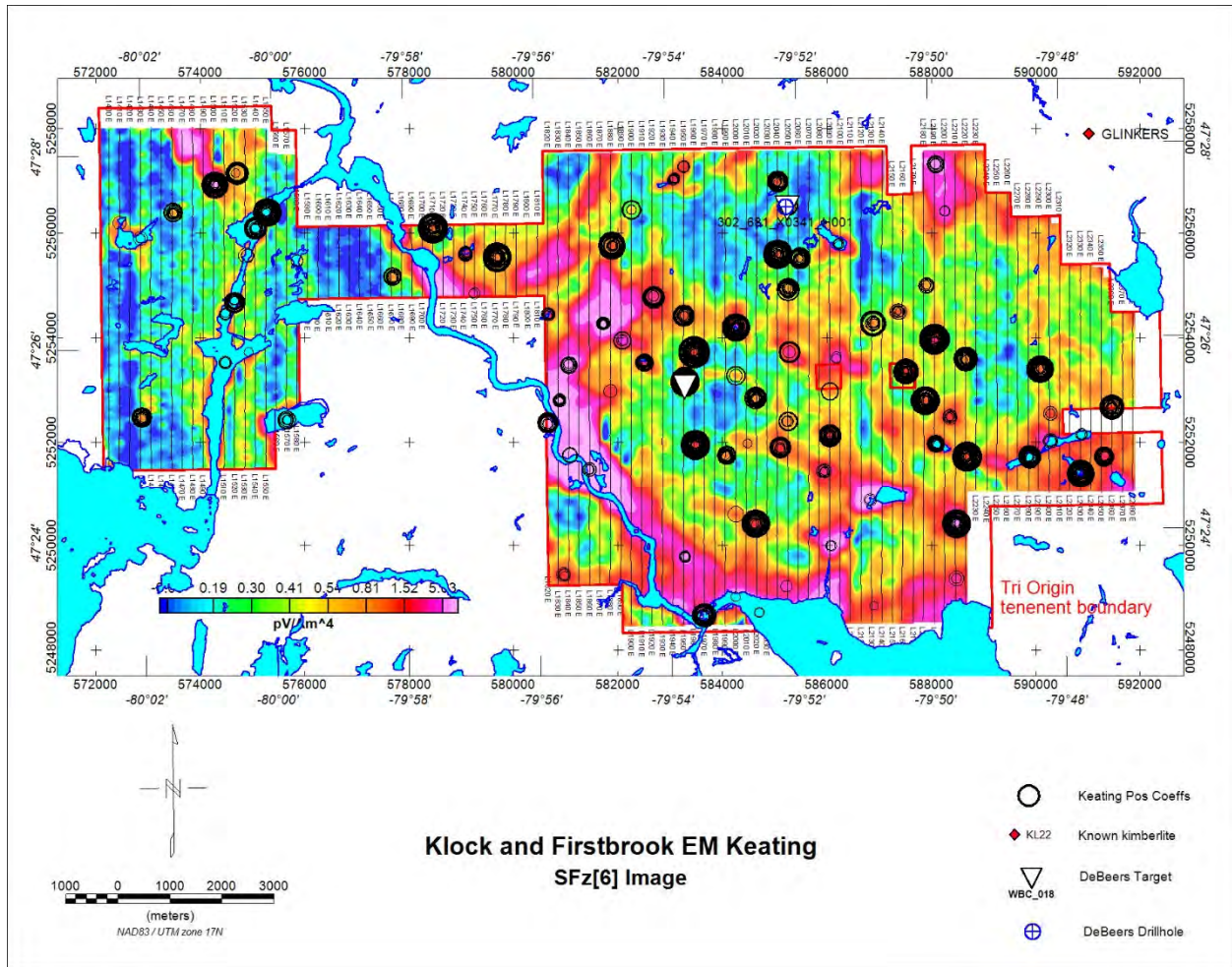


Figure 22: Klock and Firstbrook Keating EM solutions superimposed on SFz[6] image with lakes overlain. The size of the symbols is proportional to the correlation coefficient. Only solutions with a Correlation Coefficient above 85% are shown.

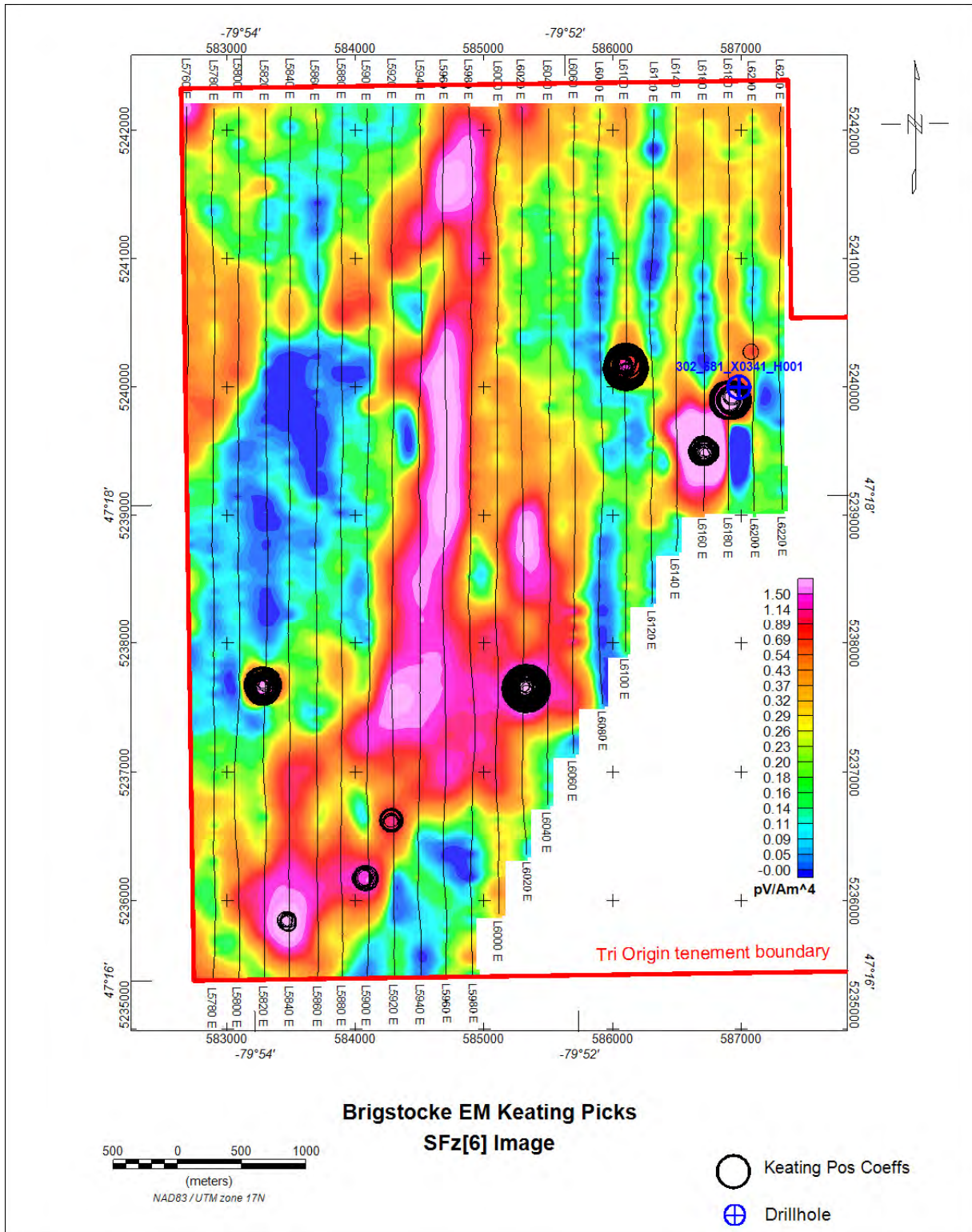


Figure 23: Brigstocke Keating EM solutions superimposed on SFz[6] image.

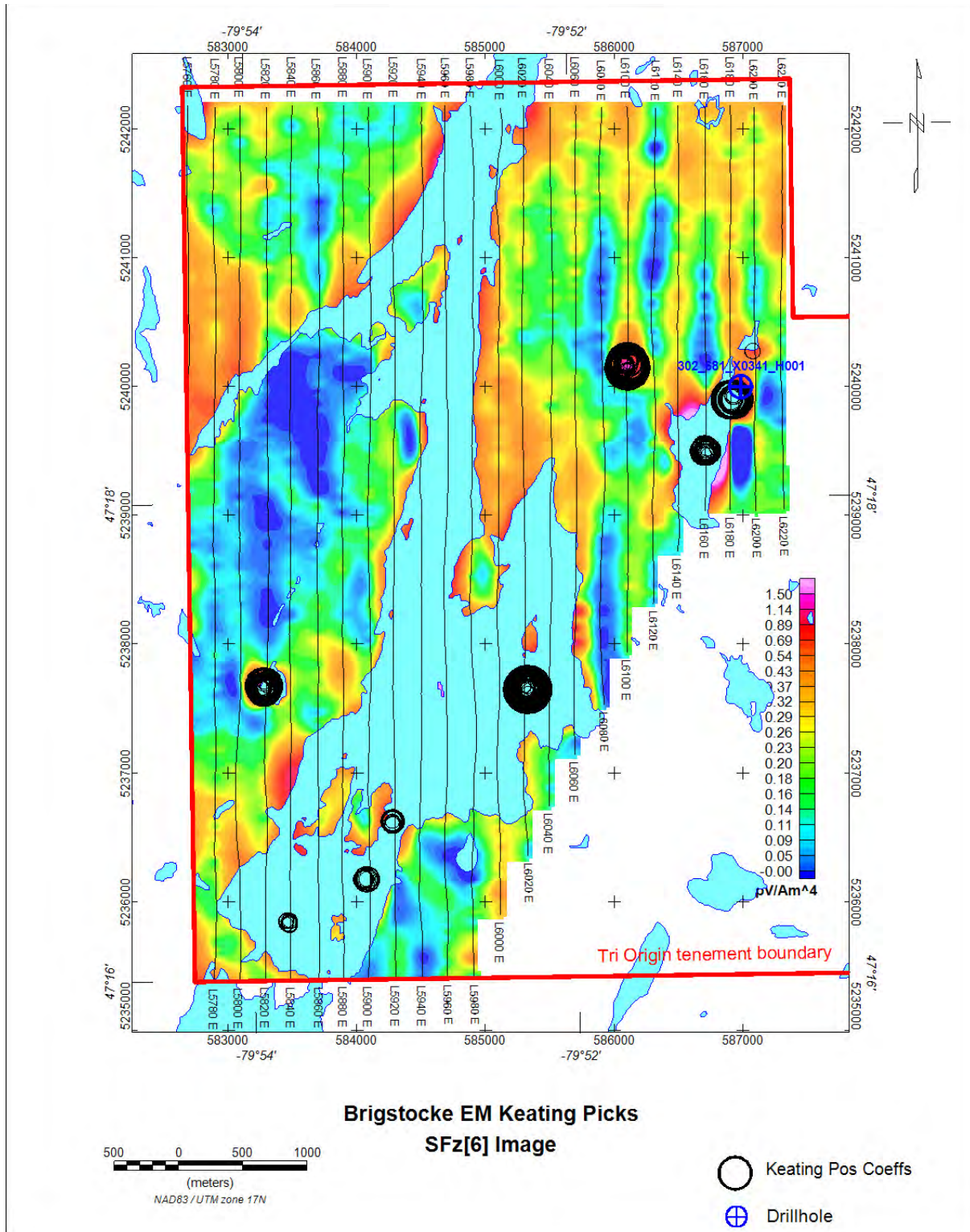


Figure 24: Brigstocke Keating EM solutions superimposed on SFz[6] image, with lakes overlain.

The area in the vicinity of De Beers drill hole is shown in Figure 25. The drill hole location is close to a Keating EM solution, corresponding to a sub-circular discrete conductive zone. This also correlates with the northern end of a small lake, suggesting that the conductivity may be due to lake sediments, possibly overlying the weathered top of a kimberlite pipe. A second Keating EM solution lies approximately 450 m to the SSW, also within the lake boundary.

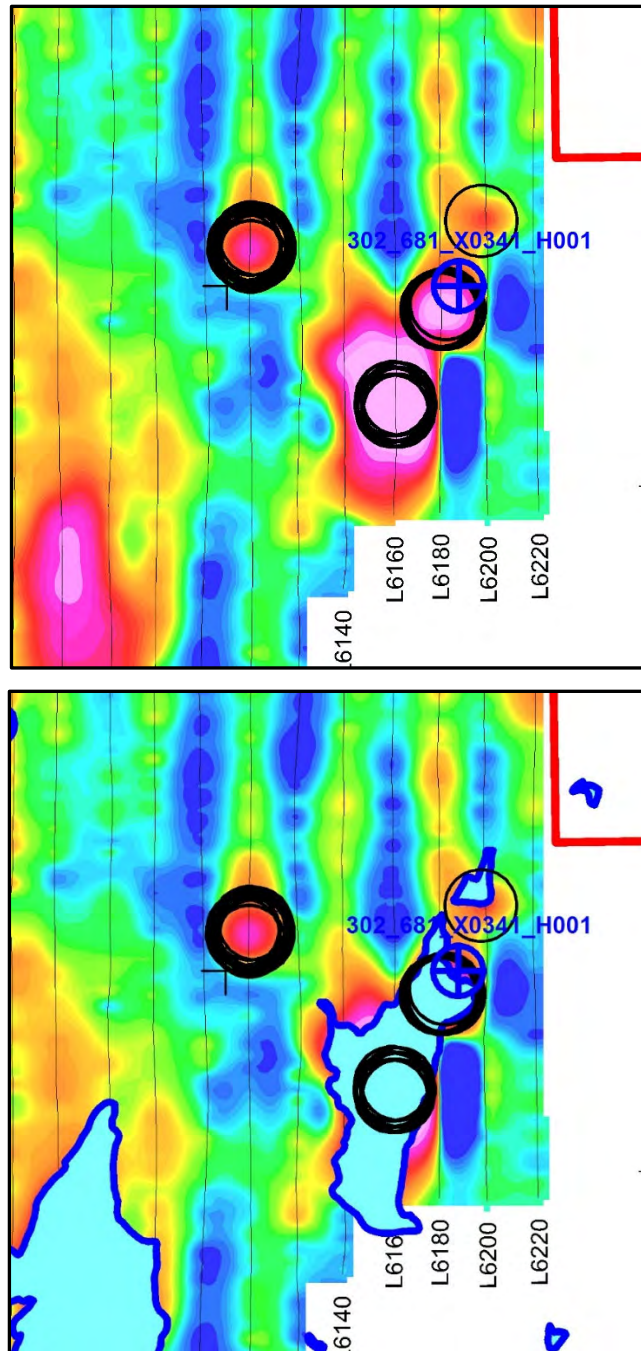


Figure 25: Brigstocke SFz[6] image in area of De Beers drill hole (top). Same image, also showing lakes (bottom).

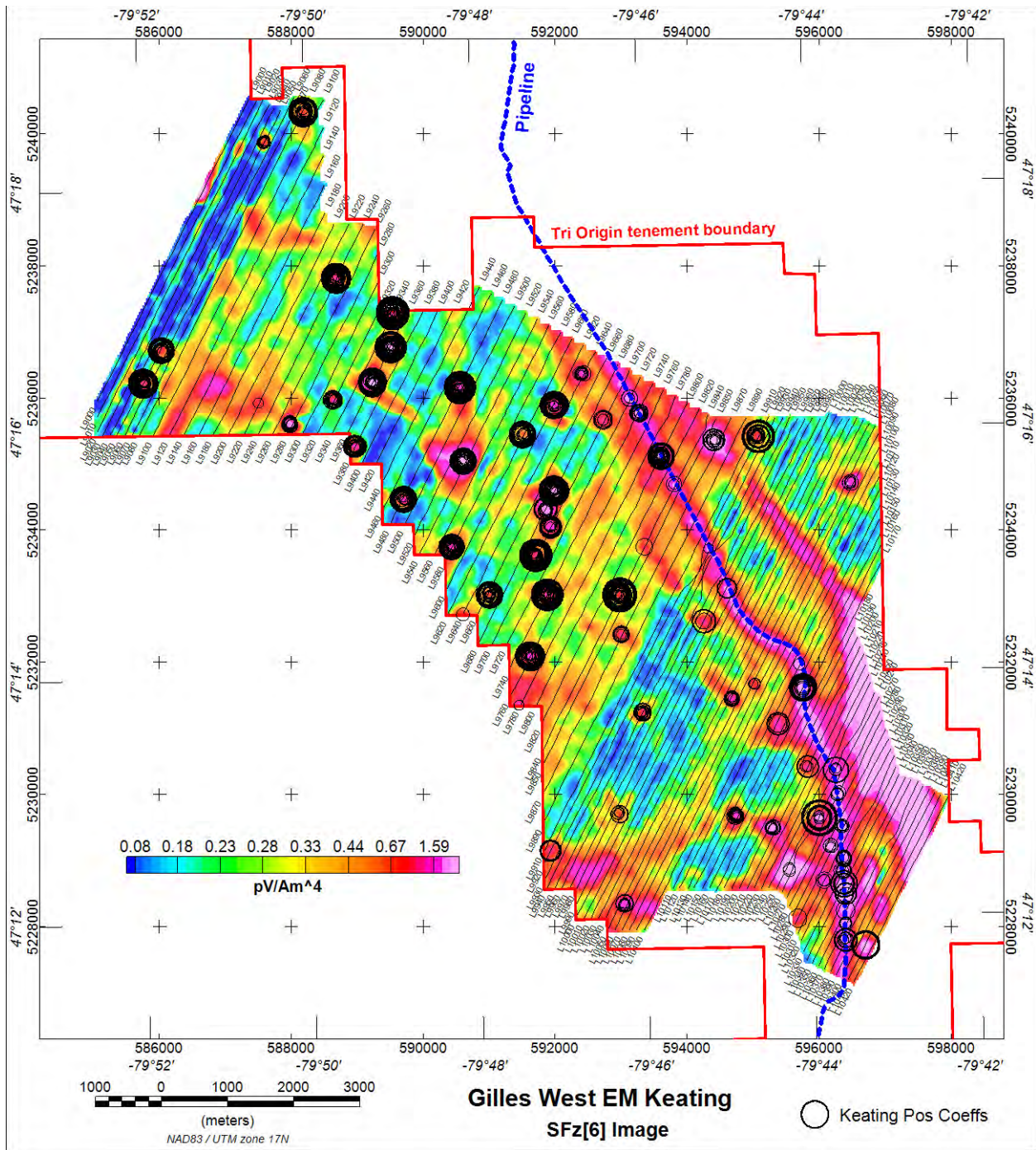


Figure 26: Gilles West Keating EM solutions superimposed on SFz[6] image.

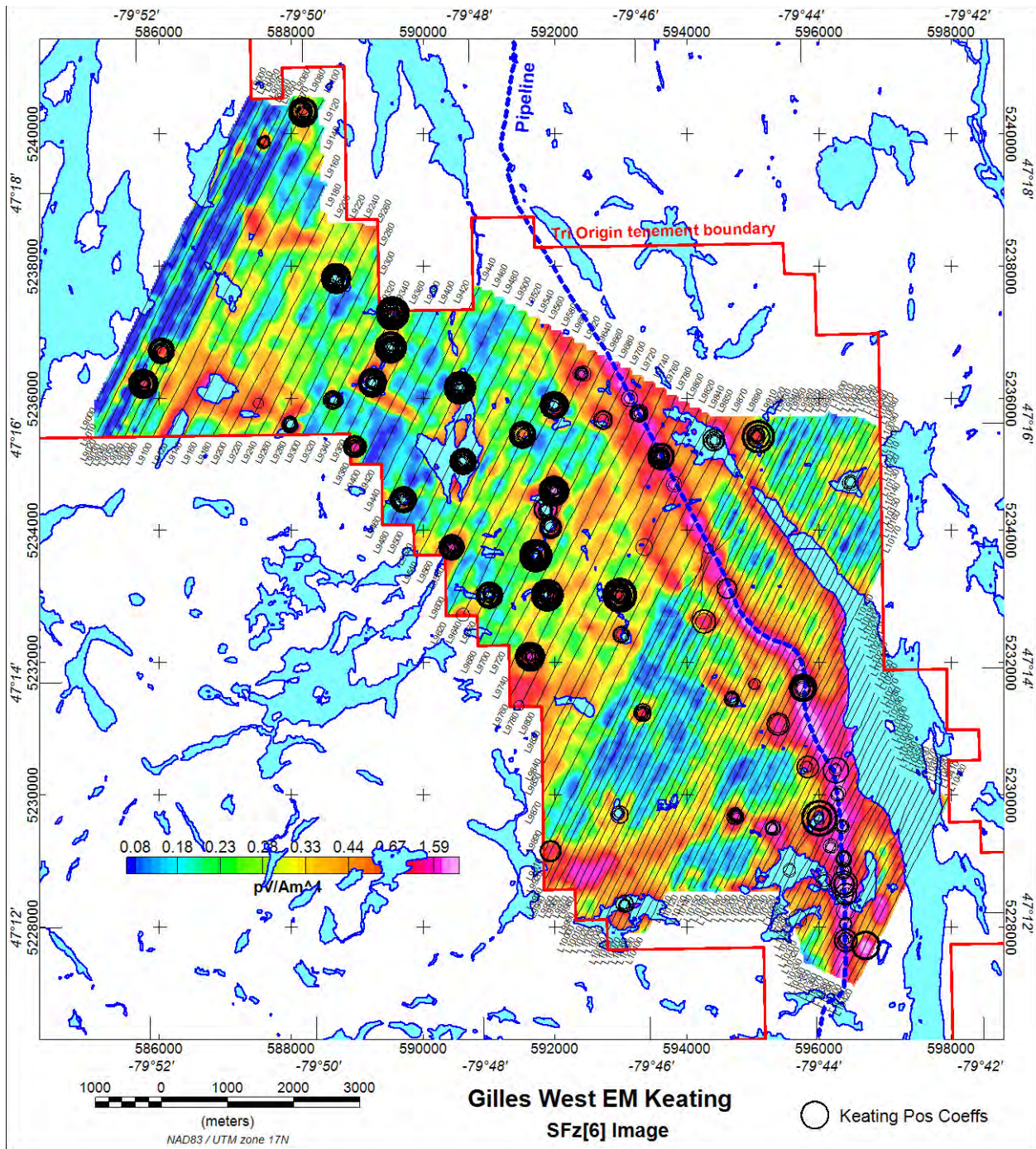


Figure 27: Gilles West Keating EM solutions superimposed on SFz[6] image, with lakes overlain.

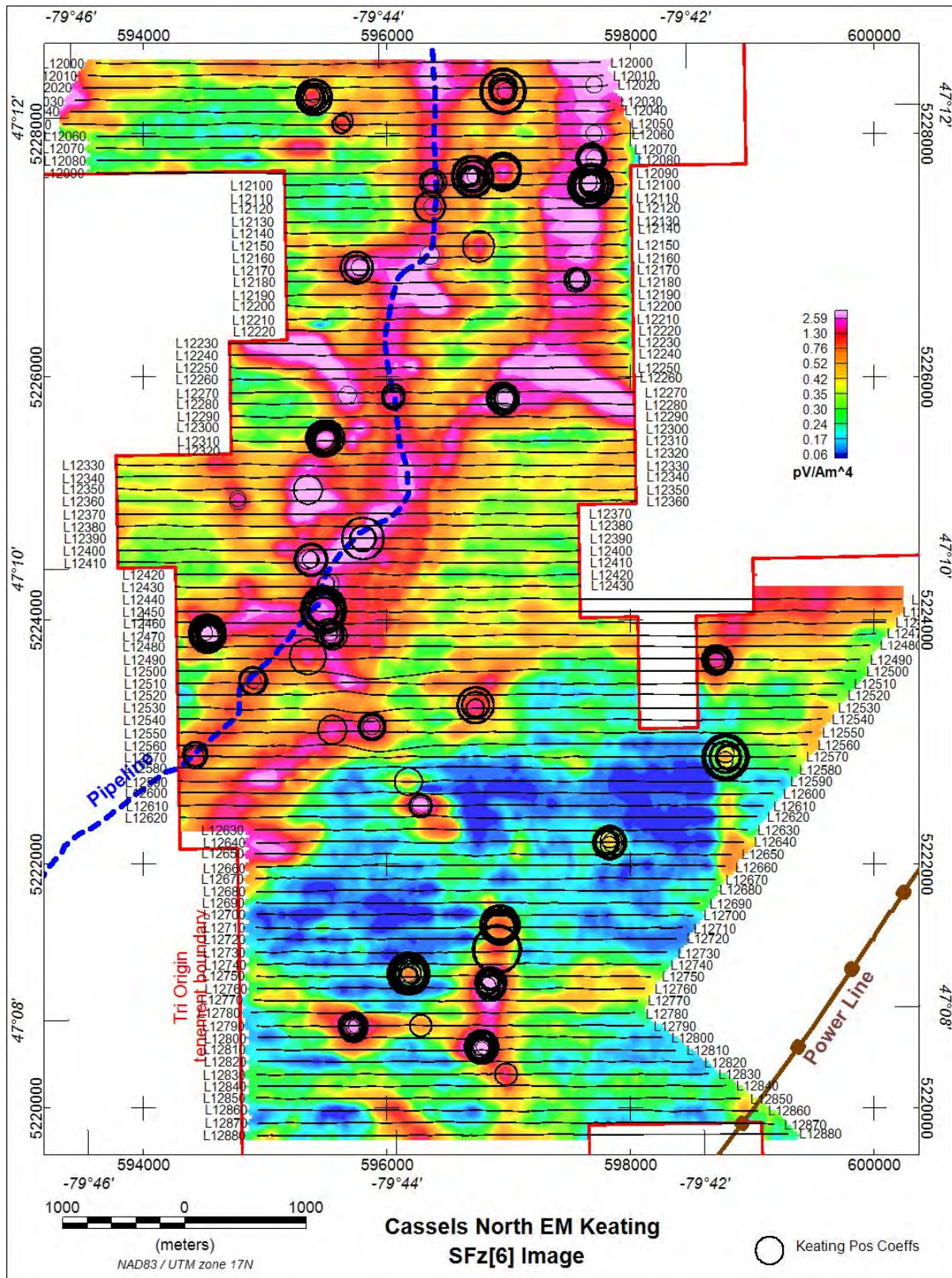


Figure 28: Cassels North Keating EM solutions superimposed on SFz[6] image.

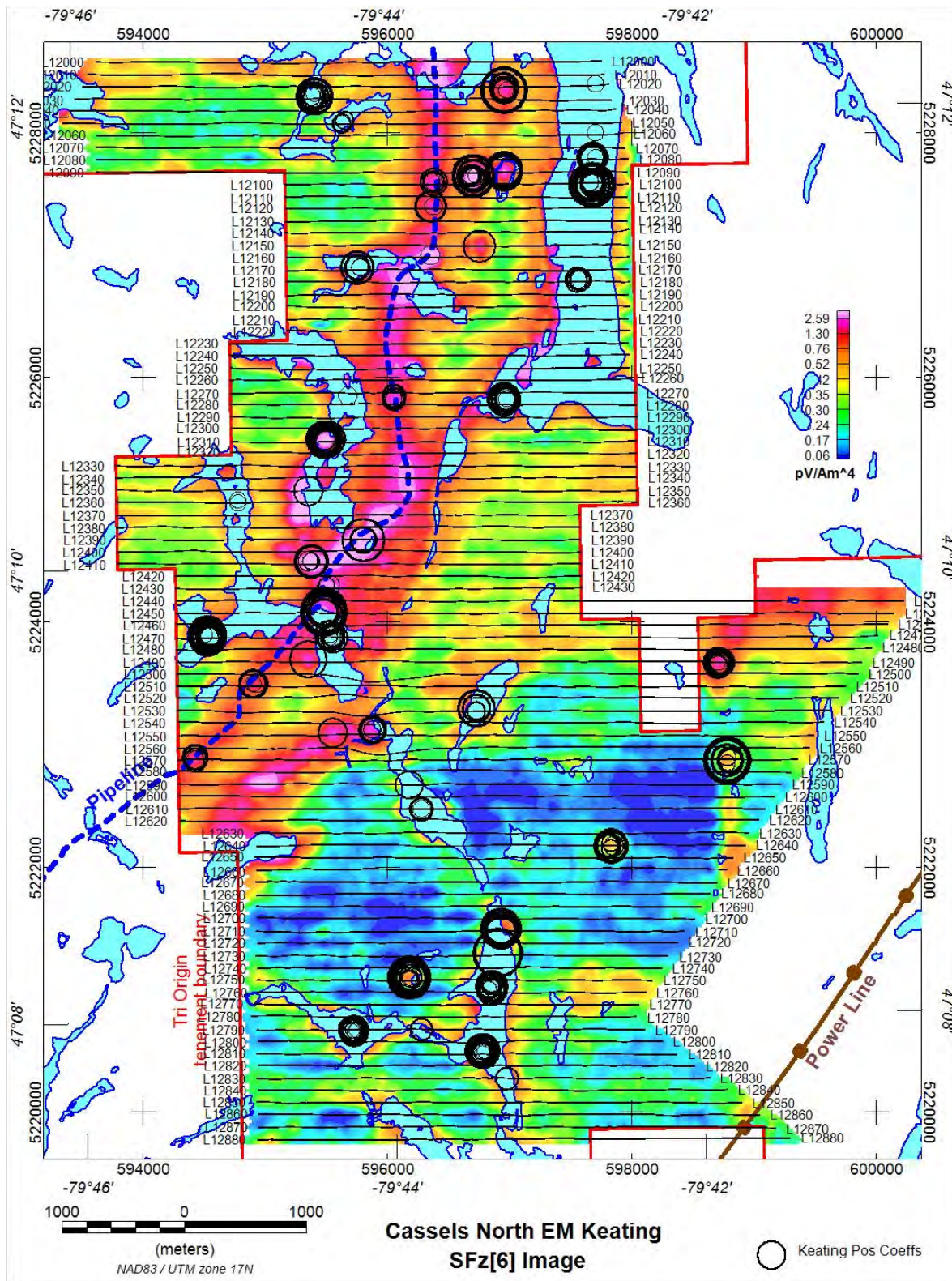


Figure 29: Cassels North Keating EM solutions superimposed on SFz[6] image, with lakes overlain.

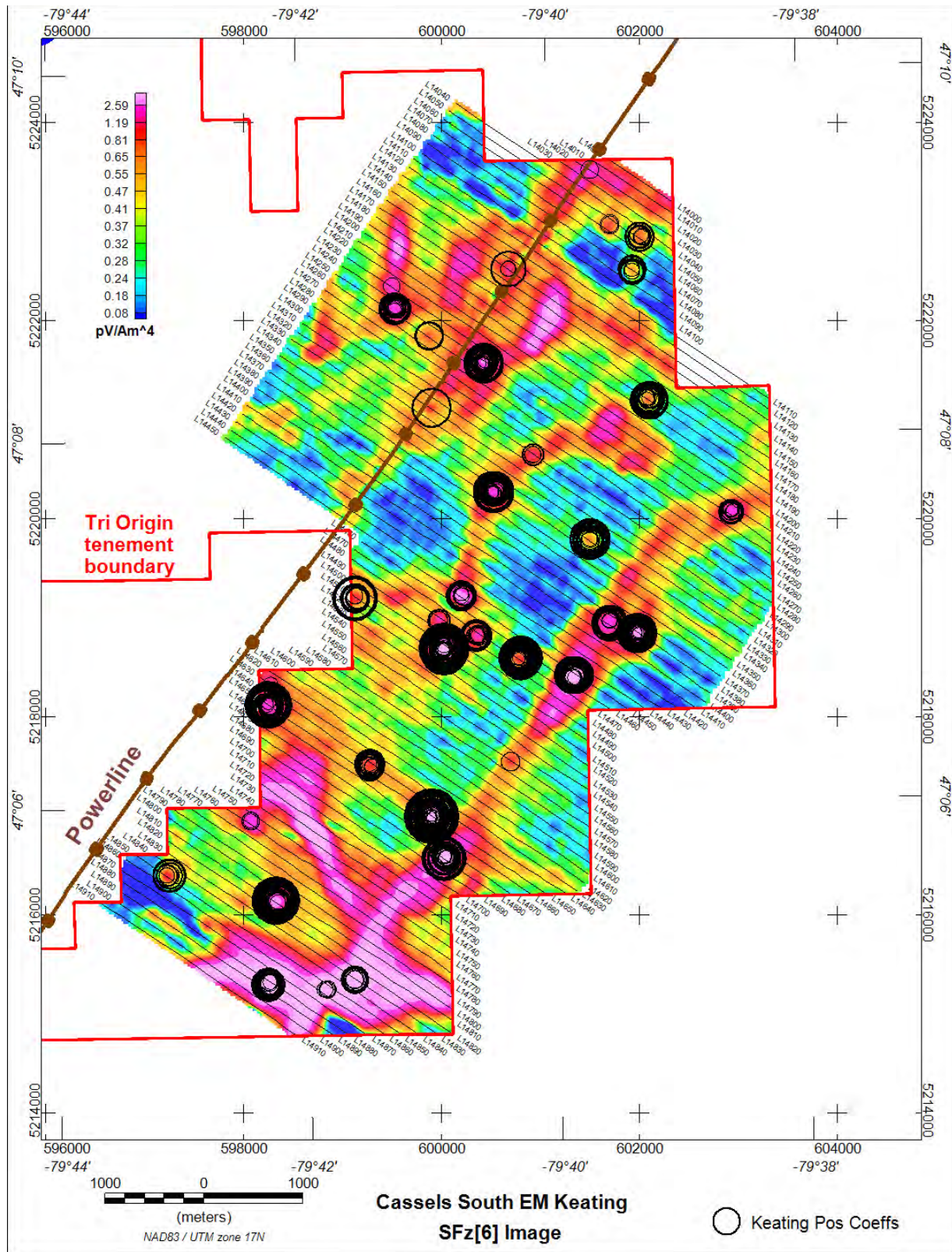


Figure 30: Cassels South Keating EM solutions superimposed on SFz[6] image.

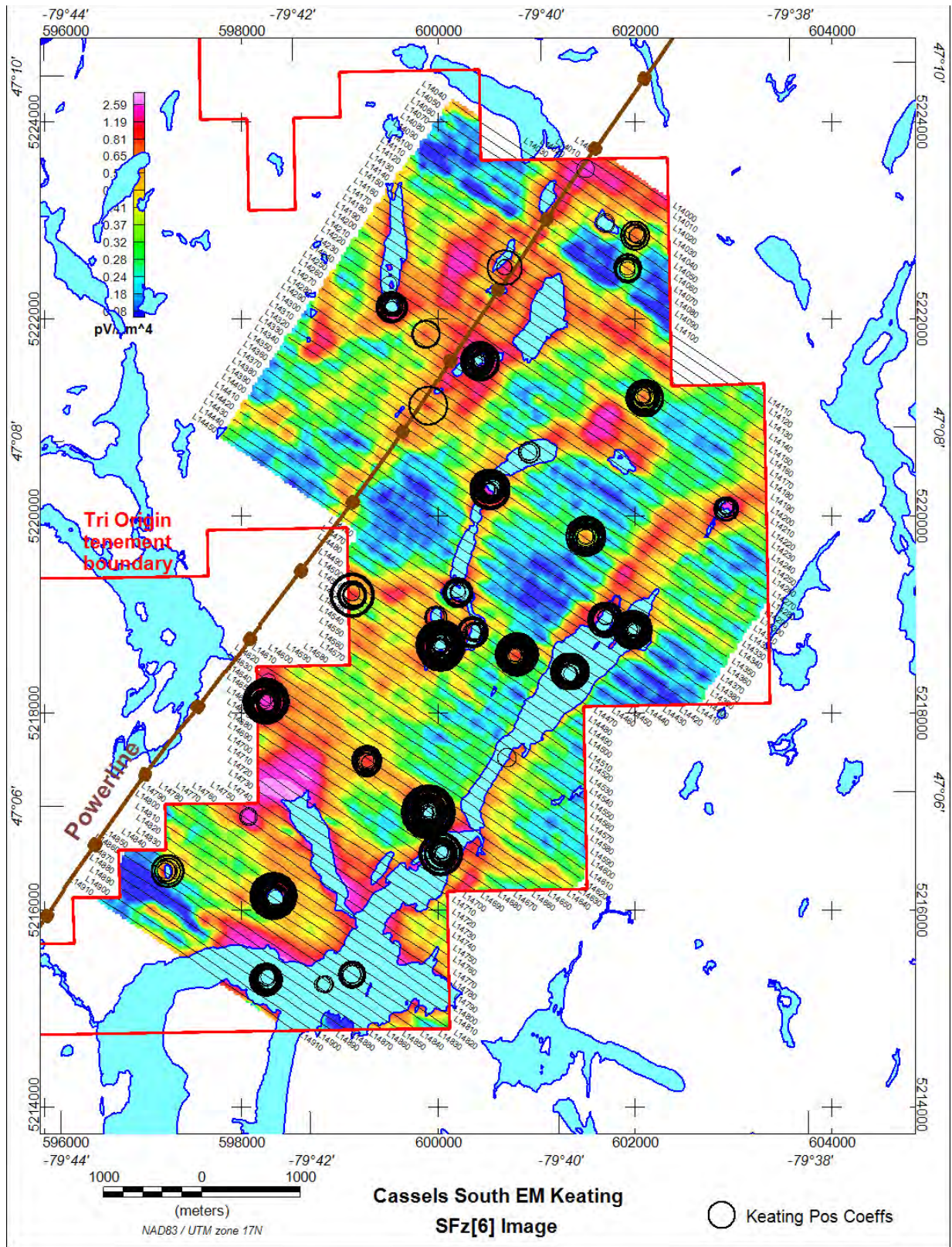


Figure 31: Cassels South Keating EM solutions superimposed on SFz[6] image, with lakes overlain.

7. MAG AND EM SOLUTIONS COMBINED

To visualize the correlation between the magnetic and EM Keating solutions, both sets of data have been overlain on the following maps (Figures 32-36). The base image in each case is the magnetic RTP 1VD. In these maps, the EM solutions are shown as blue triangles.

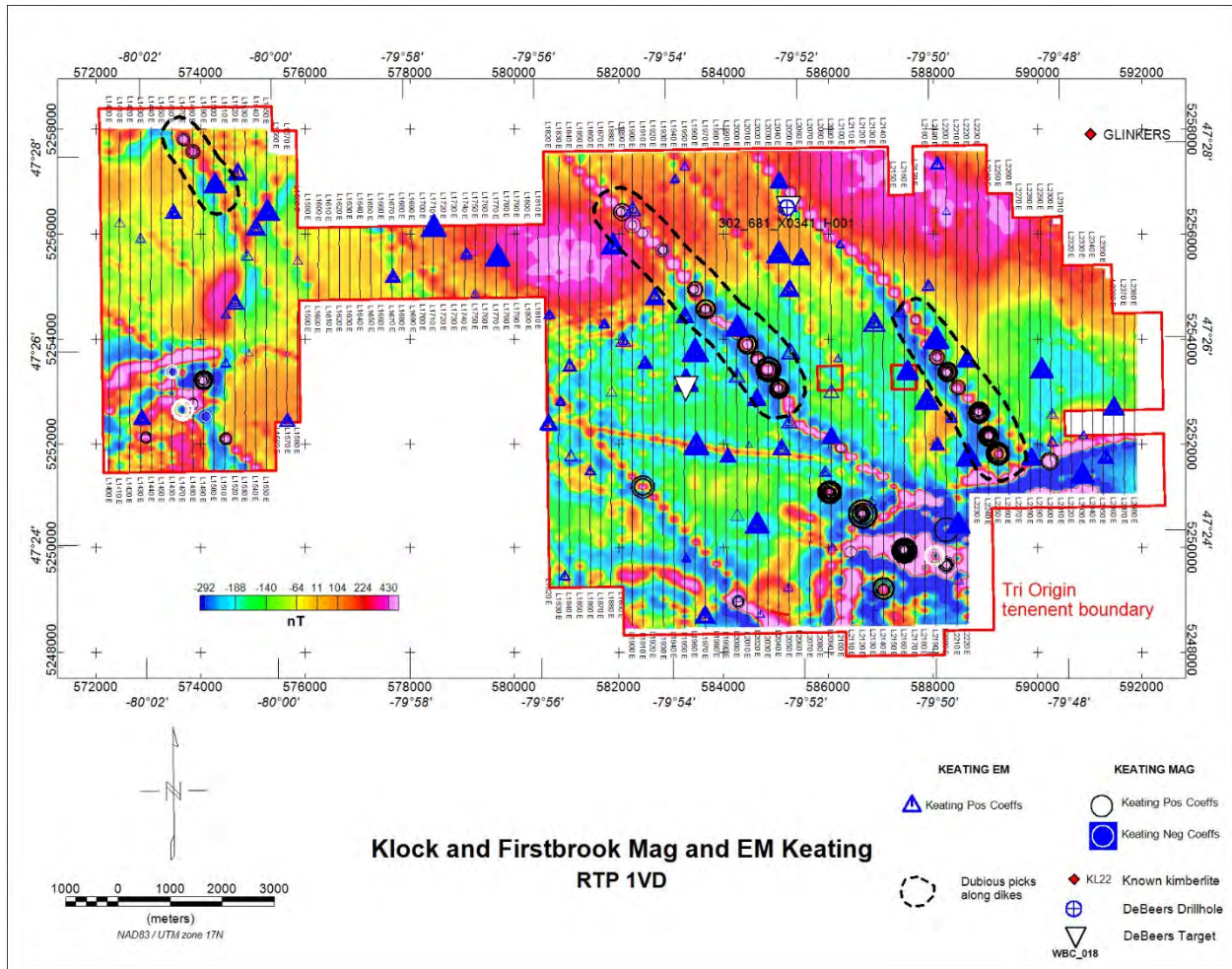


Figure 32: Klock and Firstbrook Mag and EM solutions combined, overlain on RTP 1VD image. The size of the symbols is proportional to the correlation coefficient. Only solutions with a Correlation Coefficient above 85% are shown.

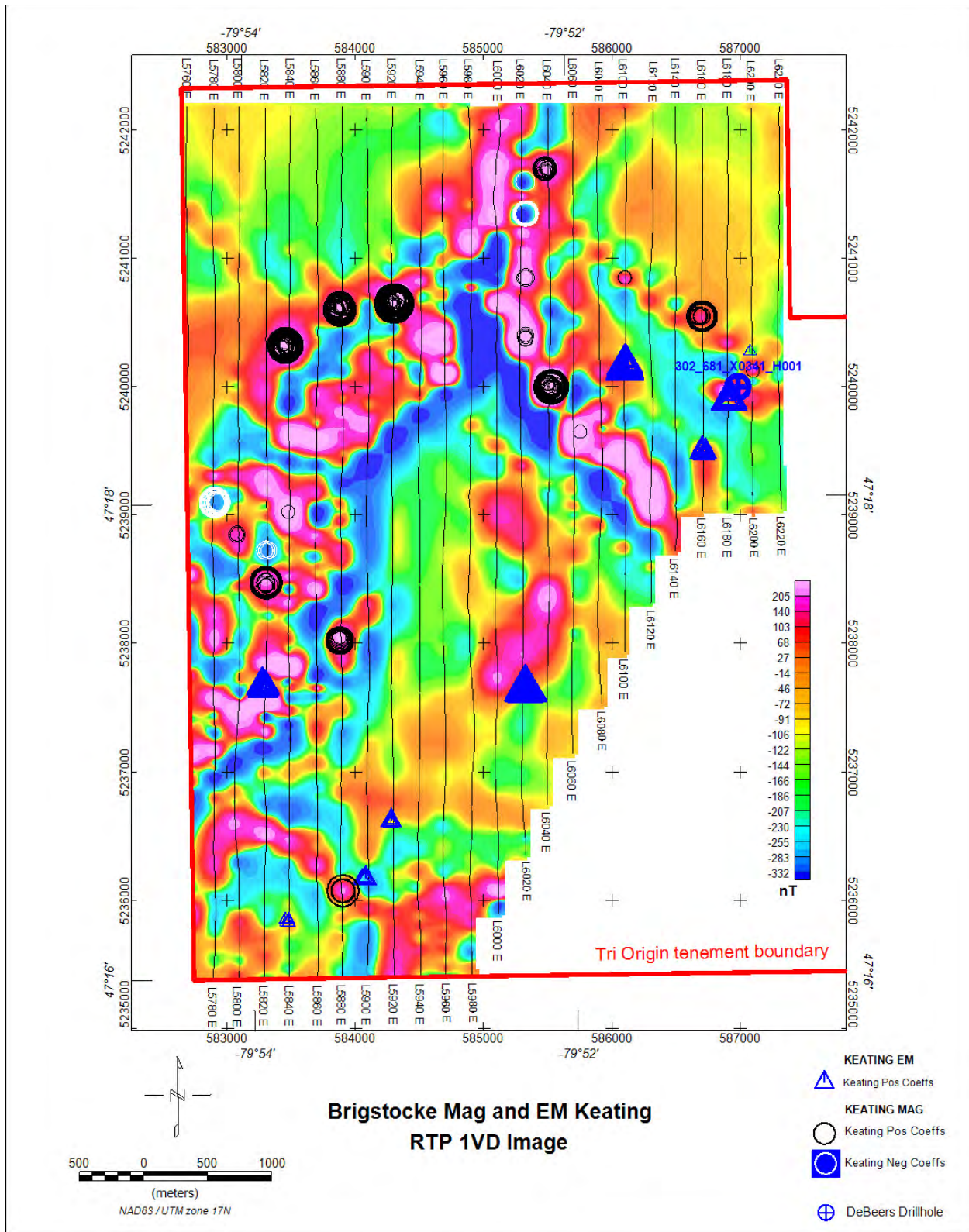


Figure 33: Brigstocke Mag and EM solutions combined, overlain on RTP 1VD image.

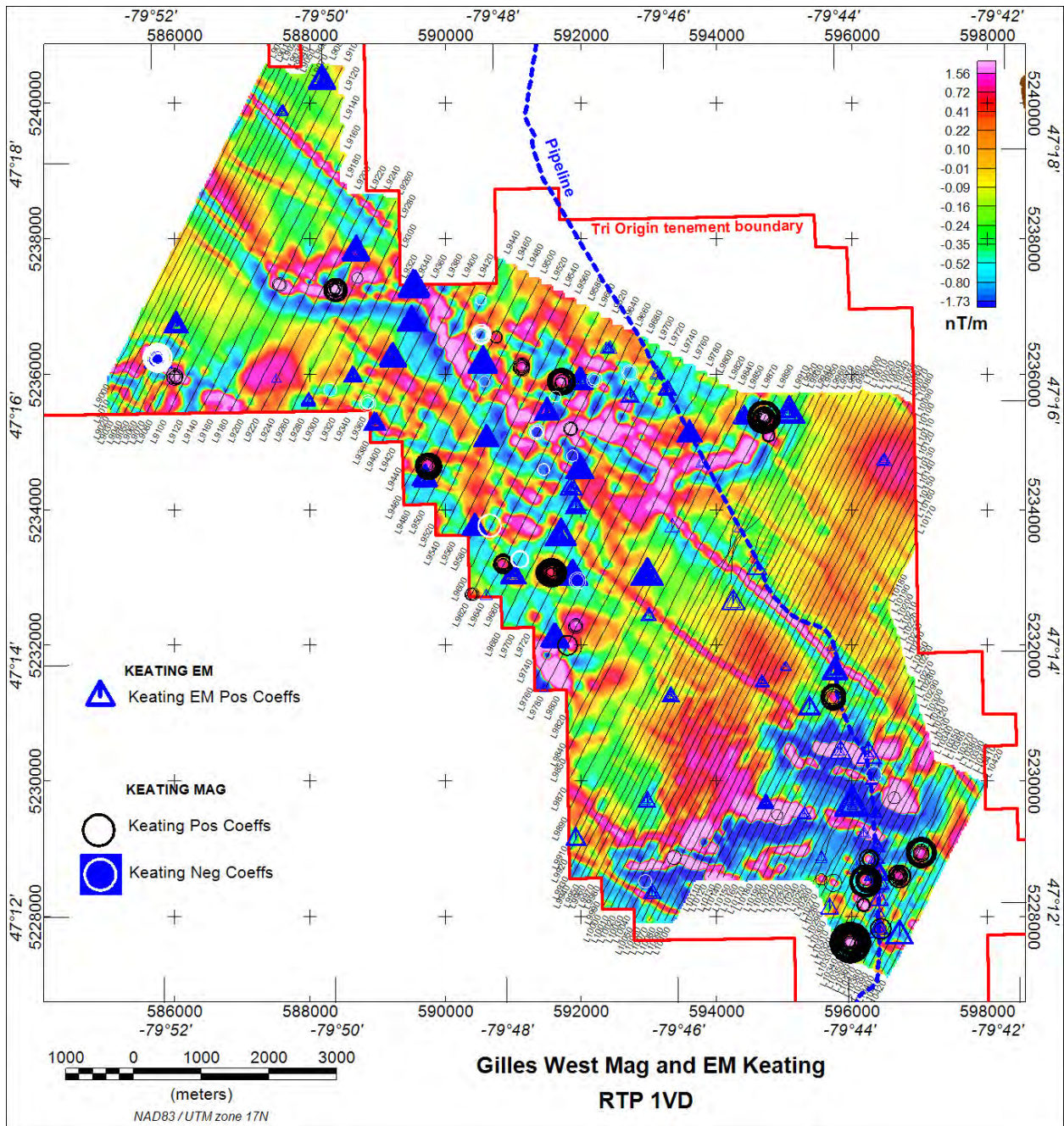


Figure 34: Gilles West Mag and EM solutions combined, overlain on RTP 1VD image.

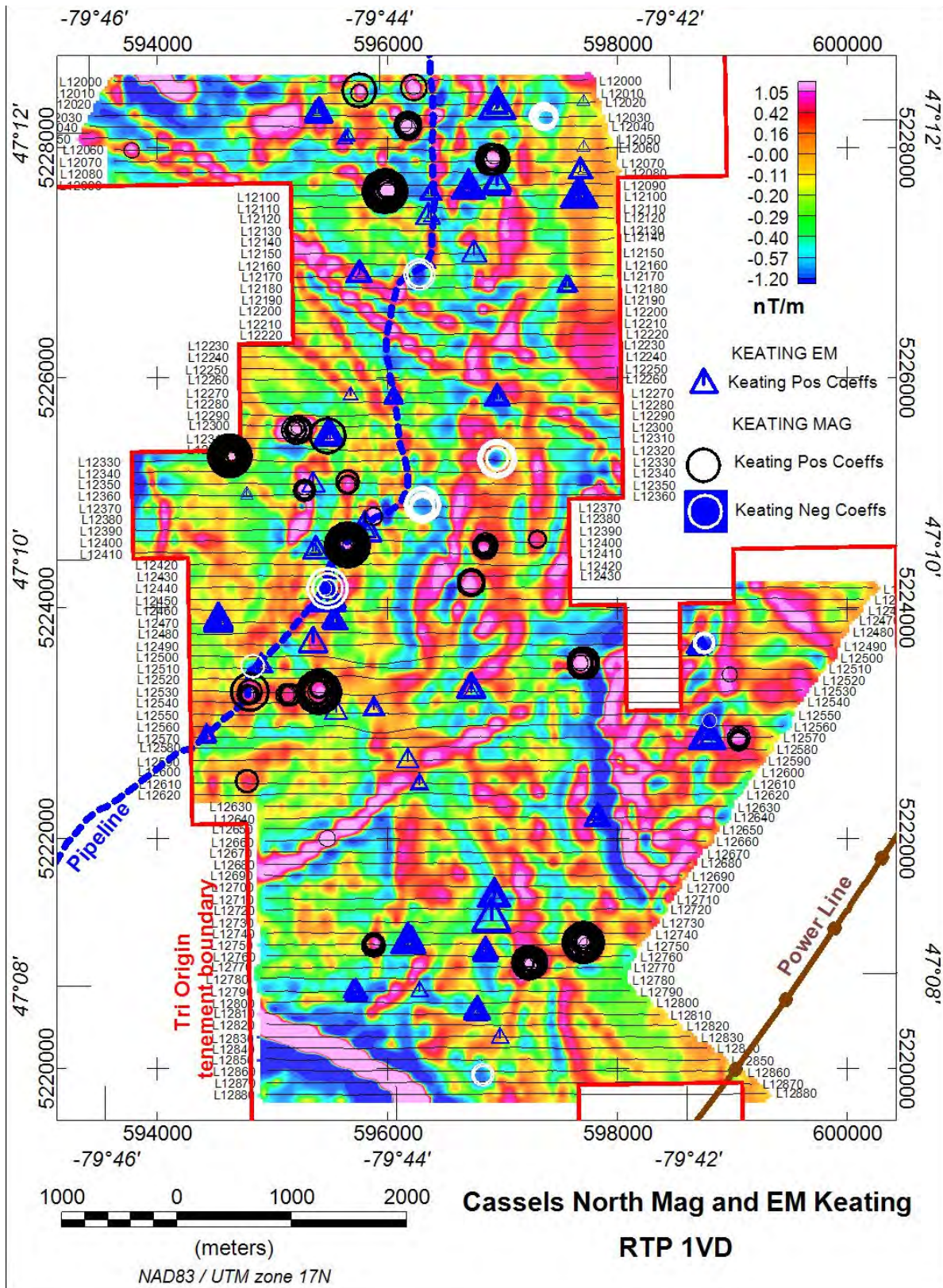


Figure 35: Cassels North Mag and EM solutions combined, overlain on RTP 1VD image.

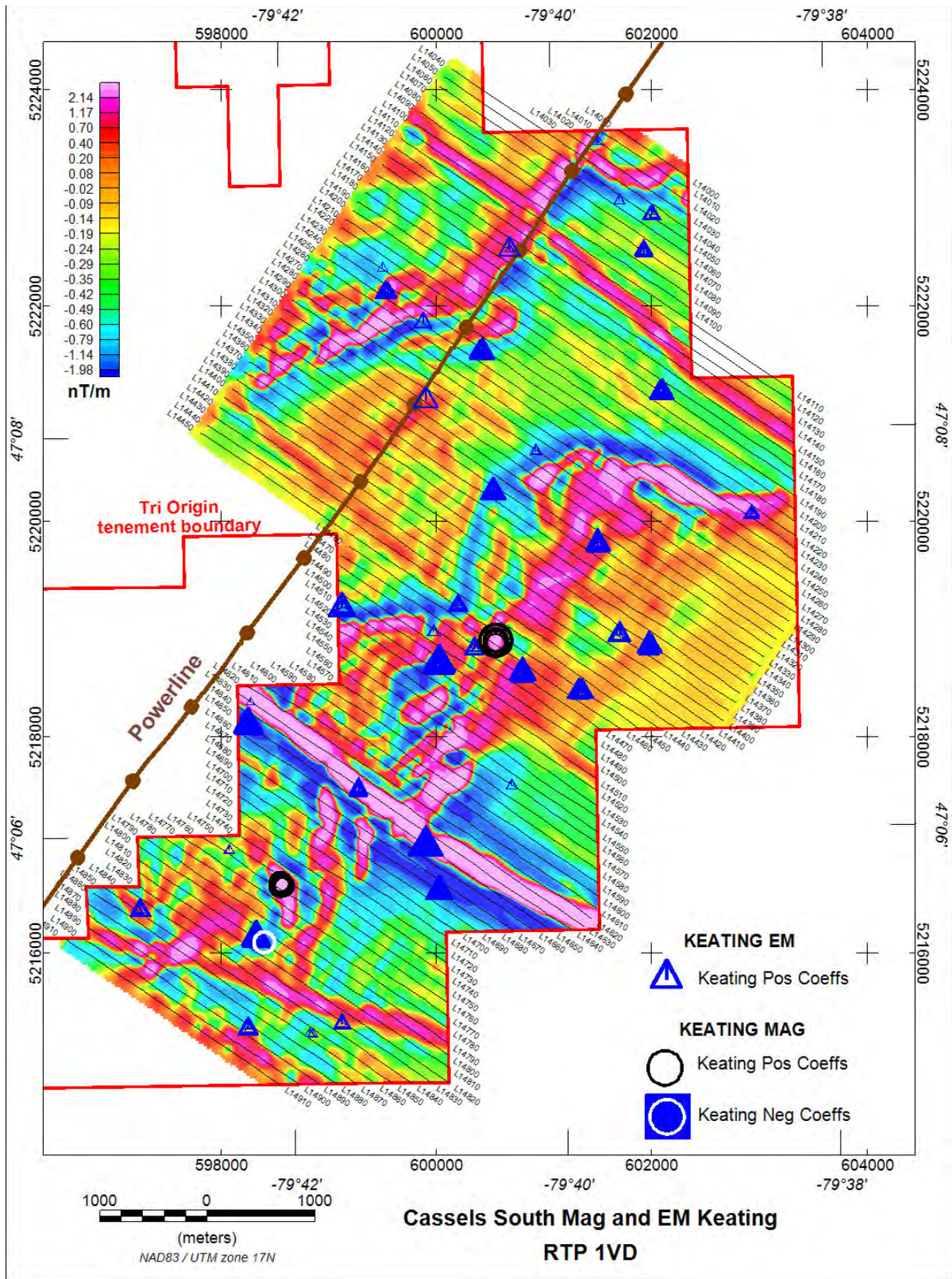


Figure 36: Cassels South Mag and EM solutions combined, overlain on RTP 1VD image.

8. DISCUSSION

Despite the Keating analysis of the EM data being based on theoretical magnetic models, the EM solutions correlate with early dB/dt channel anomalies that make sense geophysically, i.e. could be selected by a manual, human interpretation as possibly caused by kimberlite pipes.

As shown in the maps in Section 7, the correlation between Keating Mag and EM solutions is relatively poor. Subjectively, one may consider that the magnetic Keating solutions are more reliable than the EM solutions.

9. PRODUCTS

Table 9-1 lists the maps and products that are provided for each of the five VTEM survey blocks. Other products can be prepared from the existing datasets required.

All maps are created using the following datum and projection parameters:

- Ellipsoid: GRS80
- Datum: NAD83
- Projection: UTM (Zone: 17N)

Table 9-1 Survey Products

1. Database of LEI
2. MAG3D voxel inversion of magnetic data (.msh and .sus files)
3. MultiPlots™ (as described in Section 4)
4. Excel spreadsheets of magnetic Keating solutions (positive and negative)
5. Excel spreadsheet of Keating EM solutions
6. Oasis Montaj packed maps showing Keating magnetic solutions superimposed on RTP and RTP 1VD images.
7. Oasis Montaj packed maps showing Keating EM solutions superimposed on SFz[6] VTEM channel image.

10. CONCLUSIONS AND RECOMMENDATIONS

The Keating matched filtering method applied to airborne magnetic and EM data is a useful additional tool in defining kimberlite targets in large airborne magnetic and EM data sets. Human anomaly picking is flexible, but depends heavily on the experience of the interpreter and is inherently subjective. The Keating method has the advantage of being relatively fast and objective. In our experience it has delineated targets that we had not picked manually and so is very useful in adding to the thoroughness of the interpretation process.

However, the method is effectively limited to sub-circular anomalies and will not define targets which are distinctly ovoid or linear in shape. So, the method is not a panacea, but rather an adjunct to manual picking of targets.

To further progress diamond exploration in this area, the authors recommend that the client consider hiring an exploration geologist or geophysicist with extensive experience in kimberlite diamond exploration in this geological environment, who can further assess the Keating magnetic and EM solutions generated in this study, in conjunction with geological data and design a future exploration program.

If there is sufficient encouragement from immediate follow up, we suggest that areas of interest be re-flown with much higher resolution magnetics (and possibly EM). The existing VTEM surveys have line spacings of 100 m to 200 m and magnetic sensor height approximately 60 m above ground. A new survey with 40-50 m line spacing and sensor height of no greater than 30 m (employing gradient magnetic sensors) would generate higher resolution magnetic images more appropriate for kimberlite pipe exploration. A helicopter survey will likely be most cost-effective, but drone magnetic surveys could be useful over small areas (as shown by RJK in their Kon area).

Respectfully submitted,

Ken Witherly

President,

Condor Consulting, Inc.

April 23, 2021

11. REFERENCES

Ellis, R. G. 1998: Inversion of airborne electromagnetic data: Exploration Geophysics Vol 29, pp 121-127.

Farquharson, C.G. and Oldenburg, D.W. 1993: Inversion of time domain EM data for a horizontally layered earth, Geophysical Journal International, Vol. 114, pp 433-441.

Fiset, N., Orta, M. and Plastow, G. 2016: Report on a helicopter-borne versatile time domain electromagnetic (VTEM Plus) and horizontal magnetic gradiometer geophysical survey. Project: Klock and Firstbrook. Location Temagami, Ontario. For: Tri Origin Exploration. Survey Flown: January-February 2016. Project GL150279. Report by Geotech Ltd., March 2016.

Keating, P. 1995: A simple technique to identify magnetic anomalies due to kimberlite pipes. Exploration and Mining Geology, Vol. 4, No. 2, pp. 121-125, Canadian Institute of Mining, Metallurgy and Petroleum.

Ontario Ministry of Energy, Northern Development and Mines 2021: Mineral Deposit Inventory Database: https://www.geologyontario.mndm.gov.on.ca/MDI_Description.html

Power, M., Belcourt, G. and Rockel, E., 2004, Geophysical methods for kimberlite exploration in northern Canada, The Leading Edge, November 2004

Rudd, J. 2005, Report on a Helicopter-Borne AeroTEM II Electromagnetic & Magnetometer Survey, Lapointe Project, Aeroquest project 05002 for Tres-OR Resources Ltd. January, 2005.

Venter, N., Fiset, N., Orta, M. and Plastow, G. 2016: Report on a helicopter-borne versatile time domain electromagnetic (VTEM Plus) and horizontal magnetic gradiometer geophysical survey. Project: Brigstocke, Gilles West, Cassels North and Cassels South. Location Temagami, Ontario. For Tri Origin Exploration. Survey Flown: October 2015-January 2016. Project GL150279. Report by Geotech Ltd., March 2016.

APPENDIX A: KEATING 1995 PAPER



0964-1823(95)00002-X

A simple technique to identify magnetic anomalies due to kimberlite pipes

PIERRE KEATING

Geological Survey of Canada, 1 Observatory Crescent, Ottawa, Ontario, Canada, K1A 0Y3

Contribution from the Geological Survey of Canada 20794

Received June 27, 1994; accepted November 24, 1994.

Abstract — Most of the world's known kimberlites have distinctive geophysical signatures, generally magnetic and/or electromagnetic. In the Canadian Shield, their aeromagnetic signature is often that of a circular anomaly. Target selection from aeromagnetic data is, therefore, based on the identification of roughly circular anomalies. This procedure can be automated by using known pattern recognition techniques. One of them is to compute, over a moving window, a first-order regression between a typical model anomaly and the aeromagnetic data. Only the results where the absolute value of the correlation coefficient is above a certain threshold are retained. Other criteria are later used to further refine the selection. The locations of these solutions are then plotted on the aeromagnetic map and, if available, on a conductivity map. The Kirkland Lake region was selected to test the methodology and the proposed technique has been able to identify known kimberlites.

Résumé — La plupart des kimberlites connues dans le monde ont des signatures géophysiques particulières, en général magnétique et/ou électromagnétique. Dans le Bouclier canadien, leur signature magnétique est souvent une anomalie circulaire. La sélection de cibles à partir des données aéromagnétiques est donc basée sur l'identification d'anomalies plus ou moins circulaires. Cette procédure peut être automatisée à l'aide de techniques de reconnaissance de forme. L'une d'elle, est de calculer à l'intérieur d'une fenêtre mobile une régression du premier ordre entre le modèle d'une anomalie typique et les données aéromagnétiques. Seuls les résultats dont la valeur absolue du coefficient de corrélation est supérieure à un certain seuil sont conservés. D'autres critères sont par la suite utilisés pour raffiner la sélection. Les localisations de ces solutions sont alors tracées sur une carte aéromagnétique et, lorsqu'elle est disponible, sur une carte de conductivité. La région de Kirkland Lake a été choisie pour tester la méthodologie, et la technique proposée a pu identifier les kimberlites connues.

Introduction

Most of the world's known kimberlites, a major source of diamonds, have obvious geophysical signatures, generally magnetic and/or electromagnetic. Macnae (1979) reviews the various geophysical characteristics of kimberlites and presents simple interpretation models. The identification criteria that are suggested in South Africa: a bull's eye appearance on the contoured magnetic and/or EM data; the EM anomaly, if present, should appear to have a shallower source than the magnetic anomaly; either the magnetic or the EM anomaly should be of large amplitude; pipes tend to be clustered within a few kilometers; and there should be a coincident visible feature on aerial photographs. Brummer et al. (1992) show how aeromagnetic surveys have been able to successfully identify previously unknown kimberlites in the Kirkland Lake region in Northern Ontario; their approach was to look for small, isolated circular anomalies. Paterson et al. (1991) have used Euler deconvolution (Reid et al., 1990) of aeromagnetic data to select targets for kimberlite exploration.

Kimberlites are more or less circular in surface exposure. A typical pipe is carrot-shaped in cross section and its size

diminishes with increasing depth and changes to a kimberlite dike (Brummer et al., 1992). In the Canadian Shield, their aeromagnetic signature is that of a circular anomaly. However, at ground level, the anomaly is often more complex, it can be slightly elongated and even have internal highs. Typical examples are presented by Macnae (1979) and Brummer et al. (1992). Magnetic susceptibility can be variable, even within a single pipe. Remanence may be present or not; for instance, many of the kimberlites from the Northwest Territories have a reversed magnetization (Reed, 1993). Pipe dimensions vary; Macnae (1979) notes that in South Africa the apparent source dimension of the magnetic anomaly is in the range of 100 m to 1600 m. In the Kirkland Lake area, the diameter of the known kimberlite pipes is of a few hundred meters. Target selection from aeromagnetic data is, therefore, generally based on the identification of roughly circular anomalies.

Methodology

The primary selection of kimberlite locations can be done visually by inspection of the aeromagnetic map (Brummer

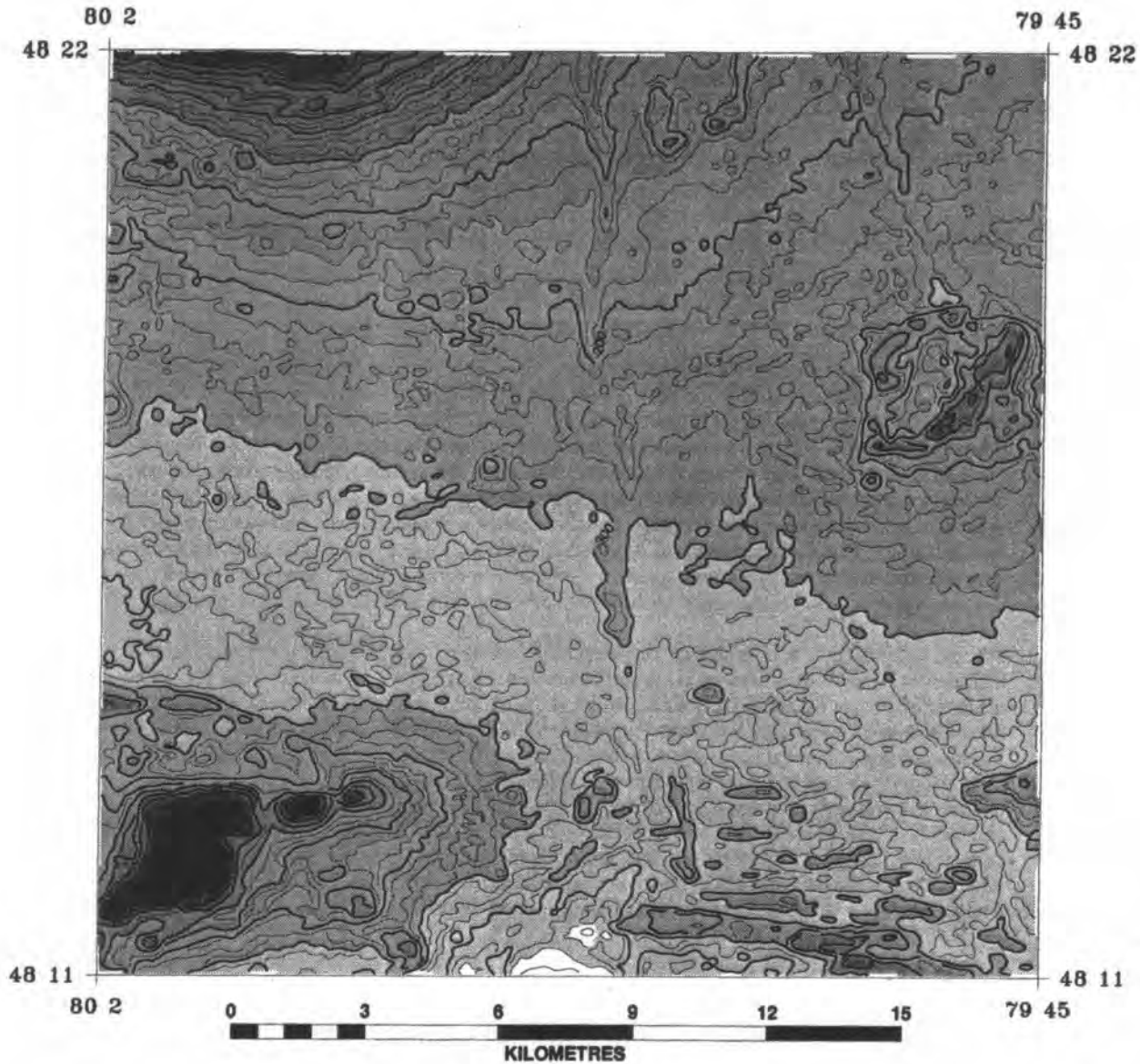


Fig. 1. Magnetic anomaly map.

et al., 1992) or, in an automated manner, by using Euler deconvolution as proposed by Paterson et al. (1991). A problem, not often mentioned, with the use of the latter technique is the great number of false targets obtained. Euler deconvolution is very sensitive to the local gradients of the magnetic field and tends to identify contacts between areas of different susceptibilities. The Euler structural index of 2.0, which corresponds to the vertical pipe model, also targets dikes where they are offset or truncated by faults. Here, the author proposes to use a simple pattern recognition technique to identify only those aeromagnetic anomalies that are caused by vertical pipe-shaped bodies.

The carrot shape of the kimberlite pipe suggests the use of a finite vertical cylinder as a model. In theory, a vertical pipe can be modelled by a vertical cylinder, a vertical dipole or, more simply, by a simple pole anomaly. It has been found that the best results are obtained with the vertical cylinder model, because simple poles or dipoles cannot ac-

count for the radius of the kimberlites. The magnetic anomaly caused by a vertical cylinder can be calculated by applying Poisson's relation to the gravity anomaly due to this geometry (Telford et al., 1990). The vertical component of the gravitational effect of a semi-infinite outcropping cylinder as derived by Nabighian (1962) is:

$$g = 2 G \sigma R \left(\frac{1 - x^2}{(1 + x)^2 + a^2} K + \sqrt{(1 + x)^2 + a^2} E + \frac{\pi}{2} a [A_0(\varphi, k) - 2] \right) \dots \dots \dots (1)$$

where

- G = universal constant of gravitation
- σ = density contrast
- R = radius of the cylinder
- x₀ = horizontal distance from the cylinder axis
- a₀ = depth to the top of the cylinder

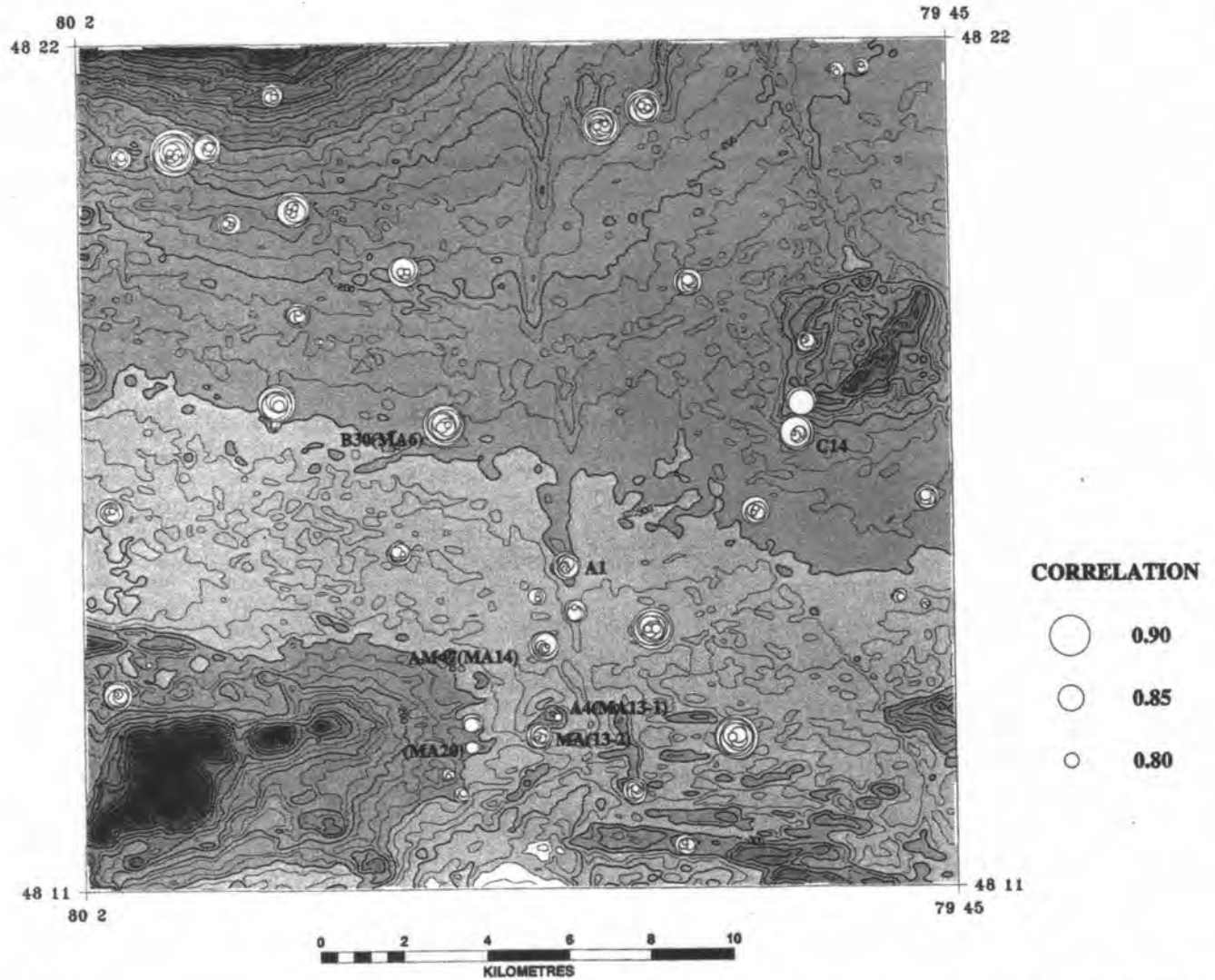


Fig. 2. Magnetic anomaly map. Location and numbering of the kimberlite pipes is from Figure 2 of Brummer et al. (1992). Circle diameter is proportional to the absolute correlation.

$$a = a_0/R$$

$$x = x_0/R$$

K and E are the complete elliptic integrals of the first and second kind with parameter k

$$k^2 = \frac{4x}{(1+x)^2 + a^2}$$

$\Lambda_0(\varphi, k)$ is Heuman's Lambda function with

$$\varphi = \arcsin \left(\frac{\alpha}{\sqrt{(1-x)^2 + a^2}} \right)$$

A numerical solution for equation (1) is given by Nagy (1965). The gravitational attraction of a finite cylinder is obtained by subtracting the effect of two coaxial semi-infinite cylinders separated by a vertical distance L. The magnetic anomaly is then easily calculated from Poisson's relation (Telford et al., 1990).

A theoretical model anomaly is first calculated, the depth to its top and its radius are selected to be the expected values of these parameters for the kimberlite pipes in the studied area. Different values can be tested. Pattern recognition consists of simply calculating a first-order regression between the model anomaly and the aeromagnetic data over a moving window (Davis, 1973). Regression results include the standard error of fit, the correlation coefficient, the student's test value and the scaling factor between the model and the observed data. Only the results that have an absolute value of the correlation coefficient above a certain threshold are retained. The standard error of fit of the regression is later used to further refine the selection of the targets. The locations of these solutions are then plotted on the aeromagnetic map and, if available, on a conductivity map.

Actual Results

The Kirkland Lake region was selected to test the methodology, as it is well documented. The data are from a com-

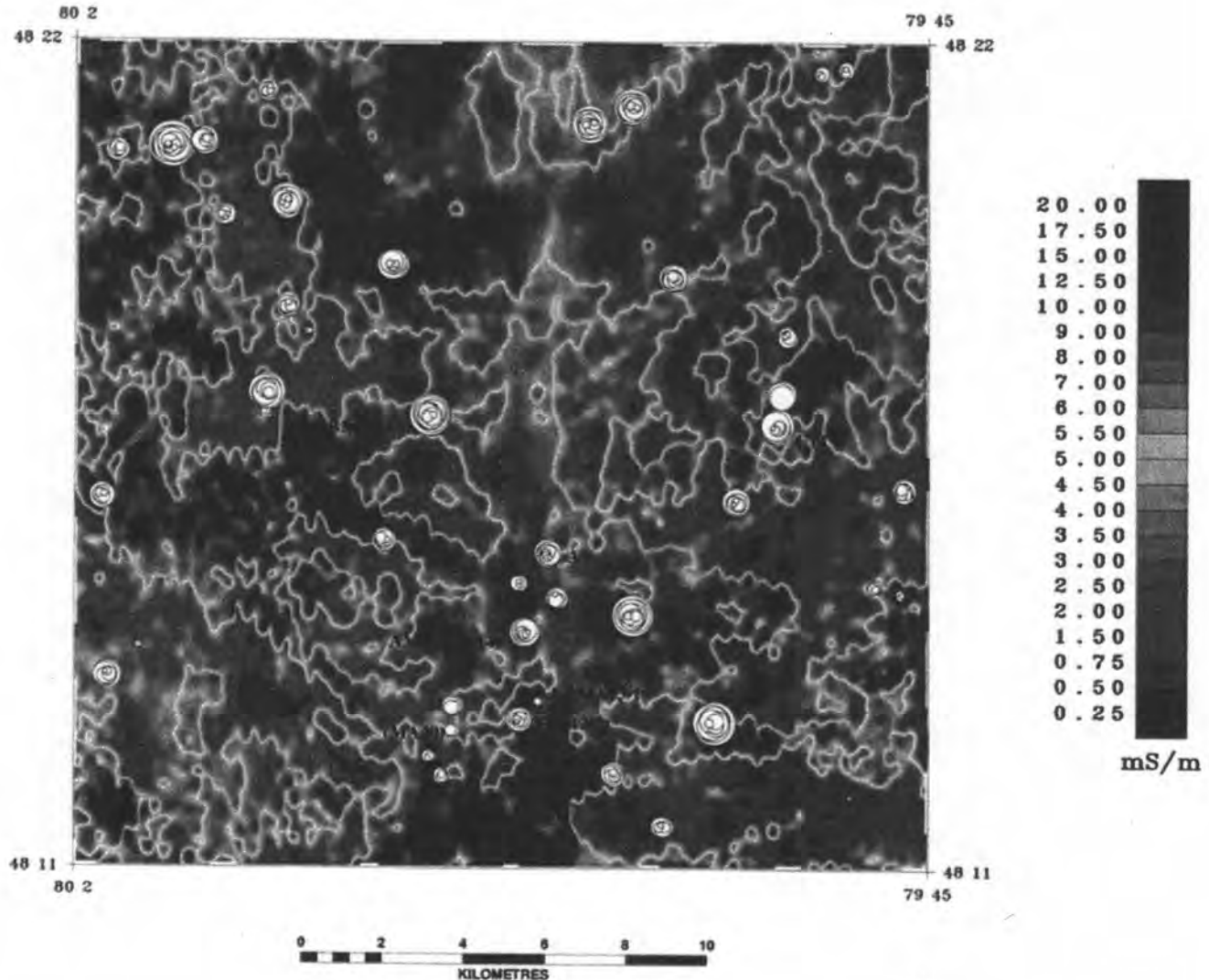


Fig. 3. Apparent overburden conductivity map. Location and numbering of the kimberlite pipes is from Figure 2 of Brummer et al. (1992). Circle diameter is proportional to the absolute correlation.

bined magnetic (Fig. 1) and electromagnetic survey flown as part of the Ontario-Canada Mineral Development Agreement (GSC, 1993). The test area is located north of Kirkland Lake in northeastern Ontario. Flight lines were oriented north-south and the magnetometer sensor was located at an average height of 70 m above ground. The EM data (time-domain EM) were also used to produce a conductivity map. A total of seven kimberlites (Fig. 2) are known in this area, which has been extensively studied (Brummer et al., 1992). Solutions with an absolute value of the correlation coefficient greater than 0.75 and a standard error of regression better than 75 nT are shown in Figure 1. In this case, the top of the pipes is assumed to be about 120 m under the magnetometer (depth of 50 m) and their radius to be 75 m.

Strong absolute correlations (>0.85) are found for most known kimberlites, except for MA 20 and MA 13-1 that have weaker absolute correlations, only slightly more than 0.75. This is because they are elongated ellipsoidal shaped anomalies, therefore departing from the circular model hypothesis.

Although, in theory, Euler deconvolution also provides depth information, the technique proposed here is more effective, because it accurately locates known kimberlites, while keeping the number of possible targets to a minimum. Euler deconvolution is based on the assumption that the equation of the magnetic or gravity anomaly for a given geometry is homogeneous. Although this is the case for a few simple shapes, it is not for more complex geometries.

Plotting the solutions on the overburden conductivity map (Fig. 3) improves target selection, because kimberlites often have a positive conductivity response. The increase in conductivity is due to the presence of near-surface conductive clays in the weathered kimberlite (Palacky, 1987). In the Kirkland Lake region, kimberlites documented by Brummer et al. (1992) are associated with an increase of the overburden thickness, likely caused by erosion of the weathered top of the pipe after the last glaciation. This results in a higher apparent conductivity. This criteria can be used to reduce the number of possible targets. All the known kimberlites in this region have a positive conductivity response.

Conclusions

A simple regression between the theoretical magnetic anomaly due to a vertical cylinder and the observed magnetic field within a moving window is an effective tool to identify magnetic anomalies caused by kimberlite pipes. The absolute value of the correlation coefficient and the standard error of fit of the regression are used to screen the possible targets. Plotting the solutions on a conductivity map of the studied area further improves the technique, because most kimberlites have a positive conductivity response.

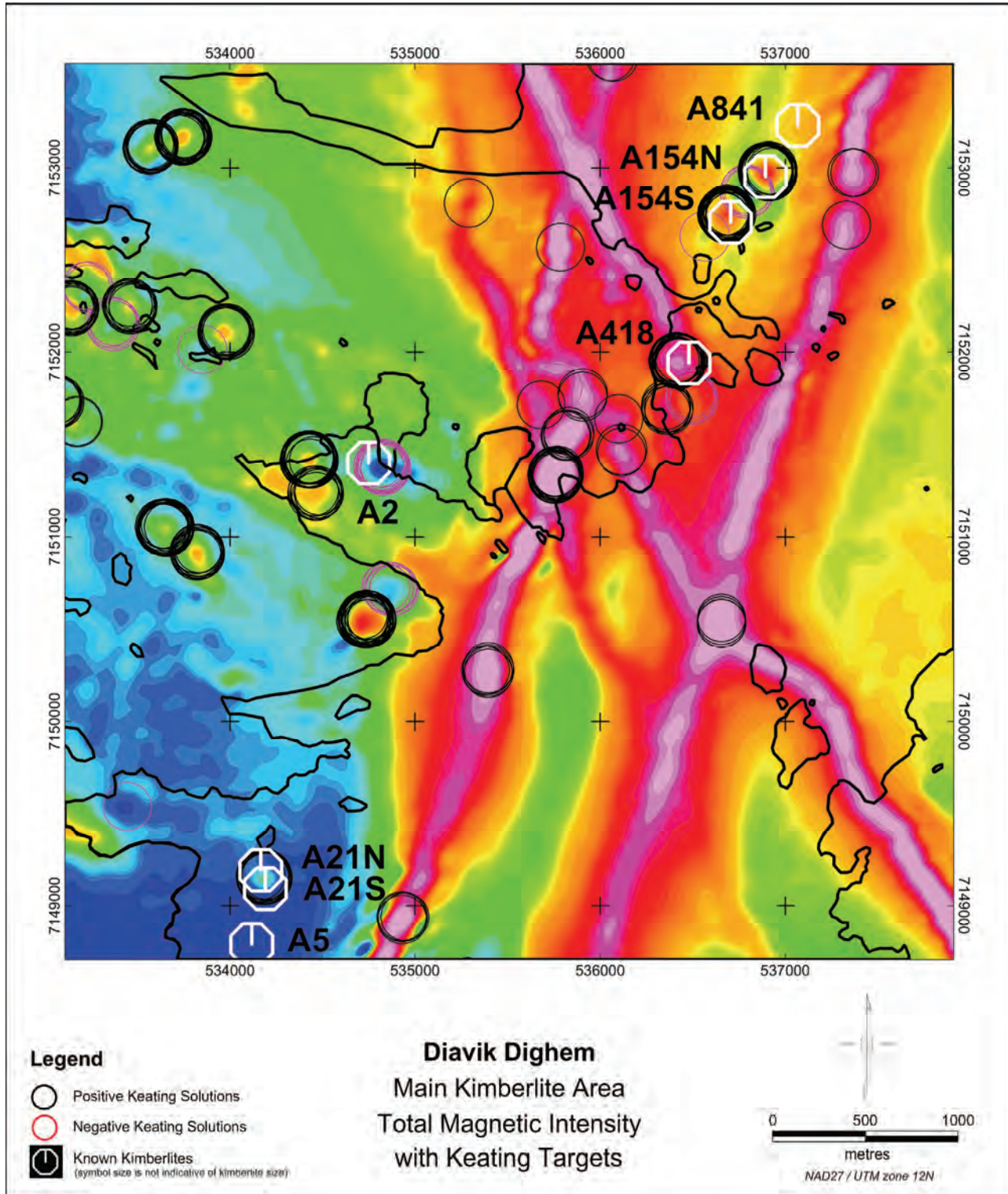
Acknowledgments

The author thanks his colleagues M. Pilkington and R.A.F. Grieve for suggesting improvements to the original manuscript and stimulating discussions. Thanks are also extended to Exploration and Mining Geology reviewer, Stefen Reford, for suggesting improvements to the manuscript.

References

- BRUMMER, J.J., MACFADYEN, D. A. and PEGG, C.C., 1992. Discovery of kimberlites in the Kirkland Lake area, Northern Ontario, Canada; Part II: Kimberlite discoveries, sampling, diamond content, ages and emplacement. *Exploration and Mining Geology*, 1, p. 351-370.
- DAVIS, J.C., 1973. *Statistics and data analysis in geology*. John Wiley & Sons, 550 p.
- GEOLOGICAL SURVEY OF CANADA, 1993. Aeromagnetic maps 20369G and 25056G.
- MACNAE, J.C., 1979. Kimberlites and exploration geophysics. *Geophysics*, 44, p. 1395-1416.
- NABIGHIAN, M.N., 1962. The gravitational attraction of a right rectangular cylinder at points external to it. *Geofis. Pura e Appl.*, 53, p. 45-51.
- NAGY, D., 1965. The evaluation of Heuman's Lamda function and its application to calculate the gravitational effect of a right circular cylinder. *Pure Appl. Geophys.*, 62, p. 3-12.
- PALACKY, G.J., 1987. Airborne electromagnetics, geological mapping, and prospecting for nontraditional targets. *In* Developments and applications of modern airborne electromagnetic surveys. *Edited by* D.V. Fitterman. U.S. Geological Survey Bulletin 1925.
- PATERSON, N.R., KWAN, K.C.H. and REFORD, S.W., 1991. Use of Euler deconvolution in recognizing magnetic anomalies of pipe-like bodies. Expanded Abstracts of the 61st Annual Meeting of the Society of Exploration Geophysicists, p. 642-645.
- REED, L.E., 1993. Exploration for kimberlites using magnetics. The Gange, GAC - Mineral Deposits Division Newsletter.
- REID, A.B., ALLSOP, J.M., GRANSER, H., MILLET, A.J. and SOMERTON, I.W., 1990. Magnetic interpretation in three dimensions using Euler deconvolution. *Geophysics*, 55, p. 80-91.
- TELFORD, W.M., GELDART, L.P. and SHERIFF, R.E., 1990. *Applied Geophysics*, Second edition, Cambridge University Press.

In 1997, the entire Diavik mine area was flown with the DIGHEM HEM system. A portion of these data over the main mine area were processed using the Keating matched filter technique; the image below shows the results. The known kimberlites are highlighted as are the Keating solutions, both positive and negative outcomes. All but one of the known kimberlites (A5) showed a corresponding Keating solution.



APPENDIX B: CONDOR TECHNICAL NOTE 2004-1

Condor Technical Note 2004-1

DEFINITION OF KIMBERLITE EM TARGETS USING THE KEATING MATCHED FILTERING METHOD.

INTRODUCTION

Kimberlites typically have circular or sub-circular horizontal cross sections and thus generate magnetic anomalies at high latitudes (or reduced-to-pole) that are also circular. Keating (1995) and Keating and Sailhac (2004) have developed matched filtering techniques that can be applied to gridded magnetic data to identify potential targets.

First, the magnetic response of a vertical cylinder (corresponding to the circular pipe) is calculated using the appropriate flying height, depth to top and diameter of the expected kimberlite. Then a simple pattern-recognition technique is applied, based on a first order regression over a moving window, between the observed magnetic field and the model magnetic field. Results where the correlation coefficient between the observed and model signal within the moving window are above a specified threshold are retained and additional criteria can later be used to refine the target selection.

The pattern recognition is general and can be applied to any pair of observed and theoretical responses. Condor has now applied this method to definition of kimberlite targets using DIGHEM and RESOLVE airborne EM data.

KIMBERLITE EM MODELS

The in-phase and quadrature responses of typical kimberlites have been calculated for frequencies typical of DIGHEM and RESOLVE airborne EM systems. This work was performed for Condor by Geophysical Algorithms (Peter Walker) and details are included as an attachment to this technical note.

The EM response of typical kimberlites is considered to be generated by either (or both):-

- (i) The relatively low conductivity of the crater phase (or weathering/oxidation) at the top of the kimberlite.
- (ii) The unweathered kimberlite having a relatively low resistivity, sufficient to generate a significant EM anomaly. However, the limited depth of penetration of airborne EM systems means that only the near-surface portion of any kimberlite will contribute to the EM response.

The conductive near-surface section of the kimberlite was modeled as a horizontal disk or “hockey puck”, with thickness of 50 meters and resistivity of 100 ohm-m. A series of models for a horizontal disk of diameters of 50, 100, 150 and 200 meters at distances of 25 m, 40 m and 55 m below a DIGHEM sensor were prepared. As the DIGHEM sensor is normally flown at approximately 25m above ground these distances correspond to 0 m, 15 m and 30 m below ground level.

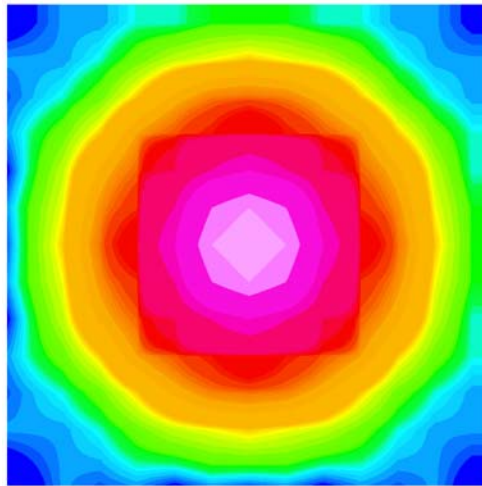
The frequencies used were:-

- Coplanar frequencies: 900, 7200, 56,000 Hz.
- Coaxial Frequencies: 900,5000 Hz.
- Coil spacing 8 m (except for 56K, which is 6.3 m.)

These are the normal frequencies used for a DIGHEM^V system. However, the modeling results can also be applied to similar frequencies in the RESOLVE system.

The results of the modeling are displayed as profiles of in-phase and quadrature in Appendix B.

The data for each frequency and component (in-phase and quadrature) have been gridded in order to be used in the Keating matched filtering. A typical grid is shown below, for 7000 Hz in-phase response of a 100m diameter disk with the top at surface.



APPLICATION

The Keating matched filtering is applied within the Oasis Montaj environment.

In northern Canada, the size of most diamondiferous kimberlites is between 50-200 m diameter, but of course is not known in advance. Although some kimberlites outcrop, many are buried beneath lakes and in the latter case the top of the conductive crater phase corresponds to the depth of the lake, which may be up to 30 m or deeper (if deeper, it is unlikely to produce a recognizable EM response on the DIGHEM or RESOLVE systems, because of the relatively rapid falloff in response with depth).

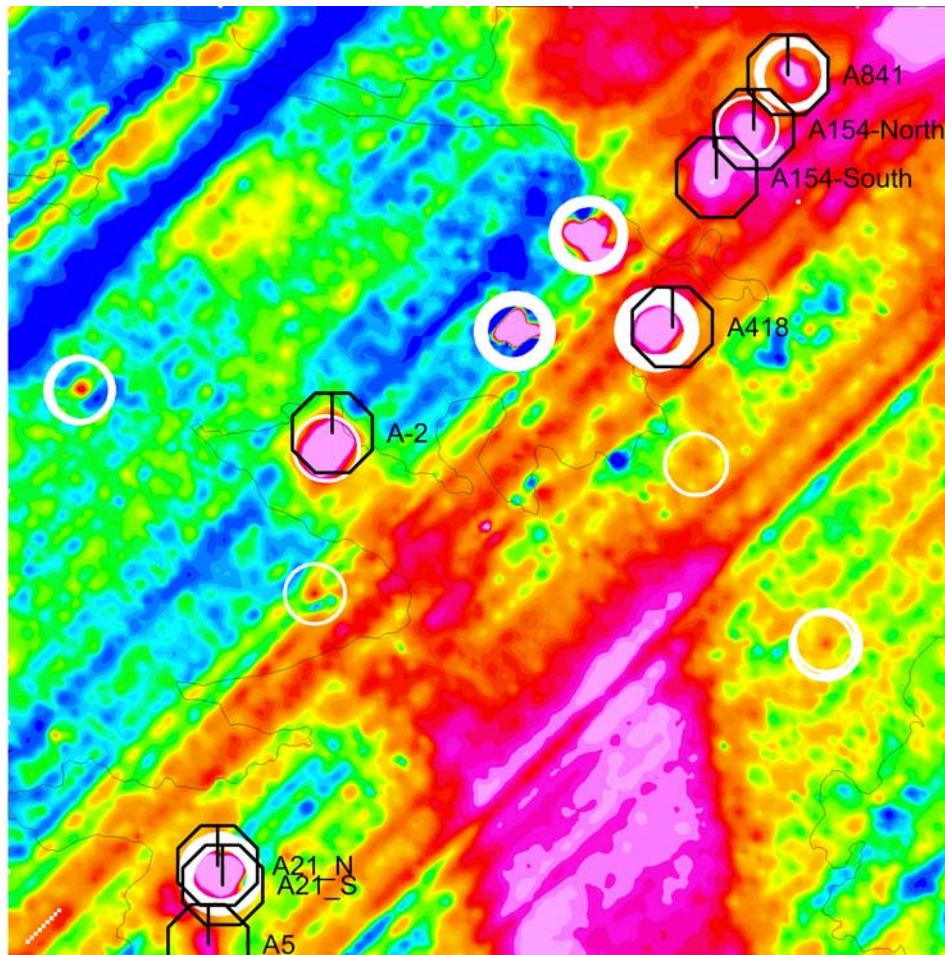
Therefore the matched filtering is carried out for all four diameters and all three depths, to maximize the chance of detection. Although the filtering can be applied to any or all of the data at the various frequencies and in-phase/quadrature components, normally (to reduce the processing to a manageable size) one frequency and one component are chosen

The Keating matched filtering generates an output file with X,Y locations of matching anomalies together with information on the correlation coefficients. These data are inspected and a suitable threshold value for the correlation coefficient is selected, so as to sift out anomalies that do not fit well to the theoretical model and thus reduce the data set to a manageable number of targets.

The final locations are then overlain on a suitable base map – typically an image of the observed data corresponding to the frequency and component used for the Keating processing, or an apparent resistivity image of the same frequency. One method is to plot circles with diameters related to the correlation coefficient (so that larger circles represent better correlations, which allows the actual anomalies to be seen. Different colors can be used for the different kimberlite diameters and/or the different depths, or alternatively the same color can be used for all Keating locations.

EXAMPLE

The method was applied to DIGHEM data flown over the Diavik area, NWT where a number of known kimberlites are located. The image below shows the 7200 Hz in-phase component, with the high values shown in red and low values in blue. The locations of the known kimberlites are indicated as black octagons, with the names annotated to the right. The Keating EM solutions are shown as white circles – these encompass all four diameters and three depths as described above.



Of the eight known kimberlites in the area shown, five correlate with Keating solutions. Kimberlites A21_N and A21_S are very close together and the Keating solutions are centered on the combined anomaly.

Kimberlites A154_South and A5 correlate with relatively strong anomalies on the 7200 Hz in-phase data, but the anomalies are significantly ovoid in shape and thus did not produce strong correlation coefficients in the matched filtering.

DISCUSSION

A limitation of this method is that it depends on kimberlites having circular, or near-circular cross sections. Other shapes could be accommodated during the modeling, but this would increase the number of models enormously in order to cater for a range of strike lengths and orientations and thus is not really feasible.

CONCLUSIONS

The Keating matched filtering method applied to airborne EM data is a useful additional tool in defining kimberlite targets in large airborne EM data sets. Human anomaly picking is flexible, but depends heavily on the experience of the interpreter and is inherently subjective. The Keating method has the advantage of being relatively fast and objective. In our experience it has delineated targets that we had not picked manually and so is very useful in adding to the thoroughness of the interpretation process.

However, the method is effectively limited to sub-circular anomalies and will not define targets that are distinctly ovoid or linear in shape. So the method is not a panacea, but rather an adjunct to manual picking of targets.

REFERENCES

Keating, P. (1995) A simple technique to identify magnetic anomalies due to kimberlite pipes. Exploration and Mining geology, Vol.4, No. 2, pp121-125.

Keating, P. and Sailhac, P. (2004) Use of analytic signal to identify magnetic anomalies due to kimberlite pipes. Geophysics, Vol 69, No. 1 pp 180-190.

Description of Dighem V Disk Modelling

May 21, 2004

Completed by P. Walker for K. Witherly of Condor Consulting

A series of models for a horizontal disk of diameters of 50, 100, 150 and 200 meters at depths of 25, 40 and 55 meters below a Dighem V¹ sensor have been prepared. The modeled body is described as a hockey puck with a thickness of 50 meters and a resistivity of 100 ohm-m. This was represented for the purposes of modeling as a thin sheet of conductance of 0.5 S.

The model results were prepared with Multiloop3, using a dimensional scaling factor of 100. The X, Y and Z coordinates of the output are therefore reports in units of 100 meters. The models were run using a scaled resistance of 0.02 ohms. The disk contained 401 nodes. For this number of nodes, the 200-meter disk would have an area of approximately 30000 m², and each basis function in this case would have an area of approximately 100 m², or a diameter of approximately 10-12 meters. The diameters of the basis functions on the other disks would be correspondingly smaller. This discretization interval is considered to be acceptable for all models completed.

As the model is symmetric about the two horizontal axis though the centre of the disk, profiles were run over ¼ of the disk. Line separation was 20 meters (.2 X 100 m) and point separation was 10 meters.

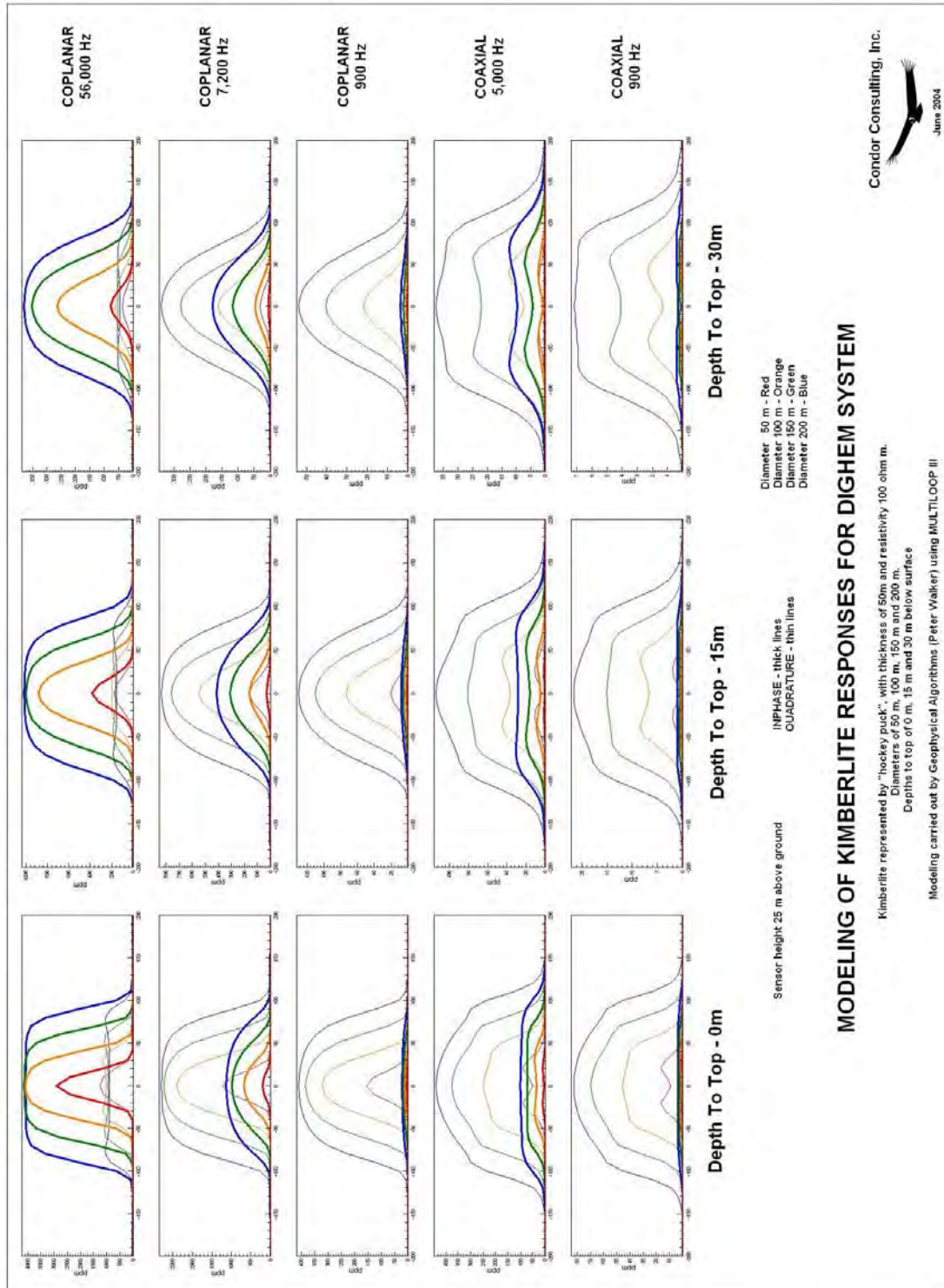
MultiLoop3 results were checked against VHPlate for the Dighem V system by comparing model results for a 100 by 100 meter, 100 S horizontal plate in free space. The results compared favourably.

Separate model runs were completed for each of the 3 coil geometries in the Dighem V system, and then merged into a single XYZ file for each disk diameter. The XYZ file data were then loaded into corresponding databases for delivery.

¹ The Dighem V system was represented as follows: Coplanar frequencies: 900, 7200, 56,000 Hz. Coaxial Frequencies: 900,5000 Hz. The coil spacing for all but the 56k is 8 m, the 56K is 6.3 m.

DISK MODELING

DIGHEM in-phase and quadrature profiles for different depths and diameters



APPENDIX C: MAG3D INVERSION NOTES/EM REFERENCE PAPERS

Inversion of Magnetic data for Tri Origin Exploration at the South Abitibi Project, Ontario, Canada, from the magnetic data stitch of 12 different data sets ranging from 50 m to 800 m spacing survey

The purpose of the inversion is to convert the measured nanoTesla data into a susceptibility model of the earth. The University of British Columbia (UBC) 3D magnetic inversion program, version 4.0, was used.

The inversions were performed with only the topography surface as a model constraint, along with the normal UBC-style objective function.

Area Inverted:

The area inverted was rectangular with the X and Y limits: 560 400 E, 607 000 E, 5 211 400 N, 5 263 800 N. All coordinates are NAD83 UTM Zone 17N. These units are in meters, which is required for the inversion. The area may not be completely saturated with data, leaving some portions of the inversion block without data. Areas of the model not covered with data are nulled in the final model.

Magnetic Data:

The data used came from the file: TriOrigin_Mag_Stitch_Final-PrPr1.grd which has a cell size of: 50 m.

A join by Condor Consulting of several grids.

Over the spatial extents of the windowed data, the regional trend (effects of sources outside the finite element mesh) was modeled as a 1st order surface (plane). The observed data, after regional removal, had a range of 31 243 nT. A simple 0th order shift was applied to ensure optimum positivity of the data so that the nominal model value is close to 0. No further preparation of the data was required.

A magnetic inclination of 72.6 degrees and declination of -11.3 degrees were used with a field strength of 55594 nT. The inversion model is not sensitive to small changes in the inducing field vector; changes over the span of the survey areas are inconsequential.

Topographic Data:

The topographic data came from the file: "TriOrigin_SRTM US Elevation 90m UTM17N.grd". The topography grid had a cell size of 77 m.

The topography had a range of 342 m over the inverted area.

Sensor Height:

A constant sensor height above the topography was used: 57 m. 35 m is the optimum EM sensor height for a VTEM survey, which is the source of one data set that contributed to the merge. The mag sensor would be 22 m above that (57 m above the ground).

Model Design:

The inversion area was split into 9 tiles with 3 in the easting, 3 in the northing.

The finite element mesh for the inversion tile employed a cell size of 100 m by 100 m, in the east and north dimensions respectively, and the cell height varied wrt depth. There were 156 cells in the easting, 175 in the northing. In the vertical direction, there are 14 air cells, each being 25 m thick and the ground cells started at 25 m thick and progressively increased in thickness through 30 vertical cells. In addition to the cells specified above, seven rim cells required by the finite

element algorithm were used on the sides of the mesh and six were added to the bottom. The depth of mesh, excluding bottom rim (finite element buffer layers) and air cells, was 3000 m. The initial error estimate provided to the inversion program was:

Tile 1) 15.85 nT
Tile 2) 28.03 nT
Tile 3) 13.60 nT
Tile 4) 2.77 nT
Tile 5) 8.21 nT
Tile 6) 9.76 nT
Tile 7) 2.42 nT
Tile 8) 6.20 nT
Tile 9) 8.10 nT

These errors were derived from 0.003 times the standard deviation of the data plus 0.500 times the average gradient between cells plus 0.010 nT.

Length scales (used in the inversion objective function) are 100 m in the horizontal and 50 m in the vertical directions. The sensitivity matrix was computed to a resolution of 0.025.

Inversion Results:

Two inversions were run, the first with a starting and reference model of 0.0 nT. The model from the first inversion was sharpened then used as the reference for the second inversion. This additional model sharpening procedure was performed to lessen the inherent smoothness of the models while retaining a good fit to the data.

The final inversion finished with a final data misfit average of 3.58 nT. The standard deviation of the misfits was 9.75 nT.

The voxel model was trimmed by 7 cells on the east and west, 7 cells on the north and south, and 6 cells from the bottom to remove the finite element buffer cells. The voxel model was further cleaned by nulling the voxels where there was no data.

The final merged model has 468 cells in the easting, 525 in the northing and 44 in the vertical. It covers an area that is 47 km by 53 km.

The model has a total of 8 321 770 cells. The model susceptibility ranges from -0.50200 to 1.95200 with a mean of 0.00323 SI. It should be noted that for this inversion the model was not restricted to positivity (doing so often leads to ringing in the model). Instead the modeled susceptibility values are allowed to be negative and are considered relative, not absolute values. Indeed, the amount of negative susceptibility values in the model is largely a function of the shift applied to the observed data (adding 100 nT to the observation data may reduce the number of negatives but can create undesired trends and edge effects in the model as well). It is also noted that in the case of remanence, the magnetization vector can be oriented in some direction other than the earth's inducing field. The UBC inversion allows the magnetization vector to only be in the same direction of the inducing field or in the opposite direction (manifested as negative values). Geosoft's MVI program, however, allows for the magnetization field to be in any direction (which is unconstrained and often ignored despite its significance) and the returned susceptibility is simply the length of that vector.

Presentation of the Models: The final model is delivered to the client in the native format of the UBC inversion in SI units. Although this format can be read by several geophysical packages, such as Geosoft, Encom PA and WinDisp (by Scientific Computing and Applications), it is unknown to many other visualization programs. If required, Condor Consulting can export the model

in the CSV format that, although bulky, can be imported by a greater number of programs such as Leapfrog.

Condor Consulting can make Geosoft formatted grid slices of the model through the nodes in the XZ, YZ and XY planes. In addition, Geotiffs can be produced for the grids in the XY planes and depth slices (draped beneath topography). For 3D visualization, 3D DXF files are often created from the models for a few isosurface values.

Smooth Model Inversion:

The SCA and UBC 3D susceptibility inversions are smooth model inversions, producing fuzzy objects in the resulting block model. This can be mitigated to some extent by sharpening techniques and by constraints. However, the model will still contain a large spatial uncertainty, which manifests as indistinct boundaries. Therefore, the density values in the model usually underestimate the actual density of the objects being imaged, since the density is smeared over a greater volume than the actual object.

Depth Weighting:

It is a well-known fact that magnetic data lack inherent depth resolution. A numerical consequence of this is that when an inversion is performed the resultant susceptibility is concentrated close to the observation locations. In order to overcome this, the inversion introduces a depth weighting to counteract this natural decay. The weighting approximately cancels the sensitivity decay and gives cells at different locations equal probability to enter into the solution with non-zero susceptibility. This weighting is approximately the depth of the finite element cell to the 2nd power, to counter a sensitivity drop of approximately $1/z^2$.

Inversion of airborne electromagnetic data

Robert G. Ellis

BHP Minerals,
1597 Cole Boulevard,
Suite 250,
Golden, CO 80401 USA.

ABSTRACT

Airborne electromagnetic geophysics is based on analysis of the interaction of an electromagnetic field with the geoelectric properties of the earth. Inversion, or inverse modelling, of airborne electromagnetic (AEM) data refers to a particular mathematical methodology for solving the AEM inverse problem, that is, deducing the earth's geoelectric properties from observed electromagnetic interactions. This is a difficult problem for several reasons. First, like most geophysical inverse problems, the AEM inverse problem with a finite number of noisy data is ill-posed, and consequently, the geoelectric properties of the earth cannot be uniquely determined. To generate a unique solution a priori information must be added to the inverse problem: a procedure referred to as regularisation. Second, since the geoelectric properties of the earth and the observed AEM data are not linearly related the inverse problem is nonlinear and requires solution by an iterative method. Third, the forward problem of calculating the response from a given geoelectric earth model, which is an essential part of the inverse problem, is itself a difficult and time consuming problem for 2.5D or 3D models. Fourth, AEM geophysics is characterised by enormous quantities of data. These difficulties and how they can be addressed are the focus of this paper. Particular emphasis is placed on the non-uniqueness of the AEM inverse problem and how it can be resolved through regularisation using a priori information. The applicability of 1D inversion in multi-dimensional environments and the advantages of multi-dimensional inversion are demonstrated, as is the potential value of joint inversion of AEM data and other geophysical data.

INTRODUCTION

Inversion or inverse modelling of airborne electromagnetic (AEM) data refers to a particular mathematical methodology for solving the AEM inverse problem. In the simplest of terms inversion refers to the process of finding a geoelectric model which has a predicted response in satisfactory agreement with given observed data. Usually the geoelectric model refers to a conductivity model, however, the general AEM response is also sensitive to other electrical properties of the earth: magnetic susceptibility, dielectric permittivity, and chargeability. The term AEM response generally refers to a measured magnetic field or its time derivative. Without significant loss of generality this paper focuses on the AEM inverse problem limited to conductivity models and time derivatives of the magnetic field response as would be measured in a typical coil-based acquisition system.

The solution of the AEM inverse problem is difficult for several reasons, some mathematical, and some specific to the nature of the AEM data itself. From the mathematical perspective the AEM inverse problem, like all geophysical inverse problems is ill-posed; that is, the geoelectric properties of the earth cannot be uniquely determined from a finite number of noisy AEM data. This is by far the most

significant issue for the geoscientist and is the primary focus of this paper. Furthermore, it is necessary to further constrain the AEM inverse problem by adding *a priori* information, which is simply auxiliary information that the geoscientist incorporates to help solve the inversion problem. This external information can come from a wide variety of sources; for example, from the interpretation of other geophysical surveys, from knowledge of the local geology, from drill logs, or if all else fails, from a mathematical statement of ignorance. The addition of a priori information is said to regularise the inverse problem. It must be emphasised that the difference between a valuable inversion and a worthless inversion often rests on the quality of the a priori information used in the solution.

A second mathematical difficulty with the AEM inverse problem is the non-linear relationship between the geoelectric properties of the earth and the resulting observed AEM data, as embodied in Maxwell's equations. This is in sharp contrast to the simpler gravity and magnetics inverse problems. Consequently, a numerically intensive iterative method of solution must be employed. Numerical difficulties are exacerbated by the forward AEM problem of calculating the response from a given geoelectric earth model, itself a difficult and time consuming problem for 2.5D or 3D models.

The feature most specific to the AEM method, when compared to other electromagnetic geophysical methods, is the enormous quantities of data that are produced from an AEM survey. Modern airborne surveys may well contain tens of thousands of line kilometres of multi-channel data sampled every tens of meters. These vast quantities of data have resulted in the majority of AEM inversions assuming a one-dimensional earth model. However, with increasing computer power, and the fact that the earth is often heterogeneous, interest is turning to higher dimensional models. Other specific issues related to the AEM method include the band-limited time window in which measurements can be made on a moving platform, the limited target angular coverage or footprint, and a host of motion noise issues related to airborne platforms.

MATHEMATICS OF INVERSE MODELLING

In the most general terms, airborne inverse modelling simply refers to the process of finding a conductivity model, $\sigma(x)$, which has a predicted EM response, $H_i^{\text{pred}}[\sigma]$, in satisfactory agreement with N observed data, H_i^{obs} . Inevitably the observed data have associated errors, δH_i^{obs} ,

and knowledge of these errors permits a mathematical statement of satisfactory agreement: the χ^2 misfit should be approximately equal to the number of data for Gaussian errors. The inverse problem can then be written,

$$\text{Find } \sigma(\mathbf{x}) \text{ such that } \chi^2 = \sum_{i=1}^N \left(\frac{H_i^{\text{obs}} - H_i^{\text{pred}}[\sigma]}{\delta H_i^{\text{obs}}} \right)^2 \sim N \quad (1)$$

This simple description of inverse modelling conveys the essence of problem, however, it completely masks the complexity and beauty of the problem, and, certainly does an injustice to the vast literature on this subject. For the geoscientist the most challenging aspect of equation (1) is the fact that there are infinitely many solutions. This non-uniqueness is a symptomatic of equation (1) being an ill-posed inverse problem.

Ill-posed Inverse Problems

When an inverse problem is described as ill-posed it means that one or more of the three conditions required by a well-posed inverse problem are not satisfied. These conditions are: a solution must exist, the solution must be unique, and the solution must be stable. To clarify these conditions let us consider a simple inverse problem: given 14 channels of time domain fixed wing AEM data (the "observed" data), find a layered earth model (the "recovered" model) which fits the data. For the purpose of this example, the transmitter current is taken to be a 25 Hz, 4 ms half-sine pulse. The measured channel times and widths are consistent with typical AEM acquisition systems, ranging from 1 ms to 15 ms after the end of the 4 ms pulse. The transmitter is assumed to be a horizontal loop and only the response from the vertical axis receiver coil is considered. The observed data are shown in the lower part of Figure 1 as points with, for demonstration purposes, a 2% error bar. We now demonstrate why this problem is ill-posed by first examining the non-uniqueness of solutions to equation (1)

Non-uniqueness refers to the situation where more than a single model gives rise to the same response. This is illustrated in Figure 1 where three conductivity models are shown, all of which give rise to a response in agreement with the observed data to within 2% RMS error. The upper model in Figure 1 is a three-layer model, the middle model is a five-layer model, and the lower model is smooth, and there are infinitely many other models which have responses which fit the observed data. Clearly there can be a significant difference between these recovered models, and quite likely in any interpretation based on these different inversion results. Such a situation is well known in EM geophysics and has given rise to the general rule of thumb that only the conductivity thickness product, or conductance, can be determined from an EM measurement. While perhaps useful in certain cases, this statement is overly simplistic and often excessively reduces the credibility of the result of an inversion.

Having demonstrated that equation (1) does not specify a unique solution is sufficient to prove that the EM inverse problem is ill-posed. It is also found that the solution to equation (1) is unstable. Instability refers to the situation where small changes in the initial or boundary conditions on the inverse problem lead to large changes in the solution. In the AEM inverse problem instability is most likely to manifest itself as sensitivity of the recovered conductivity model to errors in the observed data.

The question of existence of a solution to equation (1) is less of an issue for practical AEM inversion, except in the sense that the model used to represent the true geoelectric model may be inappropriate. For example, if an AEM decay

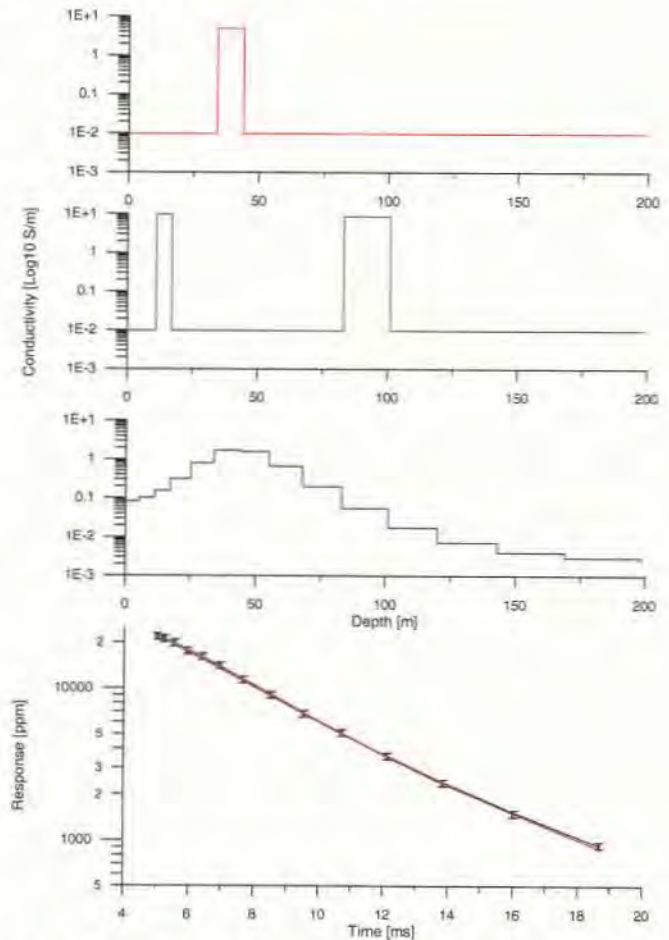


Figure 1. Three solutions for the inverse problem for a synthetic layered-earth model illustrate the concept of non-uniqueness in fixed-wing AEM data. The bottom graph shows the observed response in ppm as points with error bars plotted against time after the onset of the half-sine pulse. The upper three graphs show three conductivity models plotted as \log_{10} conductivity against depth. The predicted responses from the three conductivity models are shown in the lower graph in the corresponding colour.

curve has been measured or synthesised over a strongly 2D or 3D earth it is possible that the decay curve may change sign, a situation for which there is no layered earth solution. Another possibility is that the measured response may result from variation in susceptibility and the inverse model may only consider conductivity as a variable.

Different Approaches to the Inverse Problem

As we have seen in the preceding section, the AEM inverse problem, stated simply as the process of finding a model which has a predicted response in satisfactory agreement with some given data, is ill-posed. Rather than dismiss the problem as intractable, and in light of the fact that some albeit limited and ambiguous information about the electrical properties of the earth are hidden in the measured AEM response, considerable effort has been directed toward extracting information from fundamentally ill-posed inverse problems. These efforts have resulted in several ways to approach an ill-posed inverse problem, the simplest being to solve the construction problem.

The construction approach is to construct a specific type of model that has a predicted response in satisfactory agreement with the observed data. It is the most common technique applied to geophysical inverse problems in industry because it is computationally efficient and provides the interpreter with one or more models from a geophysical

survey. The essence of construction is to add extra information to the inverse problem before attempting a solution, a process that is often referred to as regularisation of the inverse problem (Tikhonov 1977). Methods of adding the requisite extra information needed for model construction can be grouped into three general categories (Menke 1984). The first category, the *model norm method*, is as simple as choosing, from the infinity of models which satisfies the constraint imposed by satisfactorily fitting the observed data, that model which also satisfies the auxiliary condition of minimising a predefined norm of the model. Such model norms are usually chosen on the basis of geological acceptability or on the basis of a mathematical condition such as minimum curvature. The second category, the *averaging function method* (Backus 1965), relies on minimising a combination of the Backus-Gilbert spread function and the covariance of the solution. The third method, the *probability or maximum likelihood method* (Tarantola 1982) reformulates the ill-posed inverse problem as a combination of information problem. In this case the inverse problem is formulated in terms of probability density functions for the data and model parameters, rather than in terms of single quantities such as the bounds or means of the model. Probability theory methods are used to solve the inverse problem, yielding those model parameters that maximise the probability that the observed data were in fact observed. Each of these three methods has its devotees, and with acknowledgment that in theory each method has its unique properties and insights, in practice there can also be a certain similarity between the resulting solutions, as discussed by Menke (1984, p. 95). In the spirit of this similarity only the model norm method will be considered in this paper.

While construction is the most common approach to the geophysical inverse problem it is far from the only approach to extracting information from an ill-posed inverse problem. For example, the appraisal method of Backus and Gilbert (1967) relies, not on adding prior information to render the problem well-posed but, instead, determines which model parameters, or combination of model parameters, are actually uniquely determined by the observed data. This approach is often referred to as Backus-Gilbert appraisal. The result of appraisal gives unique information satisfied by all models that reproduce the observed data. However, those same unique results are often of little practical use being either too vague or of little relevance since the geophysicist has no control, except in survey design, over which combinations of parameters are uniquely determined. Consequently, Backus (1970) developed the method of inference where the inverse problem is posed as: given observed data which are functionals of the model, what can be inferred about other functionals of the model where the latter functionals are defined by the geophysicist. This approach has seen some interesting further development toward the estimation of global bounds on model parameters in the work of Parker (1974), Oldenburg (1983), Fullager (1984) and Dosso (1989), however these methods are not commonly used in practice due to their computational burden.

To proceed further with the construction problem associated with equation (1) extra information must be added to distinguish between the infinite number of possible solutions. This extra information is termed a priori information and must be added to regularise the inverse problem. A priori information can come in many forms, for example, from geological considerations, from the interpretation or inversion other geophysical surveys, from drill hole information, or from a mathematical assumption such as finding a minimum norm model. The motivation for

the latter regularisation is the appealing principle that in the absence of constraint from the data, the solution to equation (1) should be in some sense recognisably "simple". Here "simple" is taken to mean the recovered solution has structure only where structure is imposed by the data and otherwise minimises a norm of the model. Mathematically this is achieved by modifying equation (1) to

$$\begin{aligned} &\text{Find } \sigma(x) \text{ to minimize } \Phi(\sigma) = \|W(\sigma - \sigma^{\text{ref}})\|^2 \\ &\text{subject to the constraint that } \chi^2 = \sum_{i=1}^N \left(\frac{H_i^{\text{obs}} - H_i^{\text{mod}}[\sigma]}{\delta H_i^{\text{obs}}} \right)^2 \sim N \end{aligned} \quad (2)$$

where W is an operator on the model σ returning, for example, the curvature of the model, or the global variation of the model, or any other measure of the model which satisfies the properties of being a proper norm. A reference model σ^{ref} is often included to give further flexibility in controlling the recovered model. Equation (2) is a constrained optimisation problem and it is usual, for the purposes of numerical simplicity, to convert to an unconstrained optimisation problem using the method of Lagrange multipliers. The resulting non-linear optimisation problem becomes,

$$\begin{aligned} &\text{Find } \sigma(x) \text{ to minimize } \Phi(\sigma) = \|W(\sigma - \sigma^{\text{ref}})\|^2 + \mu \sum_{i=1}^N \left(\frac{H_i^{\text{obs}} - H_i^{\text{mod}}[\sigma]}{\delta H_i^{\text{obs}}} \right)^2 \\ &\text{choosing } \mu \text{ such that } \chi^2 = \sum_{i=1}^N \left(\frac{H_i^{\text{obs}} - H_i^{\text{mod}}[\sigma]}{\delta H_i^{\text{obs}}} \right)^2 \sim N \end{aligned} \quad (3)$$

The trade-off parameter μ can be found by trial and error or by a line search algorithm. Proper choice of μ and W regularises the inverse problem and, together with σ^{ref} , control the otherwise arbitrary character of the solution to the inverse problem. The importance of this regularisation can be appreciated from the solutions shown in Figure 1 since it is only the choice of regularisation that determines which of those solutions will be produced by a particular algorithm: the lower model was produced by minimising the L2 norm of the model; the upper model was produced by minimising the L1 norm of the variation of the model; and, the middle model used the L1 norm of the model variation together with a five-layer reference model.

AEM INVERSION IN 1D

A full 3D solution to the AEM inverse problem is currently beyond the practical capabilities of all but the most powerful parallel processor computers so that in practice certain compromises must be made. One of today's popular compromises, motivated mainly by current computing capacity, is to restrict the class of inverse models to be 1D under each measurement point and then to stitch the individual inversion results together along a profile. Such an approximation is expected to give reliable results in relatively flat-lying geology, however, it might be expected to fail to some unknown extent in more complicated geology. The following examples addresses the degree to which such failure affects the interpretation of stitched 1D inversions.

The first model considered consists of a 100 Ωm uniform host with a 20 Ωm overburden of finite extent, shown in the lower part of Figure 2. All the images and results shown in this section will be drawn from a single profile through the middle of the 500m side of the overburden. The airborne system is chosen to simulate a typical fixed wing TEM system using a 25 Hz 4 ms half-sine transmitter pulse and a towed bird measuring the z-component of the derivative of the magnetic field approximately 120m behind and 40m below the transmitter. The observed (simulated) airborne

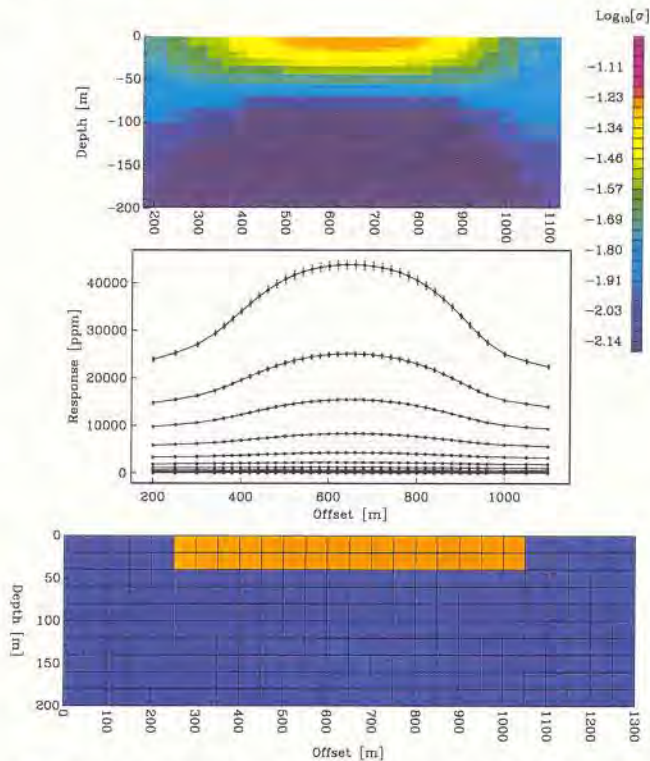


Figure 2. Stitched 1D inversion over a 3D conductive block. A section through the true conductivity model used to generate the data to be inverted is shown in the lower panel. The true conductivity model consists of a $100 \Omega\text{m}$ uniform host with a finite area of $20 \Omega\text{m}$ overburden. The overburden is $800\text{m} \times 500\text{m}$ in area and 40m thick. The data to be inverted are shown in the middle panel as points with error bars. The upper panel shows the recovered 1D inversions stitched to form a 2D section. The side colour bar gives the model conductivities in \log_{10} S/m. The predicted response from the recovered model is plotted as solid lines in the middle panel, fits the observed 1-D data very well.

TEM data plotted as points with a 2% RMS error bar in the middle panel of Figure 2. Applying the methods described above, a 1D smooth model inversion has been performed for each decay and the result is stitched into the 2D section shown in the upper panel of Figure 2. The 1D predicted response from the stitched section is shown in the middle panel plotted as lines over the error bars. For each 1D inversion the fit to the observed data is better than 2%. It will be noticed that over the centre of the overburden the 1D inversion does a good job of recovering the local character of the true overburden, however, it is significantly distorted near the edges of the overburden as might be expected. Perhaps less expected is that the forward response from the 1D model can very accurately simulate the observed 3D response of the true model. This demonstrates an important conclusion: the degree to which a 1D response fits the observed data cannot be used as an indicator that the true model is in fact 1D in vicinity of the observation.

The second model considered is an extension of the previous model in which a $1\Omega\text{m}$ target conductor, with dimensions $100\text{m} \times 500\text{m} \times 80\text{m}$, is buried below the overburden as shown in Figure 3, lower panel. The predicted response is shown in the middle panel as points with 2% error bars and demonstrates the characteristic minima associated with a horizontal loop airborne configuration passing over a vertical target. Again 1D inversions have been stitched to form the recovered model shown in the top panel. It is obvious that there is no direct indication of the target conductor in the stitched 1D section.

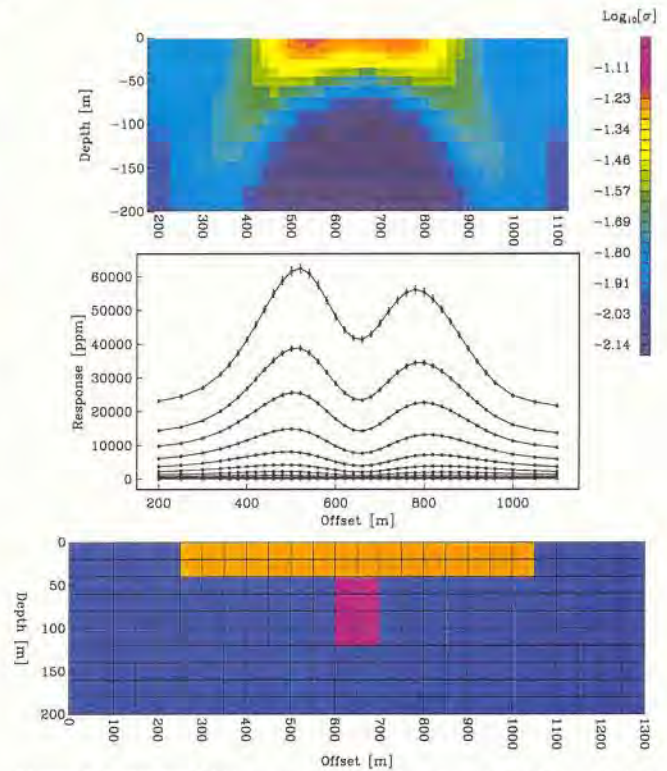


Figure 3. A stitched 1D inversion over the same model as Figure 2, but with the addition of a $1 \Omega\text{m}$ target conductor, with dimensions $100\text{m} \times 500\text{m} \times 80\text{m}$, buried beneath the overburden. The data to be inverted are shown in the middle panel as points with error bars. The upper panel shows the recovered 1D inversions stitched to form a 2D section. The predicted response from the recovered model is plotted as solid lines in the middle panel. The buried target is not resolved by the 1D inversion.

However, notice again that the predicted 1D responses fit the observed data to significantly better than the 2% error bars, reinforcing the conclusions that the goodness of fit to the data cannot be used to infer the geoelectric one dimensionality of the local vicinity, nor can it be used to infer any relationship between the stitched 1D model and the true model.

AEM INVERSION IN 2.5D

The limitations of 1D inversion of AEM electromagnetic data demonstrated in the preceding section are a strong motivation for inversion in two or three dimensions. Figure 4 shows an example of an inversion result using a 2.5D inversion over the model shown in Figure 3. The 2.5D inversion result clearly resolves the target conductor and provides a much greater similarity to the true model than the stitched 1D sections. The inversion algorithm used in this example was based on the inversion methodology developed by the University of British Columbia Joint and Cooperative Inversion Consortium (Ellis, 1994) and AEM modelling software developed by the University of Utah Consortium for Electromagnetic Modelling and Inversion (Xiong, 1992).

JOINT INVERSION OF AEM DATA

The success of AEM inversions in two and three dimensions is certainly a major step forward. However, expectations must be tempered by the realisation that non-uniqueness is as prevalent in higher dimensions as it is in one dimension. Consequently regularisation is still an important part of the multi-dimensional AEM inverse problem and has a major effect on the character of the

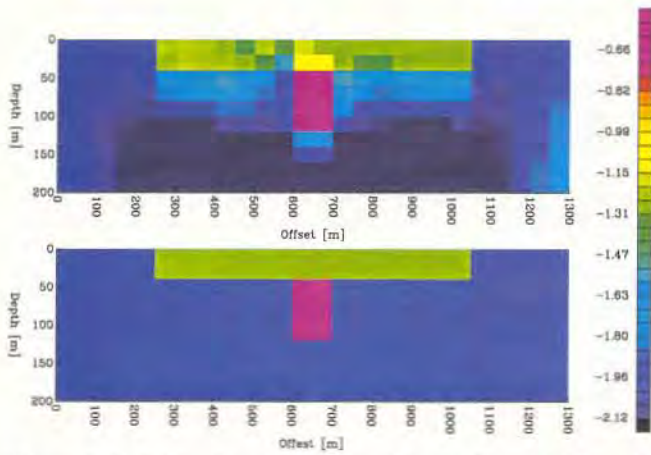


Figure 4. 2.5D inversion of the same data as shown in Figure 3 demonstrates recovery of the target conductor.

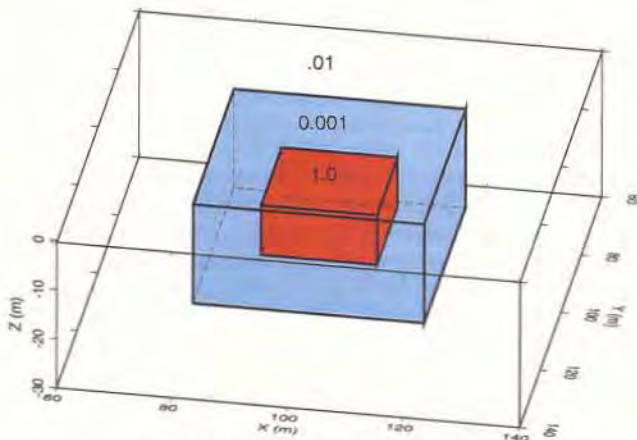


Figure 5. A 3D perspective view of the model used to simulate data for the joint inversion of helicopter AEM and DC resistivity data. The model consists of a conducting 1 Ωm prism buried inside a larger 1000 Ωm all buried in a 100 Ωm host.

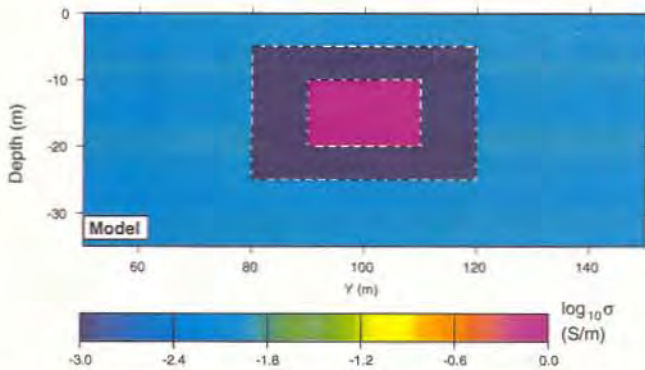


Figure 6. A section of the conductivity model of Figure 5 at $x = 95\text{m}$.

recovered model. Rather than exploring the effects of different regularisations in detail it would seem to be more advantageous to examine the possibility of reducing non-uniqueness by the introduction of information from other geophysical methods. Such information can be included by forming a larger inverse problem in a process referred to as joint inversion. The details of this approach has been presented elsewhere (Ellis 1995) for the case of joint inversion of frequency domain AEM data (H^{obs}) and DC resistivity data (V^{obs}). The joint inverse problem can be formulated as

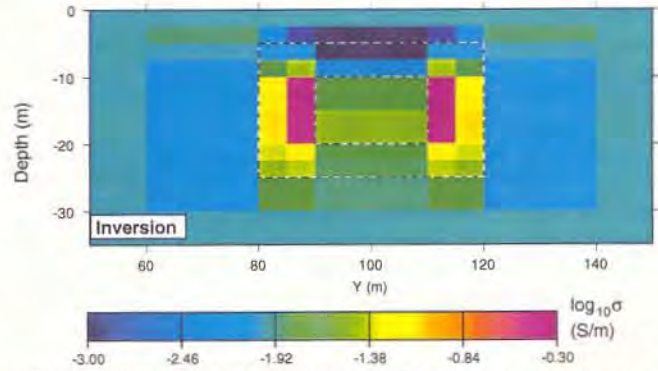


Figure 7. The conductivity model recovered from independent inversion of AEM data.

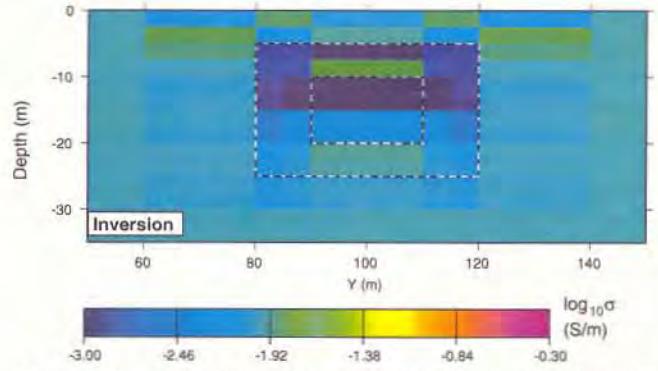


Figure 8. The conductivity model recovered from independent inversion of DC data.

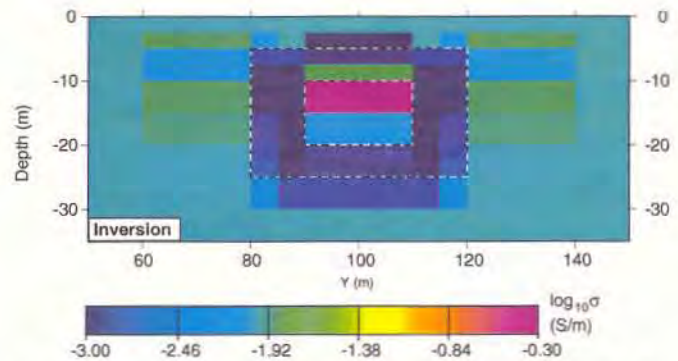


Figure 9. The conductivity model recovered from joint inversion of AEM data and DC resistivity data.

$$\text{Minimize } \Phi(\sigma) = \|W(\sigma - \sigma^{ref})\|^2 + \mu_1 \sum_{i=1}^N \left(\frac{H_i^{obs} - H_i^{mod}(\sigma)}{\delta H_i^{obs}} \right)^2 + \mu_2 \sum_{j=1}^M \left(\frac{V_j^{obs} - V_j^{mod}(\sigma)}{\delta V_j^{obs}} \right)^2 \quad (4)$$

where the optimisation problem of equation (2) has been augmented by a third term representing the χ^2 DC resistivity data misfit. The method of solution remains unchanged except for the addition of a second trade-off parameter, μ^2 . To demonstrate the effectiveness of joint inversion consider a geotechnically motivated model consisting of a conducting 1Ωm prism buried inside a larger 1000 Ωm prism all buried in a 100 Ωm host as shown in Figure 5. A single 28 kHz frequency domain helicopter survey, consisting of 8 flight lines 70 m in length and spaced 10 m apart, was simulated over this model. In the spirit of conciseness the results summarised here will show sections through the model only at $x=95\text{m}$. Figure 6 shows the true model section, Figure 7 shows the result of inverting the AEM data

alone, and Figure 8 shows the result of inverting the DC resistivity data alone. Figure 9 shows the result of inverting the AEM and DC data jointly via equation (4). This example shows that the combination of the AEM data, dominated by the inductive response, and the DC resistivity data dominated by the galvanic response, provides a significantly better image of the true model than either does independently. It is reasonable to generalise this result to the expectation that joint inversion of complementary geophysical data is important in reducing the effects on non-uniqueness inherent in the inversion of independent data.

IMAGING AND OTHER APPROACHES

Inverse modelling is necessarily an iterative process for AEM data because equation (2) is non-linear with respect to σ . This iterative process is conventionally derived from the first term in the Taylor series expansion of equation (2). At each iteration a solution is constructed which reduces the value of $\Phi(\sigma)$ compared to the previous iteration, and the process continues until convergence is reached. The iterative process can be terminated at any stage, even after at the first iteration. For example, an operator could be applied once to the data to generate an approximate image of the model. In the case of inverse modelling the imaging operator is based on a mathematical linearisation of the AEM forward modelling process; however, an infinity of other possibilities for the imaging operator exist. Indeed, considerable effort has been spent devising improved imaging operators with the aim of generating a geoelectric image of the earth without the necessity for the complexity and computation effort of a full multi-dimensional inversion (see for example Wolfgram, 1995, and Liu, 1993). Recent progress in this area has been made by Christensen (1997) using an 2D adaptive Born approximation with some success in removing artefacts associated with stitched 1D inversion. Progress has also been made by Zhdanov et al. (1995) on fast 2D resistivity imaging using time domain electromagnetic migration, a method which is based on downward extrapolation of the observed EM field in reverse time.

Just as iteration is used in the conventional inverse problem, it can also be applied to an imaging operator to enhance the accuracy of the image. Some progress has been made on formalising the process of iterating imaging operators (Oldenburg, 1991) with success in the MT and DC resistivity (Li, 1998) inverse problems. The philosophy and motivation behind the imaging operator approach is that they may work better than mathematically motivated operators if the physics of the problem can be embedded in the imaging operator more effectively than mathematical linearisation.

Another approach to inverse modelling relies on discrete models. These models attempt to describe the geoelectric properties of the earth in a small number of parameters. For example, algorithms have also been developed to solve the 1D layered earth inverse problem to determine the properties of a few layers of variable thickness, or as thin plates of finite conductance and infinite extension. Algorithms also exist for inversion of multi-dimensional AEM data which find the properties of a buried plate of finite extension and variable dip, strike, plunge, location and conductance (Macnae et al., 1998). These discrete models have the advantage of having only a few parameters, however, AEM data usually depend on those parameters in a very non-linear manner making solution of the inverse modelling problem based on discrete models more difficult than expected.

CONCLUSIONS

Inversion of AEM data is a difficult problem, principally because given a finite number of noisy AEM data there are infinitely many geoelectric models which have a predicted response that is in agreement with the given data to within noise levels. This situation has been clearly demonstrated for the layered earth inversion of typical fixed wing AEM data. To resolve this non-uniqueness a priori information must be added to the inverse problem, a process referred to as regularisation. Inversion results using L1 and L2 minimum structure models demonstrate the dramatic effect which a priori information can have on the AEM inverse problem solution.

Most AEM inversion to date has focussed on using a 1D model plotted under each measurement location. In the situation where the geology is relatively flat lying such an approximation will yield meaningful results. However, when the geoelectric properties of earth are significantly heterogeneous, a 1D assumption can lead to seriously inaccurate models. It is important to note that the degree to which the response of a 1D model can reproduce the observed data is no indication of the one-dimensionality of the local geoelectrical model, nor can it be used to infer any relationship between the stitched 1D responses and the true geoelectric earth.

Multi-dimensional inversion of AEM data is in its infancy, however, the confluence of more powerful desktop computers, improved inversion algorithms, and the knowledge that important discoveries may be overlooked by 1D inversion, are a powerful incentive in this area. A comparison of the results of a stitched 1D and a 2.5D inversion over the same model demonstrate the importance of multi-dimensional inversion.

There are a wide variety of methods for regularising the ill-posed AEM inverse problem. Each method requires the introduction of a priori information to choose a unique solution from the infinity of possible solutions with a satisfactory predicted response. A priori information can be introduced from many sources, for example from geological constraints, from the inversion and interpretation of other geophysical surveys, or from a mathematical statement of complete ignorance, such as model smoothness. The effectiveness of using information from a complementary geophysical survey was demonstrated with an example of joint inversion of AEM and DC resistivity data. The recovered models from independent AEM inversion and DC resistivity inversion showed little resemblance to the true model, however, joint inversion of these data sets produced a model with strong resemblance to the true model. Generalising this result suggests that joint inversion of the data from complementary geophysical surveys will significantly reduce the non-uniqueness inherent in a single survey, and, in turn increase the confidence of geoscientists in the results of geophysical inversion.

ACKNOWLEDGMENTS

The author wishes to thank Peter Diorio, Ken Witherly and Peter Wolfgram for reviewing this manuscript and to thank BHP Minerals for permission to publish this work.

REFERENCES

- Backus, G.E., and Gilbert, J.E., 1967, Numerical Applications of a formalism for geophysical inverse problems. *Geophys. J. Roy. Astron. Soc.* **13**, 247-276.
- Backus, G.E., 1970, Inference from inadequate and inaccurate data: *Proc. Nat. Acad. Sci. U.S.A.* **65**, 1-289
- Christensen, N.B., 1970, Two-dimensional imaging of transient electromagnetic soundings; Symposium on the application of Geophysics to Engineering and Environmental Problems. Proceedings, March 23-26, Reno, Nevada, 397-406.
- Dosso, S.E., and Oldenburg, D.W., 1989, Linear and non-linear appraisal using extremal models of bounded variation, *Geophys. J. Int.*

- Ellis, R.G., and Shekhtman, R., 1994, ABFOR3D and ABINV3D: Programs for forward and inverse modelling of Airborne EM Data: JACI 1994 Ann. Rep., Dept. Geophysics and Astronomy, Univ. of British Columbia.
- Ellis, R.G., 1995, Joint 3D EM Inversion: Symposium on Three-Dimensional Electromagnetics, Proceedings, Schlumberger-Doll Research, October 4-6, Ridgefield, Connecticut, 307-323 (also to appear in Three-Dimensional Electromagnetics; Soc. Expl. Geophys., 1998).
- Fullagar, P.K., 1984, Inversion of horizontal loop electromagnetic frequency soundings: *Geophysics* **49**, 150-164.
- Li, Y., and Oldenburg, D.W., 1994, Inversion of 3D resistivity data using an approximate inverse mapping: *Geophys. J. Int.* **116**, 527-537.
- Liu, G., and Asten, M.W., 1993, Fast approximate solutions of transient EM response to a target buried beneath a conductive overburden: *Geophysics* **58**, 810-817.
- Macnae, J., Osmakoff, A., Blaha, A., King, A., and Stolz, N., 1998, Fast Approximate AEM Data Processing: *Exploration Geophysics* (this volume).
- Menke, W., 1984, *Geophysical Data Analysis: Discrete Inverse Theory*: Academic Press.
- Oldenburg, D.W., 1983, Funnel Functions in Linear and Nonlinear Appraisal: *J. Geophys. Res.* **88**, 7387-7398.
- Oldenburg, D.W., and Ellis, R.G., 1991, Inversion of Geophysical data using an approximate inverse mapping: *Geophys. J. Int.* **105**, 325-353.
- Parker, R.L., 1974, Best bounds on density and gravity data: *Geophysics* **39**, 644-649.
- Tarantola, A., and Valette, B., 1982, Inverse Problems - Quest for Information: *J. Geophys.* **50**, 159-170.
- Tikhonov, A.N., and Arsenin, V.Y., 1977, *Solution of Ill-posed Problems*: John Wiley and Sons.
- Wolfgram, P., and Karlik, G., 1995, Conductivity-depth transform of GEOTEM data: *Exploration Geophysics* **26**, 179-185.
- Xiong, Z., 1992, Electromagnetic modelling of 3D structures by the method of system iteration using integral equations: *Geophysics* **57**, 1556-1561.
- Zhdanov, M.S., Traynin, P.N., and Portniaguine, O., 1995, Resistivity imaging by time domain electromagnetic migration: *Exploration Geophysics* **26**, 186-194.

Inversion of time-domain electromagnetic data for a horizontally layered Earth

C. G. Farquharson and D. W. Oldenburg

UBC-Geophysical Inversion Facility, Department of Geophysics & Astronomy, University of British Columbia, 129–2219 Main Mall, Vancouver, BC V6T 1Z4, Canada

Accepted 1992 December 15. Received 1992 November 25; in original form 1992 June 8

SUMMARY

Time-domain electromagnetic (TEM) data are inverted to produce a conductivity model composed of horizontal layers of constant conductivity. The data can be values of the time decay of the vertical component of the magnetic field, or of its time derivative, measured at points either inside or outside a rectangular transmitter loop. Our inversion allows many more layers than there are data. This means that the constructed conductivity model not only fits the data to the required level, but also possesses particular characteristics. By suitable choice of the objective function to be minimized, our constructed model may have minimum structure in some well-defined sense and/or it may be close to some known background model. Our inversion algorithm works directly in the time domain. This requires fractionally more computing time than the alternative approach of transforming the data to the frequency domain before inversion. However, working in the time domain prevents distortion of the data and their associated measurement errors which may arise during the transformation. Also, the effects of the full transmitter current waveform can easily be incorporated by convolution in the time domain. Our inversion is applied to data from an environmental survey and the results are shown to compare favourably with a nearby well-log.

Key words: electrical conductivity, electromagnetic surveys, inversion.

1 INTRODUCTION

Time-domain electromagnetic (TEM) soundings have a well-established place in exploration geophysics, and are in the vanguard of methods used in the ever expanding field of environmental geophysics. An excellent review of the TEM method and its uses is given by Nabighian & Macnae (1991). Typically, a step or ramp turn-off in the current flowing in a rectangular transmitter loop induces currents in the Earth, and the vertical component of the h field, or its time derivative, resulting from these induced currents is measured. These measurements can be at any point on the surface of the Earth, either inside or outside the transmitter loop.

TEM measurements are commonly interpreted using an imaging technique (e.g. Macnae & Lamontagne 1987; Nekut 1987; Eaton & Hohmann 1989; Fullager 1989) or a parametric inversion (e.g. Anderson 1982, 1985; Raiche *et al.* 1985; Huang & Palacky 1991). In the imaging methods, the downward and outward diffusion of the induced current system in the Earth is approximated by one or more image

current loops that move downwards with time. The variation in the depth and speed of these image current loops with time can be converted into a conductivity–depth section that gives a smooth approximation to the true conductivity structure. These imaging techniques can be thought of as sophisticated transformations of the observed data. They are rapid to compute but the resultant conductivity is not, in general, consistent with the observations. In a parametric inversion, an over-determined least-squares problem is solved to find the thicknesses and conductivities of a limited number of layers, perhaps half-a-dozen, that most closely reproduce the observations. This approach has the potential for generating a plausible representation of the Earth. However, the results that are obtained depend on the assumed number of layers and on the starting model used in the iterative inversion.

In this paper, we present an alternative formulation. Our earth model is composed of horizontal layers of fixed thickness and constant conductivity, and is terminated by a half-space. Generally, we have many more layers than observations, so our inverse problem is under-determined.

This greatly increases the non-uniqueness of the mathematical solution but allows us to find, from the infinity of models that adequately reproduce the data, that one which minimizes a specific objective function of the model. Suitable choice of the objective function to be minimized will result in a model that is concordant with geological intuition and any prior geophysical knowledge. Ideally, the resulting model should exhibit the right 'character' (that is, smooth or blocky in accordance with the assumed geology), be as close as possible to the conductivity section obtained from a well-log or a neighbouring sounding (if such is available) and have a minimum amount of structure. This last point is particularly important since arbitrarily complicated structures, which would, therefore, seem unlikely to resemble the true Earth, can suffice as mathematical solutions. Our desire is to generate a model that contains just enough structure to fit the observations, but no more. The flexibility to generate models of a particular character enhances the usefulness of our inversion routine compared with those algorithms that concentrate only upon misfit as a criterion for an acceptable model.

An inversion formulation that admits a large number of layers is not entirely new for TEM data. Fullagar & Oldenburg (1984) treated the inversion of horizontal-loop frequency-domain data from this perspective, and Fullagar (1983) applied the algorithm to data transformed from the time domain to the frequency domain. In his inversion, however, only the norm of the perturbation to the model is minimized at each iteration, rather than the norm of the model itself. Consequently, there is no ability to control the form of the model and so generate a final model having particular characteristics. Much of the advantage of using the under-determined formalism is lost. There is also the practical difficulty of transforming the observations to the frequency domain and, in particular, of ascribing meaningful errors to the transformed data.

The measurements obtained from a TEM experiment are values of the magnetic field, or its time derivative, as a function of time. Although our inversion works directly with these time-domain data, many of the basic computations are carried out in the frequency domain. In Section 2 we give a solution to the forward problem and show how to calculate the sensitivities needed to solve the inverse problem. Our method for solving the inverse problem is presented in Section 3, and in Section 4 it is applied to both synthetic and field data.

2 THEORY

2.1 The forward problem

We consider the forward problem of calculating either $h_z(t)$ or $\partial h_z(t)/\partial t$ induced at some point on the surface of a layered conductivity structure by a step turn-off in the current in a rectangular transmitter loop. Such a layered conductivity structure, along with the coordinate system used in this paper, is shown in Fig. 1.

To exploit the work that has been done on electromagnetic methods in the frequency domain, we shall carry out the analysis in the frequency domain and, only at the very end, transform the results to the time domain. Most of the derivation below is based upon the work of Kaufman &

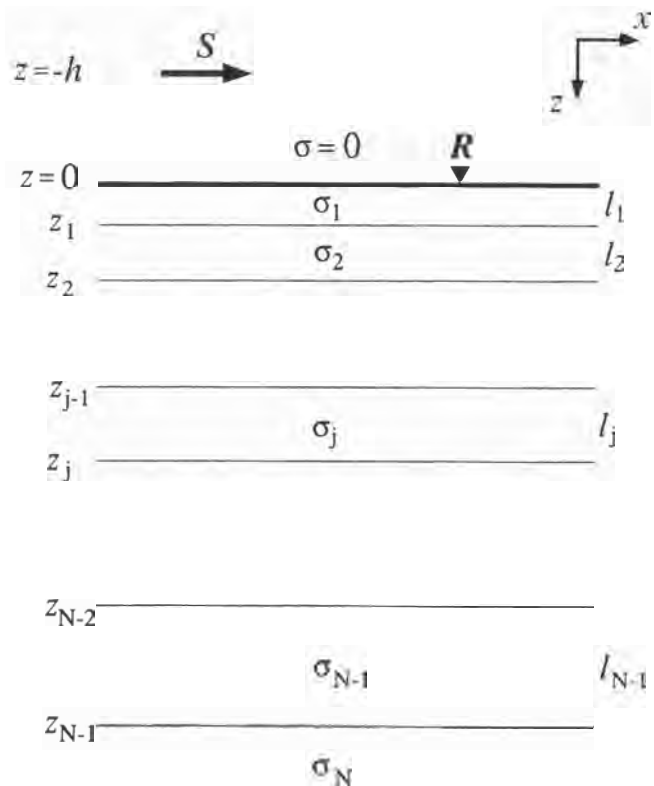


Figure 1. Notation and coordinate system for the horizontally layered conductivity model of the Earth used in this paper. z_j is the depth to the bottom of the j th layer, and σ_j and l_j are the conductivity and thickness, respectively, of the j th layer. S represents the source at a height h above the surface of the Earth, and R indicates the measurement location.

Keller (1983) and Ward & Hohmann (1988). We shall follow the notation of Ward & Hohmann and use lower case letters for fields in the time domain and upper case letters for fields in the frequency domain.

For the source-free region of Fig. 1, Maxwell's equations in the time domain are

$$\nabla \times \mathbf{e}(x, y, z, t) = -\frac{\partial}{\partial t} \mathbf{b}(x, y, z, t) \quad (1)$$

and

$$\nabla \times \mathbf{h}(x, y, z, t) = \mathbf{j}(x, y, z, t) + \frac{\partial}{\partial t} \mathbf{d}(x, y, z, t), \quad (2)$$

where \mathbf{e} , \mathbf{b} , \mathbf{h} and \mathbf{d} are the electric field intensity, the magnetic induction, the magnetic field intensity and the electric displacement, respectively. \mathbf{j} is the electric current density. By assuming a time dependence of $e^{i\omega t}$, and making use of the constitutive relations for a linear, isotropic medium, namely $\mathbf{D} = \epsilon_0 \mathbf{E}$, $\mathbf{B} = \mu_0 \mathbf{H}$ and $\mathbf{J} = \sigma \mathbf{E}$, the corresponding pair of equations in the frequency-domain is

$$\nabla \times \mathbf{E}(x, y, z, \omega) = -i\omega \mu_0 \mathbf{H}(x, y, z, \omega) \quad (3)$$

and

$$\nabla \times \mathbf{H}(x, y, z, \omega) = (\sigma + i\omega \epsilon_0) \mathbf{E}(x, y, z, \omega), \quad (4)$$

where σ is the electrical conductivity, and we have assumed for simplicity, that the magnetic permeability and the electric permittivity are everywhere equal to their free space values of μ_0 and ϵ_0 respectively. In fact, for the analysis in this paper, it is necessary only that the permeability and permittivity be constant and known in each layer.

The H field due to a rectangular transmitter loop can be evaluated by integrating the response of a horizontal electric dipole around the transmitter loop (Poddar 1982). Therefore, the major portion of the forward problem involves calculating $H_z(x, y, z, \omega)$ due to a horizontal dipole. To make use of the two axes of symmetry in this problem, one along the axis of the dipole and the other along the direction in which the conductivity is changing (i.e. the vertical direction in this 1-D earth), we introduce a vector potential $\mathbf{A}(x, y, z, \omega)$ such that

$$\mathbf{H}(x, y, z, \omega) = \nabla \times \mathbf{A}(x, y, z, \omega). \quad (5)$$

Substituting this expression for \mathbf{H} into eq. (3) gives

$$\nabla \times \mathbf{E} = -i\omega\mu_0 \nabla \times \mathbf{A}, \quad (6)$$

which implies that, assuming a region of constant permeability, the electric field intensity can be written as

$$\mathbf{E} = -i\omega\mu_0 \mathbf{A} + \nabla U, \quad (7)$$

where U is some scalar potential. Substituting eq. (5) into eq. (4) gives

$$\nabla \times \nabla \times \mathbf{A} = (\sigma + i\omega\epsilon_0)\mathbf{E}. \quad (8)$$

Using the vector identity $\nabla \times \nabla \times \mathbf{A} = \nabla \nabla \cdot \mathbf{A} - \nabla^2 \mathbf{A}$, and the expression for the electric field intensity given in eq. (7), eq. (8) becomes

$$\nabla \nabla \cdot \mathbf{A} - \nabla^2 \mathbf{A} = (\sigma + i\omega\epsilon_0)(-i\omega\mu_0 \mathbf{A} + \nabla U). \quad (9)$$

Since the scalar potential, U , is arbitrary, we can choose it such that $\nabla \cdot \mathbf{A} = (\sigma + i\omega\epsilon_0)U$. Using this expression to eliminate U from eq. (9), assuming constant conductivity and permittivity, results in the differential equation for the vector potential:

$$(\nabla^2 + \mu_0\epsilon_0\omega^2 - i\omega\mu_0\sigma)\mathbf{A}(x, y, z, \omega) = 0. \quad (10)$$

Because of the two symmetries mentioned above, the vector potential \mathbf{A} need only have two components, one in the direction of the horizontal dipole and the other in the vertical direction. Taking the dipole to lie in the x direction, \mathbf{A} has the form $\mathbf{A} = (A_x, 0, A_z)$. Moreover, because we are only interested in the vertical component of the H field, and because the relationship between \mathbf{H} and \mathbf{A} defined in eq. (5) now gives $H_z = -\partial A_x / \partial y$, we need only consider the x component of the vector potential \mathbf{A} in future calculations.

Equation (10) is valid within each layer of Fig. 1. The continuity of the tangential components of \mathbf{E} and \mathbf{H} across each boundary leads to the following conditions for the x component of the vector potential:

$$\begin{aligned} A_x^j(x, y, z = z_j, \omega) &= A_x^{j+1}(x, y, z = z_j, \omega), \\ \frac{\partial}{\partial z} A_x^j(x, y, z = z_j, \omega) &= \frac{\partial}{\partial z} A_x^{j+1}(x, y, z = z_j, \omega), \end{aligned} \quad (11)$$

where the superscript denotes the layer.

To reduce the x component of eq. (10) to an ordinary differential equation in the variable z , we shall make use of

the 2-D Fourier transform pair:

$$\begin{aligned} \bar{F}(k_x, k_y, z) &= \int_{-\infty}^{\infty} \int_{-\infty}^{\infty} F(x, y, z) e^{-i(k_x x + k_y y)} dx dy, \\ F(x, y, z) &= \frac{1}{4\pi^2} \int_{-\infty}^{\infty} \int_{-\infty}^{\infty} \bar{F}(k_x, k_y, z) e^{i(k_x x + k_y y)} dk_x dk_y. \end{aligned} \quad (12)$$

Applying this Fourier transform to the x -component of eq. (10) gives, for the j th layer,

$$\left(\frac{d^2}{dz^2} - u_j^2 \right) \bar{A}_x^j(k_x, k_y, z, \omega) = 0, \quad (13)$$

where $u_j^2 = k_x^2 + k_y^2 - \mu_0\epsilon_0\omega^2 + i\omega\mu_0\sigma_j$. The solution of eq. (13) is

$$\begin{aligned} \bar{A}_x^j(k_x, k_y, z, \omega) &= C_j(k_x, k_y, \omega) e^{i u_j(z - z_{j-1})} \\ &\quad + D_j(k_x, k_y, \omega) e^{-i u_j(z - z_{j-1})}, \end{aligned} \quad (14)$$

where C_j and D_j are determined by the boundary conditions for \bar{A}_x . These boundary conditions are obtained by applying the 2-D Fourier transform to eq. (11), giving

$$\begin{aligned} \bar{A}_x^j(k_x, k_y, z = z_j, \omega) &= \bar{A}_x^{j+1}(k_x, k_y, z = z_j, \omega), \\ \frac{\partial}{\partial z} \bar{A}_x^j(k_x, k_y, z = z_j, \omega) &= \frac{\partial}{\partial z} \bar{A}_x^{j+1}(k_x, k_y, z = z_j, \omega). \end{aligned} \quad (15)$$

In the basement half-space (layer N) the requirement that the magnetic field should decay to zero as z becomes large means that $C_N = 0$. At the top of the stack of layers, $\bar{A}_x^1(k_x, k_y, z = 0, \omega)$ must match the solution in layer 0 of the inhomogeneous version of eq. (13) which results from the presence of the horizontal electric dipole. Kaufman & Keller (eq. 2.51) give the appropriate expression for $A_x(x, y, z, \omega)$ in the non-conducting half-space above a layered earth:

$$\begin{aligned} A_x^0(x, y, z, \omega) &= \frac{I ds}{4\pi} \int_0^{\infty} \left[\frac{\lambda}{u_0} \exp(-u_0|z+h|) + \hat{C}_0(\lambda, \omega) \exp(u_0 z) \right] \\ &\quad \times J_0(\lambda r) d\lambda, \end{aligned} \quad (16)$$

where I is the current in the electric dipole, ds is the length of the dipole, $u_0^2 = \lambda^2 - \mu_0\epsilon_0\omega^2$, $\lambda^2 = k_x^2 + k_y^2$, $r^2 = x^2 + y^2$, h is the height of the dipole above the surface of the Earth, J_0 is the zeroth order Bessel function and \hat{C}_0 is determined by the boundary conditions at $z = 0$. A Hankel transform can be converted to a 2-D Fourier transform using the relationship (Ward & Hohmann, eq. 2.10)

$$\begin{aligned} 2\pi \int_0^{\infty} \bar{F}(\lambda) \lambda J_0(\lambda r) d\lambda \\ = \int_{-\infty}^{\infty} \int_{-\infty}^{\infty} \bar{F}(k_x^2 + k_y^2) e^{i(k_x x + k_y y)} dk_x dk_y, \end{aligned} \quad (17)$$

Applying this conversion to eq. (16) gives

$$\begin{aligned} \bar{A}_x^0(k_x, k_y, z, \omega) &= \frac{I ds}{2} \left[\frac{1}{u_0} \exp(-u_0|z+h|) + C_0(k_x, k_y, \omega) \exp(u_0 z) \right], \end{aligned} \quad (18)$$

where $C_0 = \hat{C}_0 / \sqrt{k_x^2 + k_y^2}$. The boundary conditions in eq.

(15) link the solutions in all the layers, from layer 0 to layer N . Using these boundary conditions, and the general form of \tilde{A}_x in each layer given by eq. (14), a pair of simultaneous equations can be constructed for D_N and C_0 . Once D_N and C_0 are known, the coefficients C_i and D_i can be calculated for all layers, hence giving \tilde{A}_x for all z .

The x component of the vector potential, $A_x(x, y, z, \omega)$, is recovered by performing the inverse 2-D Fourier transform. This is evaluated using eq. (17). The y derivative required to give $H_z(x, y, z, \omega)$ from $A_x(x, y, z, \omega)$ (see eq. 5) can be incorporated in this inverse Hankel transform:

$$\begin{aligned} H_z(x, y, z, \omega) &= -\frac{\partial}{\partial y} A_x(x, y, z, \omega) \\ &= -\frac{\partial}{\partial y} \left\{ \frac{1}{2\pi} \int_0^\infty \tilde{A}_x(\lambda, z, \omega) \lambda J_0(\lambda r) d\lambda \right\} \\ &= -\frac{1}{2\pi} \int_0^\infty \tilde{A}_x(\lambda, z, \omega) \lambda J'_0(\lambda r) \lambda \frac{\partial r}{\partial y} d\lambda \\ &= \frac{1}{2\pi r} \int_0^\infty \tilde{A}_x(\lambda, z, \omega) \lambda^2 J_1(\lambda r) d\lambda, \end{aligned} \quad (19)$$

using eq. (9.1.28) of Abramowitz & Stegun (1970), and λ and r have the same meaning as in eq. (16). Anderson's (1979a) digital filtering code is used to compute the inverse Hankel transform in eq. (19) giving H_z as a function of distance, r , from the electric dipole. This can then be integrated around the rectangular loop in the same way as Poddar (1982) to give the vertical component of the H field induced at any point on the surface of a layered earth by the rectangular transmitter loop. The desired time-domain result of either $h_z(t)$ or $\partial h_z(t)/\partial t$ can be obtained from this frequency dependence of the H field by using the digital filtering technique of Newman, Hohmann & Anderson (1986). Note that it is only in this final transformation that we have to worry about whether we are dealing with the h field or its time derivative: the analysis prior to this transformation is identical for both forms of data in the time domain. The above steps are summarized in the flow diagram in Fig. 2.

2.2 Calculation of the sensitivities

To solve the inverse problem, we need to compute the sensitivities that quantify how a change in the conductivity of each layer affects the data. The layered conductivity structure in Fig. 1 can be described in terms of a linear combination,

$$\sigma(z) = \sum_{j=1}^N \sigma_j \psi_j(z), \quad (20)$$

where the basis function, ψ_j , is a box car, equal to unity within the j th layer and zero everywhere else. The coefficient, σ_j , is equal to the conductivity of the j th layer. If these coefficients are changed by a small amount, then the resulting value of h_z (or $\partial h_z/\partial t$) measured at the surface of the conductivity structure is given by a Taylor series expansion about the original conductivity structure:

$$h[\sigma + \delta\sigma] = h[\sigma] + \sum_{j=1}^N \frac{\partial h[\sigma]}{\partial \sigma_j} \delta\sigma_j + O\|\delta\sigma\|^2, \quad (21)$$

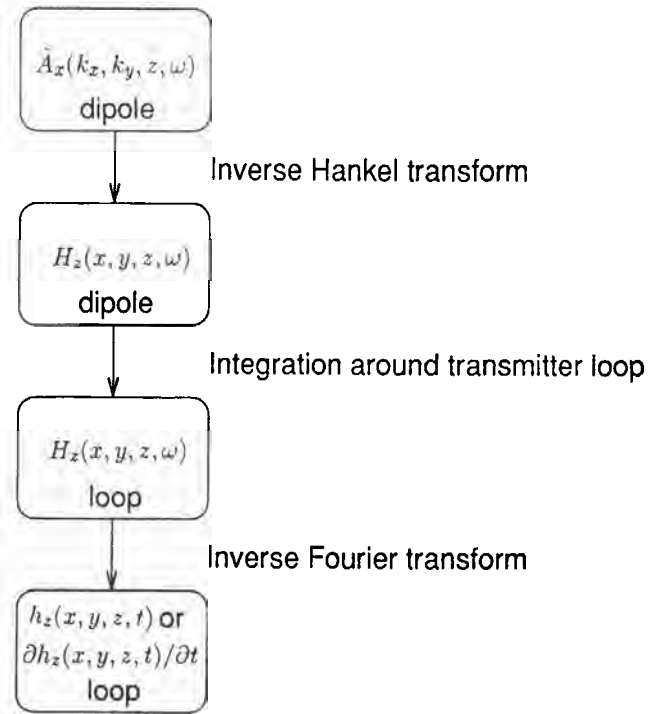


Figure 2. The sequence of integrations used to transform the values of the x component of the vector potential due to a horizontal electric dipole as a function of wavenumber and frequency to values of the vertical component of the h field, or its time derivative, for the rectangular transmitter loop as a function of space and time. This sequence of linear transformations is also used to obtain the sensitivities $\partial h/\partial\sigma_j(x, y, t)$ for the rectangular loop from the values of $\partial\tilde{A}_x/\partial\sigma_j(k_x, k_y, \omega)$ for the dipole.

where $\sigma = (\sigma_1, \dots, \sigma_N)^T$ is a vector of coefficients specifying the original conductivity structure, $\delta\sigma = (\delta\sigma_1, \dots, \delta\sigma_N)^T$ represents the changes in the coefficients, and the first-order partial derivatives are the sensitivities. The square brackets indicate the dependence on the conductivity, and $\|\cdot\|$ represents the l_2 norm. Here, and in most instances throughout the rest of this paper, we take h to represent either h_z or $\partial h_z/\partial t$.

To calculate the sensitivity $\partial h/\partial\sigma_j$, we start by considering the change in $\tilde{A}_x^1(k_x, k_y, z=0, \omega)$ for the electric dipole source that results from a change in the conductivity of the j th layer. The series of linear transformations (see Fig. 2) used to obtain $h(x, y, z, t)$ from $\tilde{A}_x^1(k_x, k_y, z, \omega)$ can then be used to obtain the desired sensitivity $\partial h/\partial\sigma_j$ for the rectangular loop.

Using the definition of the layered conductivity structure given in eq. (20), and simplifying the notation so that $F(z)$ represents \tilde{A}_x , eq. (13) can be rewritten in a form that is valid for all $z \in (-\infty, \infty)$:

$$\left(\frac{d^2}{dz^2} - u_0^2 - i\omega\mu_0 \sum_{j=0}^N \sigma_j \psi_j \right) F = S, \quad (22)$$

where $u_0^2 = k_x^2 + k_y^2 - \mu_0\epsilon_0\omega^2$ and S represents the dipole source in layer 0. Differentiating with respect to σ_j (McGillivray & Oldenburg 1990), making use of the chain rule and realizing that S is independent of σ_j , eq. (22)

becomes

$$\left(\frac{d^2}{dz^2} - u_0^2 - i\omega\mu_0 \sum_{j=0}^N \sigma_j \psi_j \right) \frac{\partial F}{\partial \sigma_j} = i\omega\mu_0 \psi_j F, \quad (23)$$

which is just an inhomogeneous ordinary differential equation for the sensitivity, $\partial F/\partial \sigma_j$. The boundary conditions are $\partial F/\partial \sigma_j \rightarrow 0$ as $z \rightarrow \pm\infty$. This boundary value problem can be solved using the adjoint Green's function method (Lanczos 1961). Hence,

$$\frac{\partial F}{\partial \sigma_j}(\xi) = \int_{-\infty}^{\infty} i\omega\mu_0 \psi_j(z) F(z) G^*(z; \xi) dz, \quad (24)$$

where the adjoint Green's function $G^*(z; \xi)$ satisfies

$$\left(\frac{d^2}{dz^2} - u_0^2 + i\omega\mu_0 \sum_{j=0}^N \sigma_j \psi_j \right) G^*(z; \xi) = \delta(z - \xi) \quad (25)$$

and

$$G^*(z; \xi) \rightarrow 0 \quad \text{as } z \rightarrow \pm\infty. \quad (26)$$

To construct the adjoint Green's function, we need two linear independent solutions of the homogeneous form of eq. (25), one of which satisfies the boundary condition as $z \rightarrow -\infty$, and the other which satisfies the boundary condition as $z \rightarrow +\infty$. For the problem under discussion in this paper, we are only interested in the value of the sensitivity at the surface of the Earth ($\xi = 0$ in eq. 24). In the region $-\infty < z \leq \xi = 0$, where the conductivity is zero, the adjoint Green's function has the form $\exp(u_0 z)$. In the region $\xi = 0 \leq z < \infty$, eq. (25) is the complex conjugate of eq. (22). And, since $F^* \rightarrow 0$ as $z \rightarrow +\infty$, the adjoint Green's function is proportional to F^* in this region. Hence,

$$G^*(z; \xi) = \begin{cases} c^- e^{u_0 z}, & z \leq \xi = 0, \\ c^+ F^*(z), & z \geq \xi = 0. \end{cases} \quad (27)$$

At $z = \xi = 0$, $G^*(z; \xi)$ must be continuous, and its derivative with respect to z must be discontinuous by an amount equal to 1 (Roach 1982). This determines the two coefficients:

$$c^- = \frac{F^*(0)}{F'^*(0) - u_0 F^*(0)}, \quad (28)$$

$$c^+ = \frac{1}{F'^*(0) - u_0 F^*(0)},$$

where the prime denotes the derivative.

So, using the explicit form of the adjoint Green's function given above, and remembering that ψ_j is unity in the j th layer and zero everywhere else, eq. (24) becomes

$$\left. \frac{\partial F}{\partial \sigma_j} \right|_{\xi=0} = \frac{i\omega\mu_0}{F'(0) - u_0 F(0)} \int_{z=z_{j-1}}^{z_j} [F(z)]^2 dz \quad (29)$$

Then, using eq. (18) to evaluate the denominator, we arrive at the following expression for the sensitivity which links the change in $\bar{A}_x^1(k_x, k_y, z=0, \omega)$ to the change in the conductivity of the j th layer:

$$\frac{\partial \bar{A}_x^1}{\partial \sigma_j}(k_x, k_y, \xi=0, \omega) = -\frac{i\omega\mu_0}{I ds} \int_{z=z_{j-1}}^{z_j} [\bar{A}_x^1(k_x, k_y, z, \omega)]^2 dz, \quad (30)$$

We can calculate this integral using the results for \bar{A}_x^i

obtained in Section 2.1. And the desired sensitivity, $\partial h/\partial \sigma_j$, can be obtained from $\partial \bar{A}_x^1/\partial \sigma_j$ by the series of transformations shown in Fig. 2.

3 INVERSION

We consider a set of M observations, $h_i^{(\text{obs})}$, $i = 1, \dots, M$ which can either be the vertical component of the h field, or its time derivative. These observations could result from measurements at different delay times, or at different locations on the surface of the Earth, or a combination of both. Our goal is to find a set of conductivities that adequately reproduce these observations. Because conductivities found in the Earth can vary over orders of magnitude, it is convenient to work with the logarithm of conductivity in the inverse problem. Also, working with logarithms ensures that σ is positive. We let $m_j = \ln \sigma_j$, and use the vector $\mathbf{m} = (m_1, \dots, m_N)^T$ to define the model for the inverse problem.

The inverse problem is non-unique: if there is one model that adequately reproduces the finite set of observations, then there is an infinite number of such models. To find a specific model, we minimize an objective function of the model which has the form

$$\phi_m = \|\mathbf{W}_m(\mathbf{m} - \mathbf{m}^{(\text{ref})})\|^2 \quad (31)$$

where \mathbf{W}_m is a weighing matrix and $\mathbf{m}^{(\text{ref})}$ is a reference model. The model, \mathbf{m} , that minimizes ϕ_m will have a character that depends on the particular choices for the weighing matrix and the reference model. The reference model can be used to include any *a priori* information that may be available about the possible conductivity structure. We note that the explicit inclusion of a reference model is of particular importance when the model is parameterized in terms of the logarithm of conductivity. If the reference model were omitted from ϕ_m , the implicit reference conductivity of 1 S m^{-1} could severely bias the inversion results.

The numerical values for \mathbf{W}_m can be generated by deciding what type of model is to be found. This is easily accomplished by considering a functional analogous to ϕ_m for models that are continuous functions of depth, for example,

$$\Phi_m = \int_{z=0}^{\infty} w(z) |T[m(z) - m^{(\text{ref})}(z)]|^2 dz. \quad (32)$$

The operator T can be the identity operator, or the first or second order derivative with respect to z . The function $w(z)$ is an additional weighting function which can be used to enhance or suppress structure over certain depth ranges. The weighing matrix \mathbf{W}_m can be obtained by making ϕ_m the discrete equivalent of Φ_m .

To determine whether or not the data produced by our model conductivity structure are sufficiently close to the observations, we introduce the following measure of misfit:

$$\phi_d = \|\mathbf{W}_d[\mathbf{h}^{(\text{obs})} - \mathbf{h}^{(\text{pred})}]\|^2, \quad (33)$$

where $\mathbf{h}^{(\text{pred})}$ is the vector made up of the data predicted from the model, and $\mathbf{W}_d^T \mathbf{W}_d = \mathbf{C}_d^{-1}$, where \mathbf{C}_d is the covariance matrix. Our objective in the inversion is to find a model which gives a misfit, ϕ_d , equal to a target misfit $\phi_d^{(\text{tar})}$.

For the examples used here, we will assume that the data errors are unbiased, independent and Gaussian. In such cases, \mathbf{W}_d is a diagonal matrix whose elements are the reciprocals of the standard deviation of each datum, and ϕ_d is equal to the χ^2 random variable. From the properties of the χ^2 random variable, the expected value of ϕ_d is equal to M , the number of observations. Hence, our final target misfit in the inverse problem is $\phi_d^{(\text{tar})} = M$.

The relationship between the observations and the model conductivity structure is non-linear and so an iterative method is required to solve the inverse problem. At the $(n+1)^{\text{th}}$ iteration,

$$\phi_d^{(n+1)} = \|\mathbf{W}_d[\mathbf{h}^{(\text{obs})} - \mathbf{h}^{(n+1)}]\|^2, \quad (34)$$

Using the Taylor series expansion in eq. (21), this can be approximated by

$$\phi_d^L = \|\mathbf{W}_d[\mathbf{h}^{(\text{obs})} - \mathbf{h}^{(n)} - \mathbf{D}\delta\mathbf{m}]\|^2, \quad (35)$$

where $D_{ij} = \partial h_i / \partial m_j = \sigma_j \partial h_i / \partial \sigma_j$, since the model is now defined in terms of the natural logarithm of conductivity. The superscript L distinguishes this linearized estimate of the misfit from the true misfit defined in eq. (34). We shall make use of ϕ_d^L in the solution of the linear system of equations at each iteration, but it is $\phi_d^{(n)}$ that is the true measure of how the iterative scheme is progressing. By writing $\delta\mathbf{m}$ explicitly as the difference between the model parameters at two successive iterations (e.g. Oldenburg, 1983; Constable, Parker & Constable 1987), and introducing the reference model, eq. (35) becomes

$$\begin{aligned} \phi_d^L &= \|\mathbf{W}_d[\mathbf{h}^{(\text{obs})} - \mathbf{h}^{(n)} - \mathbf{D}\mathbf{m}^{(\text{ref})} + \mathbf{D}\mathbf{m}^{(\text{ref})} - \mathbf{D}\mathbf{m}^{(n+1)} + \mathbf{D}\mathbf{m}^{(n)}]\|^2 \\ &= \|\mathbf{d}^{(n)} - \hat{\mathbf{D}}\hat{\mathbf{m}}^{(n+1)}\|^2, \end{aligned} \quad (36)$$

where

$$\begin{aligned} \mathbf{d}^{(n)} &= \mathbf{W}_d[\mathbf{h}^{(\text{obs})} - \mathbf{h}^{(n)} - \mathbf{D}\mathbf{m}^{(\text{ref})} + \mathbf{D}\mathbf{m}^{(n)}], \\ \hat{\mathbf{D}} &= \mathbf{W}_d \mathbf{D} \mathbf{W}_m^{-1}, \\ \hat{\mathbf{m}}^{(n+1)} &= \mathbf{W}_m[\mathbf{m}^{(n+1)} - \mathbf{m}^{(\text{ref})}]. \end{aligned} \quad (37)$$

Hence, the linearized inverse problem to be solved at the $(n+1)^{\text{th}}$ iteration is:

minimize

$$\phi_m = \|\hat{\mathbf{m}}^{(n+1)}\|^2 \quad (38)$$

subject to the constraint that

$$\phi_d^L = \|\mathbf{d}^{(n)} - \hat{\mathbf{D}}\hat{\mathbf{m}}^{(n+1)}\|^2 = \phi_d^{(\text{tar})}. \quad (39)$$

This problem could be solved by differentiating the objective function

$$\phi = \phi_m + \alpha[\phi_d^L - \phi_d^{(\text{tar})}] \quad (40)$$

with respect to the elements of $\mathbf{m}^{(n+1)}$ and equating to zero (α is a Lagrange multiplier). This would create an $N \times N$ system of equations to be solved for $\mathbf{m}^{(n+1)}$. However, in

this paper, we use the more computationally efficient method of singular value decomposition (SVD) and exploit the fact that the SVD solution of an underdetermined system of equations is the one with the smallest l_2 norm (Wiggins 1972; Parker 1977; Menke 1984; Golub & Van Loan 1989).

The SVD of the matrix $\hat{\mathbf{D}}$ is $\hat{\mathbf{D}} = \mathbf{U}\mathbf{\Lambda}\mathbf{V}^T$. The solution to the linearized inverse problem in eqs (38) and (39) is then given by

$$\hat{\mathbf{m}}^{(n+1)} = \mathbf{V}\mathbf{\Lambda}^{-1}\mathbf{U}^T\mathbf{d}^{(n)} \quad (41)$$

where $T_{ij} = \alpha s_i^2 \delta_{ij} / (\alpha s_i^2 + 1)$, s_i is the i th singular value of $\hat{\mathbf{D}}$ and δ_{ij} is the Kronecker delta (Wiggins 1972). The Lagrange multiplier α (the same as that in eq. (40) above) could be chosen using a line search so that the constraint $\phi_d^L = \phi_d^{(\text{tar})}$ in eq. (39) is satisfied. However, it is a solution to the full non-linear inverse problem that we require. We, therefore, use the line search and forward modelling to choose α such that $\phi_d^{(n+1)} = \phi_d^{(\text{tar})}$. Finally, since the linearized inverse problem defined by eqs (38) and (39) is only an approximation to the full non-linear problem, it is prudent to set the target misfit at each iteration to be some fraction β of the misfit resulting from the previous iteration. So, at the $(n+1)^{\text{th}}$ iteration, $\phi_d^{(\text{tar})}$ is chosen to be $\max[\beta\phi_d^{(n)}, M]$ where β is typically $0.1 \leq \beta \leq 0.5$.

We shall now apply the above iterative procedure to both synthetic and field data.

4 EXAMPLES

4.1 Synthetic data

Synthetic data were generated from the three-layered conductivity structure shown in Fig. 3. The transmitter loop was a square of side 50 m and the vertical component of the h field due to a step turn-off in a 1 A current was calculated 50 m from the centre of the loop. Only a pure step turn-off in the transmitter current was considered: no linear ramp was included. Both the transmitter and the receiver lay on the surface of the conductivity structure, and 20 values of h_z were calculated over the range of delay times shown in Fig. 4. Gaussian random noise with a standard deviation of 2.5 per cent was added to the values of h_z . The data, with estimated error bars, are shown in Fig. 4.

The inversion routine was used to obtain three different conductivity models, each with a distinct character, that reproduced the synthetic data to a similar level of misfit. These three models minimize, in turn, the difference between the model and a reference half-space of $5 \times 10^{-2} \text{ S m}^{-1}$, the gradient of the model, and the curvature. For convenience, we refer to them generically as the smallest, flattest, and smoothest models. The controlling factor for each model is the weighting matrix, \mathbf{W}_m . For the smallest model,

$$\mathbf{W}_m = \text{diag}(\sqrt{l_1}, \sqrt{l_2}, \dots, \sqrt{l_{N-1}}, \sqrt{l_{N-1}}), \quad (42)$$

where l_j is the thickness of the j th layer. The final element of \mathbf{W}_m , which corresponds to the basement half-space, is given the same value as the previous element.

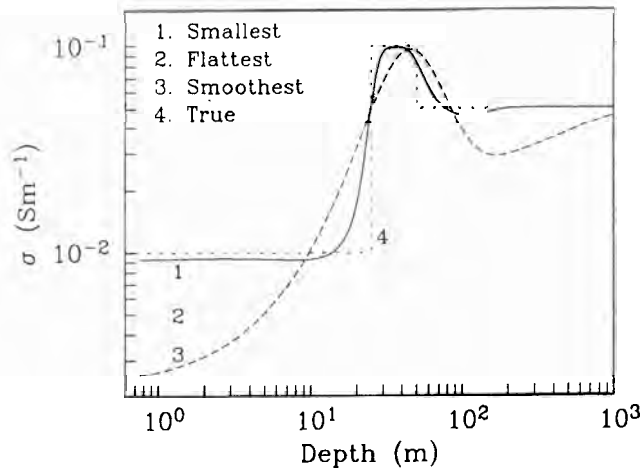


Figure 3. The three-layer model ('true') used to generate the synthetic data, and the three models produced by the inversion routine. For clarity, the individual layers in the smallest, flattest and smoothest models are not shown.

The weighting matrix for the flattest model is

$$W_m = \begin{bmatrix} \left(\frac{l_1+l_2}{2}\right)^{-1/2} & -\left(\frac{l_1+l_2}{2}\right)^{-1/2} & 0 & \dots & 0 \\ 0 & \left(\frac{l_2+l_3}{2}\right)^{-1/2} & -\left(\frac{l_2+l_3}{2}\right)^{-1/2} & 0 & \dots \\ \vdots & \vdots & \vdots & \vdots & \vdots \\ 0 & \dots & 0 & (l_{N-1})^{-1/2} & -(l_{N-1})^{-1/2} \\ 0 & \dots & \dots & 0 & C \end{bmatrix} \quad (43)$$

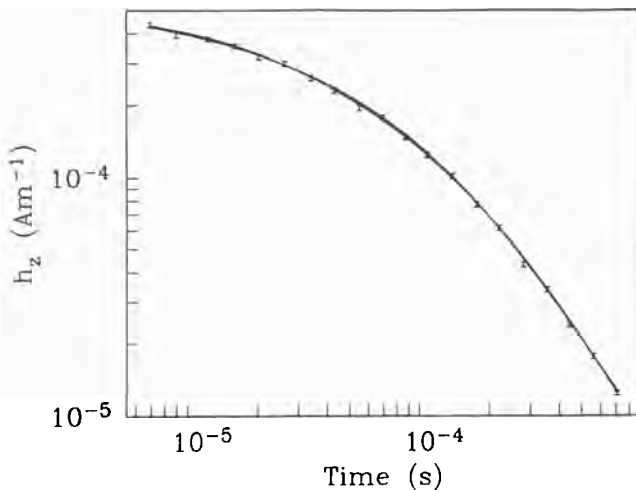


Figure 4. The synthetic data, and associated error bars, generated from the three-layer model in Fig. 3. The values of h_z were calculated 50 m from the centre of a 50 m \times 50 m transmitter loop. A pure step turn-off in a 1 A current was used as the transmitter current waveform and Gaussian random noise of standard deviation 2.5 per cent was incorporated into the data. The continuous curves represent the data predicted by each of the three models shown in Fig. 3 that resulted from the inversion.

where the constant, C , was chosen as $10^{-3}(l_{N-1})^{-1/2}$. This value is effectively negligible compared with the other elements in the matrix, and yet is sufficiently large so that W_m^{-1} can be computed. For the smoothest model, the weighting matrix is the square of the matrix used for the flattest model.

The resulting three models are shown in Fig. 3. All have 100 layers ($N = 100$), with the thicknesses increasing exponentially (to the base 1.05 with the thickness of the first layer equal to 0.5 m). During the inversion process, β (the desired reduction in misfit at each iteration) was kept fixed at 0.5. This gave a slow but steady convergence towards the final model.

The forward calculations from the three models produced by the inversion routine are represented by the continuous lines in Fig. 4. The values of ϕ_d for the smallest, flattest and smoothest models were 20.0, 20.1 and 20.3 respectively ($M = 20$). Although these three values represent an equivalent fit to the data, the models are noticeably different in character. These different characters are a direct consequence of the particular model norm that was minimized in the inversion. The most obvious differences appear in the depth ranges that are poorly constrained by the data: below approximately 200 m the smallest model returns to its reference half-space of $5 \times 10^{-2} \text{ S m}^{-1}$, the flattest model levels out to achieve zero gradient, and the smoothest model degenerates to a straight line when no longer influenced by the data. Similar behaviours can be seen at shallow depths above about 10 m. Even in the depth range to which the data are most sensitive (10–200 m, approximately) there are differences in character between the three models. The smallest model manages to follow the block nature of the true model quite closely, whereas the smoothest model smears out the high conductivity layer as much as it can in order to produce the model with the minimum amount of curvature.

From Fig. 3 it is obvious that the smallest model is the closest to the 'true' Earth. However, the remarkable agreement above 10 m depth is somewhat fortuitous, since the model at these depths is very poorly constrained by the data, and the behaviour of the model is dominated by ϕ_m . And the exact agreement below 200 m is only to be expected since we chose our reference model to have the same conductivity as the basement half-space in the true Earth. In general, we found that the smallest model often contained too much unrealistic structure, and that a minimum structure model gave the most plausible representation of the true Earth. In particular, the tendency of the flattest model to cause less smearing out of abrupt changes in conductivity compared with the smoothest model, as shown in Fig. 3, and the obvious levelling off when no longer constrained by the data, made the flattest model our preferred choice in many cases.

4.2 Field data

To test the inversion routine with more realistic data, we inverted two sets of field data acquired during an environmental study. Values of the time derivative of the vertical component of the h field were measured at the centre of a square (60 m \times 60 m) transmitter loop using the Geonics Protem system. The data, and their assumed errors,

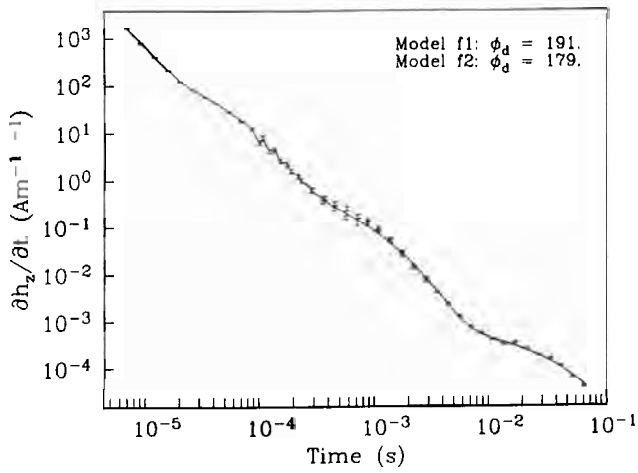


Figure 5. A TEM sounding acquired during an environmental survey. The transmitter loop was $60\text{ m} \times 60\text{ m}$, and the receiver was at its centre. The data were acquired in three overlapping sweeps: $7\ \mu\text{s}$ – 0.7 ms , 0.1 – 2.8 ms , and 0.8 – 70 ms . The observations and assigned measurement errors are represented by the error bars. The continuous curve indicates the data predicted from both models f1 and f2 in Fig. 7.

obtained from soundings at two different locations are presented in Figs 5 and 6.

The Protem instrument uses a linear ramp turn-off of length τ instead of the pure step turn-off, which is impossible to generate in practice. This modification of the source current waveform can be taken into account when calculating the resultant time decay of the fields by convolving a boxcar of length τ and height $1/\tau$ with the values of $\partial h_z/\partial t$ calculated for a pure step-off current source (Asten 1987). The observations shown in both Figs 5 and 6 were acquired in three overlapping sweeps, the first sweep from $7\ \mu\text{s}$ to 0.7 ms , the second from 0.1 to 2.8 ms , and the third from 0.8 ms onwards. The length of the ramp, τ , for these sweeps was $3.5\ \mu\text{s}$, $35\ \mu\text{s}$ and $45\ \mu\text{s}$, respectively.

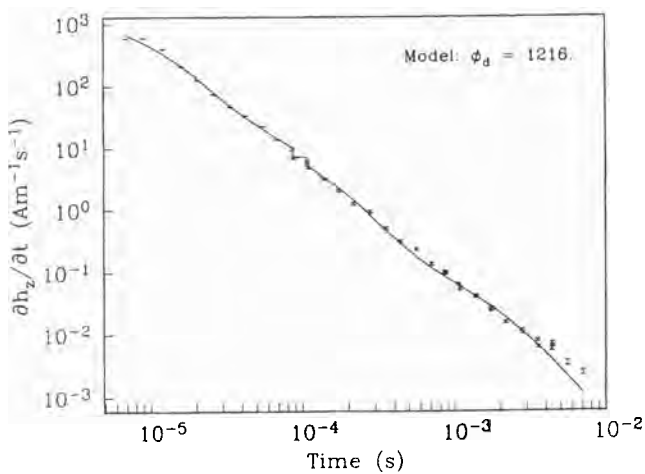


Figure 6. A second sounding from an environmental survey. The survey geometry and the three measurement sweeps are the same as for Fig. 5. The error bars indicate the observations and assigned measurement errors, and the continuous curve represents the predicted data from the flattest model produced by the inversion, and shown in Fig. 8.

These different ramp times give the data a somewhat sawtooth appearance in the time range for which the sweeps overlap.

The linear ramp turn-off in the transmitter current must also be taken into account in the inversion process. Because we are carrying out the inversion in the time domain, the sensitivities required for a ramp turn-off in the transmitter current can be obtained by applying the above convolution to the sensitivities calculated for the pure step turn-off.

For the data in Fig. 5, errors of 1 per cent, 10 per cent and 5 per cent were assigned to early, mid and late time measurements, respectively. For the data in Fig. 6, errors of 1 per cent were assigned to early time measurements, errors of 5 per cent to intermediate time measurements and errors of 10 per cent to the last few measurements.

Fig. 7 shows two inversion results for the data in Fig. 5. Model f1, represented by solid line, was obtained using the same weighting matrix as for the flattest model in Section 4.1. Model f2, represented by the dotted line, was obtained using the weighting matrix

$$\mathbf{W}_m = \begin{pmatrix} 1 & -1 & 0 & \cdots & 0 \\ 0 & 1 & -1 & & \vdots \\ & & \ddots & & \\ \vdots & & & 1 & -1 \\ 0 & \cdots & & 0 & C \end{pmatrix} \quad (44)$$

where $C = 10^{-3}$. Both models have 200 layers increasing exponentially in thickness (to the base 1.03, with the first layer of thickness 0.1 m). Because of this increasing layer thickness, the model norm constructed using \mathbf{W}_m above is essentially a discretized version of

$$\Phi_m = \int_{z=0}^{\infty} \left[\frac{d(\ln \sigma)}{d(\ln z)} \right]^2 d(\ln z) = \int_{z=0}^{\infty} z \left[\frac{d(\ln \sigma)}{dz} \right]^2 dz. \quad (45)$$

Similarly, the model norm constructed using \mathbf{W}_m in eq. (43) is a discretized version of

$$\Phi_m = \int_{z=0}^{\infty} \left[\frac{d(\ln \sigma)}{dz} \right]^2 dz. \quad (46)$$

The dashed line in Fig. 7 corresponds to the result obtained from a parameter estimation program (TEMEX-GL) based on (Anderson 1979b) which was restricted to contain seven layers.

The values of the misfit ϕ_d for models f1 and f2 were 191 and 179, respectively. The value of ϕ_d for the seven-layer model was 983. Models f1 and f2 produce nearly identical fits to the observations, as illustrated in Fig. 5. However, the two values of misfit quoted above are still significantly larger than the expected value of 56 (the number of observations). No model could be found which gave a smaller misfit than that for model f2. This suggests that the errors we assigned to the data are smaller than the true uncertainties in the measurements. This seems entirely plausible, especially for the late time measurements, where uncertainties of 30 or 40 per cent are more likely to be realistic.

The similarity between the two models in Fig. 7, despite the different nature of the weighting matrices used to produce them, emphasizes the robustness of an inversion routine which looks for a minimum structure model. Since

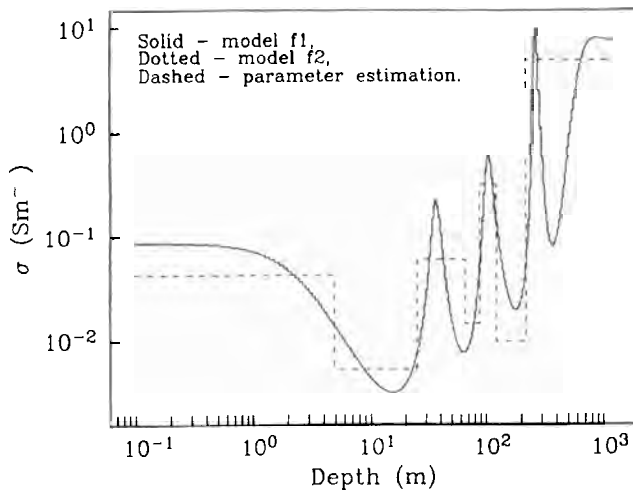


Figure 7. f1 and f2 are the two versions of the flattest model obtained from the inversion of the data in Fig. 5. The best-fitting seven-layer model produced by a parameter estimation routine (TEMEX-GL) is also shown.

models f1 and f2 both contain just enough structure to fit the data, it is not surprising that they agree on the features that are required by the data. This provides confidence that the particular sequence of conductive and resistive layers to a depth of about 300 m is present in the real Earth.

Below 300 m the models are poorly constrained by the observations, and so the particular form of the weighting matrix dominates their behaviour. The weighting term, z , that appears in eq. (45) but not (46), therefore, causes structure in model f2 to be suppressed at these depths compared with model f1. However, the fact that both models f1 and f2 do show increases in conductivity around 500 m depth, rather than levelling off, might indicate the presence of a good conductor on the extreme limit of penetration of this sounding. At shallow depths, the different weighting matrices lead to structure being enhanced in model f2 relative to model f1.

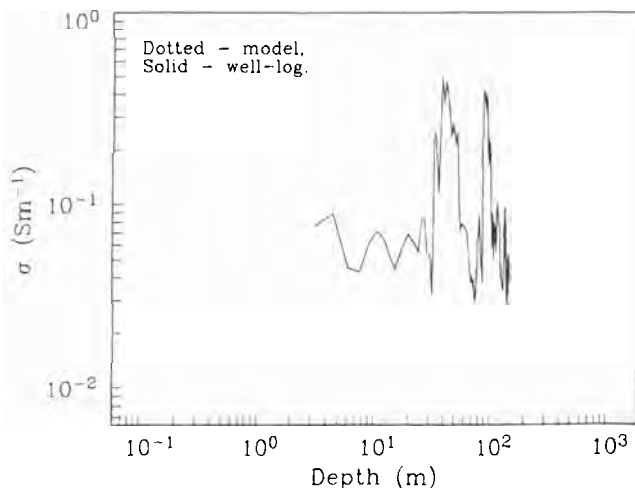


Figure 8. The flattest model (dotted line) obtained from the inversion of the data in Fig. 6. The solid line represents the values of the conductivity measured in a borehole 70 m from the observation site.

As a final example, the data from the second sounding (see Fig. 6) were inverted. The weighting matrix was the same as the one used to produce model f2 in Fig. 7. The resulting model is represented by the dotted line in Fig. 8. It is again made up of 200 layers whose thicknesses increase exponentially with depth. The solid line in Fig. 6 represents the data predicted by this model. The corresponding value of the misfit was $\phi_d = 1216$. The assigned uncertainties again seem to be too small and it was impossible to obtain a misfit close to the expected value of 40. The solid line in Fig. 8 represents well-log measurements of conductivity obtained from a borehole 70 m away from the location of the sounding. There is very good agreement between the model and the well-log measurements in the depth range 10–150 m, especially on the location of the upper regions of the two conductive zones around 35 and 90 m. The character of the well-log, comprising transition zones rather than a few layers of constant conductivity, is also reproduced by the model in Fig. 8. This type of model, constructed by minimizing the l_2 norm of its gradient, therefore, seems particularly suited to this geological setting.

5 DISCUSSION

In this paper, we have presented an inversion algorithm that generates a layered conductivity structure from measurements of h_z or $\partial h_z / \partial t$ as functions of time. Our inversion operates on data in the time-domain, despite the fact that a large part of the computations take place in the frequency domain. Our approach requires many more transformations between the frequency- and time domains than the alternative strategy of transforming the data to the frequency domain before inversion. However, the time required for these transformations is only a fraction of that required to generate the sensitivities as functions of frequency. Moreover, working with data in the time domain avoids the question of how to transform a limited number of data points and associated measurement errors to the frequency domain without loss of information. The extra effort required to carry out the inversion in the time-domain, therefore, allows full use to be made of the measurement errors, both in deciding how well the data should be fit, and in determining the relative importance of each datum in the inversion. One further advantage of the approach presented in this paper is the ease with which an arbitrary transmitter current waveform can be incorporated by convolution in the time domain: we simply convolve the waveform with both the predicted data and sensitivities calculated from an impulsive current source.

We used singular value decomposition (SVD) to solve the linear system of equations at each iteration: from the properties of SVD, such a solution to an underdetermined system of equations is the minimum l_2 norm solution. This technique is more computationally efficient than inverting the $N \times N$ system of equations obtained by explicitly minimizing an objective function with respect to the model parameters.

The formulation we have presented is quite general in its ability to generate different conductivity models. The choice of weighting matrix, reference model and norm provides a great deal of flexibility in tailoring the constructed model so that it is consistent with any prior geological and geophysical

information. In this paper, we have only considered a weighted l_2 norm. This results in conductivity structures that change somewhat slowly with depth. Other norms are possible. For example, the l_1 norm used by Dosso & Oldenburg (1989) to minimize the total variation of the conductivity as a function of depth in the inversion of magnetotelluric data produces models that are blocky in character. This is preferable if the local geology is known to be made up of distinct, contrasting layers. This is an assumption that is often made when inverting data. However, the character of the well-log in Fig. 8 is more in keeping with transition zones rather than abrupt jumps between neighbouring layers and the minimum structure model obtained using the l_2 norm mimics these gradual changes very well.

As a final comment, we mention that we have worked completely with the physical quantities that are measured in a TEM survey, either h_z or $\partial h_z/\partial t$, rather than working with an apparent conductivity. This means that the inversion routine presented here can be applied to the response for any source-receiver geometry, for which, typically, the transformation to apparent conductivity is multivalued, and, hence, not easy to carry out.

ACKNOWLEDGMENTS

We are extremely grateful to Cliff Candy of Frontier Geosciences, Inc., for supplying the field data, the well-log measurements and the results of the TEMEX-GL program (Interprex, Ltd.). C.G.F. would like to acknowledge receipt of a Commonwealth Scholarship. This research was supported by NSERC grant 5-84270.

REFERENCES

- Abramowitz, M. & Stegun, I. A., 1970. *Handbook of Mathematical Functions*, Dover Publications, New York.
- Anderson, W. L., 1979a. Numerical integration of related Hankel transforms of orders 0 and 1 by adaptive digital filtering, *Geophysics*, **44**, 1287-1305.
- Anderson, W. L., 1979b. Programs TRANS_HCLOOP and TRANS_HZWIRE: calculation of the transient horizontal coplanar loop soundings and transient wire-loop soundings, *USGS Open-File Report 79-590*.
- Anderson, W. L., 1982. Adaptive non-linear least-squares solution for constrained or unconstrained minimization problems (Subprogram NLSOL), *USGS Open-File Report 82-68*.
- Anderson, W. L., 1985. Computation of transient soundings for the time-derivative of H_z near a rectangular loop source on a layered earth (Program FWDTHZ), *USGS Open-File Report 85-270*.
- Asten, M. W., 1987. Full transmitter waveform transient electromagnetic modeling and inversion for soundings over coal measures, *Geophysics*, **52**, 279-288.
- Constable, S. C., Parker, R. L. & Constable, C. G., 1987. Occam's inversion: a practical algorithm for generating smooth models from electromagnetic sounding data, *Geophysics*, **52**, 289-300.
- Dosso, S. E. & Oldenburg, D. W., 1989. Linear and non-linear appraisal using extremal models of bounded variation, *Geophys. J. Int.*, **99**, 483-495.
- Eaton, P. A. & Hohmann, G. W., 1989. A rapid inversion technique for transient electromagnetic soundings, *Phys. Earth. planet. Inter.*, **53**, 384-404.
- Fullagar, P. K., 1983. Backus-Gilbert inversion of SIROTEM soundings, *Abstracts: The Third Biennial Conference of the ASEG*, pp. 28-30.
- Fullagar, P. K., 1989. Generation of conductivity-depth pseudosections from coincident loop and in-loop TEM data, *Expl. Geophys.*, **20**, 43-45.
- Fullagar, P. K. & Oldenburg, D. W., 1984. Inversion of horizontal loop electromagnetic frequency soundings, *Geophysics*, **49**, 150-164.
- Golub, G. H. & Van Loan, C. F., 1989. *Matrix Computations*, The John Hopkins University Press, Baltimore.
- Huang, H. & Palacky, G. J., 1991. Damped least-squares inversion of time-domain airborne EM data based on singular value decomposition, *Geophys. Prosp.*, **39**, 827-844.
- Kaufman, A. A. & Keller, G. V., 1983. *Frequency and Transient Soundings*, Elsevier, Amsterdam.
- Lanczos, C., 1961. *Linear Differential Operators*, Van Nostrand, London.
- McGillivray, P. R. & Oldenburg, D. W., 1990. Methods for calculating Fréchet derivatives and sensitivities for the non-linear inverse problem: a comparative study, *Geophys. Prosp.*, **38**, 499-524.
- Macnae, J. & Lamontagne, Y., 1987. Imaging quasi-layered conductive structures by simple processing of transient electromagnetic data, *Geophysics*, **52**, 545-554.
- Menke, W., 1984. *Geophysical Data Analysis: Discrete Inverse Theory*, Academic Press, Orlando.
- Nabighian, M. N. & Macnae, J. C., 1991. Time-domain electromagnetic prospecting methods, in *Electromagnetic Methods in Applied Geophysics*, Vol. 2, pp. 427-479, ed. Nabighian, M. N., Soc. Expl. Geophys., Tulsa.
- Nekut, A. G., 1987. Direct inversion of time-domain electromagnetic data, *Geophysics*, **52**, 1431-1435.
- Newman, G. A., Hohmann, G. W. & Anderson, W. L., 1986. Transient electromagnetic response of a three-dimensional body in a layered Earth, *Geophysics*, **51**, 1608-1627.
- Oldenburg, D. W., 1983. Funnel functions in linear and non-linear appraisal, *J. geophys. Res.*, **88**, 7387-7398.
- Parker, R. L., 1977. Understanding inverse theory, *Ann. Rev. Earth planet. Sci.*, **5**, 35-64.
- Poddar, M., 1982. A rectangular loop source of current on a two-layered Earth, *Geophys. Prosp.*, **30**, 101-114.
- Raiche, A. P., Jupp, D. L. B., Rutter, H. & Vozoff, K., 1985. The joint use of coincident loop transient electromagnetic and Schlumberger sounding to resolve layered structures, *Geophysics*, **50**, 1618-1627.
- Roach, G. F., 1982. *Green's Functions*, Cambridge University Press, Cambridge.
- Ward, S. H. & Hohmann, G. W., 1988. Electromagnetic theory for geophysical applications, in *Electromagnetic Methods in Applied Geophysics*, Vol. 1, pp. 131-311, ed. Nabighian, M. N., Soc. Expl. Geophys., Tulsa.
- Wiggins, R. A., 1972. The general linear inverse problem: Implication of surface waves and free oscillations for Earth structure, *Rev. Geophys. Space Phys.*, **10**, 251-285.

Layered Earth Inversion Model

Number of layers: 28

Depth 1	5m
Depth 2	11m
Depth 3	17m
Depth 4	25m
Depth 5	34m
Depth 6	44m
Depth 7	55m
Depth 8	68m
Depth 9	83m
Depth 10	101m
Depth 11	120m
Depth 12	143m
Depth 13	169m
Depth 14	199m
Depth 15	234m
Depth 16	273m
Depth 17	319m
Depth 18	371m
Depth 19	431m
Depth 20	500m
Depth 21	580m
Depth 22	673m
Depth 23	783m
Depth 24	909m
Depth 25	1056m
Depth 26	1228m
Depth 27	1426m
Depth 28	1658m

APPENDIX D: QUALIFICATIONS

Statement of Qualifications – Ken E. Witherly

I have graduated from University of British Columbia with the degree of Bachelor of Science in Geophysics/Physics, in 1971.

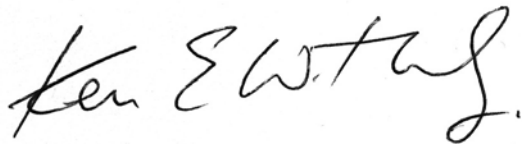
I have practiced my profession continuously since 1971;

I am employed as an exploration geophysicist by Condor Consulting, Inc.;

I have no interest, direct or indirect, in the mineral exploration dispositions comprising the areas described in this report nor do I expect to receive any;

I am registered with the American Institute of Professional Geologists as a Certified Professional Geologist; # 11536

Dated this 23rd day of April, 2021

A handwritten signature in black ink that reads "Ken E. Witherly". The signature is written in a cursive, flowing style.

President, Condor Consulting Inc.

Lakewood, Colorado